

**HYDROMECHANICAL SLOPE STABILITY ANALYSIS: MODELLING,  
MONITORING AND PREDICTION USING BP-FF ARTIFICIAL NEURAL  
NETWORKS**

**BY**

**KANULE M. B. JASON**

**A THESIS SUBMITTED IN PARTIAL FULFILMENT OF THE  
REQUIREMENTS FOR THE DEGREE OF DOCTOR OF PHILOSOPHY IN  
PHYSICS IN THE SCHOOL OF SCIENCE,  
UNIVERSITY OF ELDORET, KENYA**

**JUNE, 2021**

## DECLARATION

### Declaration by the Candidate

This thesis is my original work and has not been submitted for any academic award in any institution; and shall not be reproduced in part or full, or in any format without prior written permission from the author and/or University of Eldoret.

**Kanule B. Jason**

Signature: ..... Date: .....

**SC/D.PHIL/20/08**

### Declaration by Supervisors

This thesis has been submitted with our approval as University supervisors.

**Prof. Wilson Ng'etich**

Signature: ..... Date: .....

University of Eldoret, Kenya

**Prof. Samuel Rotich**

Signature: ..... Date: .....

Moi University, Kenya

**DEDICATION**

To my children *Noel Prudence, Godwill Mordeccai* and *Eleanor Perpetua*

## ABSTRACT

Sloping regions of the earth's crust have formed part of human settlements from time immemorial. However, these regions are prone to geological hazards especially mass wasting processes such as debris flows and landslips. While literature on soil mass movements is available, precise mathematical models, versatile instrumentation systems, and the utilization of intelligent artificial neural network (ANN) models for forecasting these events in space and time is limited.

This study was aimed at undertaking explicit characterization of convex configuration slopes under varying hydrological conditions. Specifically, it involved formulation of numerical models based on spherical-cap-shaped slip zones as well as development of ANN and hydromechanical landslide model. Computational results from the models were calibrated using experimental findings based on a solar powered data acquisition system which comprised of a laboratory flume, sensor array and data broadcasting scheme. Finally, a (Back-Propagation Feed-Forward) BP-FF ANN model was developed for purposes of predicting the slope stability status by way of numerical values of the factor of safety (FS).

Results from quantitative analysis indicated that the mode of failure and configuration of the slip zone is a function of the volumetric water content (VWC), location of the apparent phreatic surface, magnitude of cohesive strength, orientation of weak planes and existence of discontinuities. Consequently, progressive translational displacement is the most dominant mechanism of failure and the slip zones assume the shape of single or double spherical caps, depending on the morphology of the potential failure plane (planar or curvilinear), location of the phreatic surface and flaws. Furthermore, results from numerical models demonstrated that geotechnical, geophysical and hydrological parameters and by extension the FS can be defined as empirical functions of the VWC. Additionally, results showed that the amount of VWC at the interfaces between adjacent lithostratigraphic units is the principal trigger of soil mass movements. The calibrated BP-FF ANN model was used to predict the FS values of slopes.

In conclusion, since an improved effective wetness index has been derived taking into consideration the moist unit weight, threshold VWC extracted directly from the hydromechanical model and a BP-FF ANN model has been trained, an early warning system can be developed based on this information for purposes of prediction and disaster mitigation. Inferences derived from the study will provide precise constitutive computations as well as baseline geophysical and hydrological information to the public on the stability status of slopes.

## TABLE OF CONTENTS

DECLARATION .....	ii
DEDICATION .....	iii
ABSTRACT .....	iv
TABLE OF CONTENTS .....	v
LIST OF TABLES .....	x
LIST OF FIGURES .....	xi
LIST OF ABBREVIATIONS, ACRONYMS, AND SYMBOLS .....	xiii
ACKNOWLEDGEMENTS .....	xvi
<b>CHAPTER ONE .....</b>	<b>1</b>
<b>INTRODUCTION.....</b>	<b>1</b>
1.1 General Introduction .....	1
1.2 Slope stability – risk, investigation and mitigation measures .....	2
1.3 Problem Statement .....	4
1.4 Justification .....	7
1.5 Objectives of the study .....	8
1.6 Significance of the project study .....	9
<b>CHAPTER TWO .....</b>	<b>11</b>
<b>LITERATURE REVIEW .....</b>	<b>11</b>
2.1 Introduction .....	11
2.2 Slope Stability .....	11
2.2.1 Soils, Soil Mechanics and Mass Wasting Processes .....	11

2.2.2 Factors Affecting Slope Stability.....	13
2.2.3 Slope Forms and Failure Modes .....	15
2.3 Landslides.....	16
2.3.1 Overview of landslide processes.....	16
2.3.2 Types of Landslides .....	17
2.4 Effect of water content on the stability of slopes .....	18
2.5 Appraisal of Slope Stability Analysis Methods .....	20
2.5.1 Background .....	20
2.5.2 Classical Limit Equilibrium Methods .....	21
2.5.3 Finite Element Methods.....	23
2.5.4 Probabilistic Methods .....	25
2.6 Slope Monitoring.....	26
2.6.1 Overview .....	26
2.6.2 Slope monitoring methods .....	28
2.7 Artificial Neural Networks (ANN) .....	30
2.7.1 Introduction.....	30
2.7.2 ANN Basics .....	31
2.7.3 ANN Architectures .....	33
2.7.4 ANN Models .....	35
2.7.5 ANN Model Development.....	37
2.7.6 Application of ANNs in Slope Stability Analysis .....	39
<b>CHAPTER THREE .....</b>	<b>41</b>

**SLOPE STABILITY MODEL FORMULATION AND EXPERIMENTAL SETUP**

.....	<b>41</b>
3.1 Introduction .....	41
3.2 Study Area.....	42
3.3 Numerical Formulation .....	43
3.3.1: Overview.....	43
3.3.2 Spherical-cap-shaped slope morphology under planar translational failure	45
3.3.2.1 Introduction.....	45
3.3.2.2 Numerical Model Formulation .....	45
3.3.2.3 Experimental setup and design .....	50
3.3.3 Double-Spherical-Cap-Shaped Slope Morphology Under Planar Translational Failure .....	54
3.3.3.1 Introduction.....	54
3.3.3.2 Numerical Model Formulation .....	55
3.3.3.3 Experimental setup, design and assumptions.....	58
3.3.4 Hydromechanical Landslide Model.....	59
3.3.4.1 Introduction.....	59
3.3.4.2 Numerical Model Formulation .....	60
3.3.4.3 Experimental setup, design and assumptions.....	64
3.4 ANN model .....	65
3.4.1 Introduction.....	65
3.4.2 ANN model formulation .....	65
<b>CHAPTER FOUR.....</b>	<b>69</b>

<b>RESULTS AND DISCUSSION .....</b>	<b>69</b>
4.1 Introduction .....	69
4.2: Numerical Results, Experimental Validation and Discussion .....	70
4.2.1: Spherical-cap-shaped slope morphology under planar translational failure	70
4.2.1.1: Overview.....	70
4.2.1.2: Results and Discussion .....	70
4.2.1.3: Summary, Conclusion and Recommendations .....	79
4.2.1.4 Novelty in the formulation.....	81
4.2.2 Double-Spherical-Cap-Shaped Slope Morphology Under Planar Translational Failure .....	81
4.2.2.1: Overview.....	81
4.2.2.2: Results and Discussion .....	82
4.2.2.3: Summary, Conclusion and Recommendations .....	93
4.2.2.4 Novelty in the formulation.....	93
4.2.3 Hydromechanical Landslide Model.....	94
4.2.3.1 Overview.....	94
4.2.3.2 Research output and Interpretation .....	95
4.2.3.3 Summary, Conclusion and Recommendations .....	100
4.2.4 ANN Model Results.....	104
4.2.4.1 Overview.....	104
4.2.4.2 Results and Validation .....	105
4.2.4.3 Summary, Conclusion and Recommendations .....	112
<b>CHAPTER FIVE .....</b>	<b>114</b>



<b>CONCLUSIONS AND RECOMMENDATIONS.....</b>	<b>114</b>
5.1 Introduction .....	114
5.2 Contributions of the study .....	114
5.3 Recommendations for Further Research .....	119
5.4 Limitations of the study.....	119
5.5 Concluding remarks .....	120
<b>REFERENCES.....</b>	<b>122</b>
<b>APPENDICES.....</b>	<b>158</b>
Appendix I: Table showing a section of the normalized data in the range -1 to +1 to be fed in the ANN for analysis (Pre-processing of data) .....	158
Appendix II: A section of the Input, Target, Forecast, Relative Error and Performance Estimate data table during training of the ANN.....	159
Appendix III: Budget Estimates .....	160
Appendix IV: Time schedule of events.....	162
Appendix V: Similarity Report .....	163

## LIST OF TABLES

Table 2.1: Types of landslides [Modified from updated version of Varnes' classification of slope movements (Hung et al., 2014)] .....	18
<i>Table 2.2: An outline of landslide features analysed using geophysical methods (Whiteley et al., 2019)</i> .....	<b>31</b>
Table 4.1: Summary of geotechnical parameters.....	83
Table 4.2: Physical properties of the soil samples (before the experiment) .....	95
Table 4.3: Descriptive statistics of the variables used in the model development ...	107
Table 4.4: Summary of the number of training and test sets as well as error estimates from the observed data .....	107

## LIST OF FIGURES

Figure 1.1: Landslide mitigation methods [modified from Fayne <i>et al.</i> , (2019), Santi <i>et al.</i> (2011) and Anderson and Holcombe (2013)] .....	5
Figure 2.1: Modes of slope failure (Source: <a href="https://theconstructor.org/geotechnical/slope-failures-types/28467/">https://theconstructor.org/geotechnical/slope-failures-types/28467/</a> , accessed 04/04/2020) .....	15
Figure 2.2: Typical landslide morphology (Source: Highland and Bobrowsky, 2008)....	17
Figure 2.3: Landslide causative factors .....	17
Figure 2.4: Common slope stability analysis methods [modified from Duncan (1996)] .	21
Figure 2.5: Factor of safety definitions (Abramson <i>et al.</i> , 2002) .....	24
Figure 2.6: Design of a geodetic monitoring network (Welsch <i>et al.</i> , 2000).....	29
Figure 2.7: Artificial Neuron Model (modified from McCulloch and Pitts, 1943) .....	33
Figure 2.8: General configuration of a three-layered feed-forward artificial neural network (Caner <i>et al.</i> , 2011) .....	36
Figure 3.1: Schematic illustration of a spherical-cap-shaped slope section (shaded) and an extract of the inertial forces acting on it .....	48
Figure 3.2: SPM system setup (schematic diagram and picture).....	52
Figure 3.3: SPM flowchart.....	53
Figure 3.4: A section of a concave shaped rigid-perfectly plastic soil mass on a slope with an exploded view of the shaded part of the slope indicating Inertial forces acting on the soil mass.....	57
Figure 4.1: Results of computational and experimental (a) Rainfall intensity; (b) Pore-pressure; as a function of time in minutes. Inset: statistical analysis.....	72

Figure 4.2: Computational and experimental results of (a) Water content; (b) Displacement; varying with time in minutes. Inset: statistical analysis .....	76
Figure 4.3: Computational and experimental FS results with time .....	77
Figure 4.4: Computational and experimental results of the volumetric water content as a function of time (Inset: statistical analysis) .....	85
Figure 4.5: Variation of pore-water pressure with time (Inset: statistical analysis) .....	86
Figure 4.6: Pore-water pressure profile as function of with time for a soil slope (Inset: statistical analysis) .....	88
Figure 4.7: Factor of safety (model and experimental) profiles for different angles as a function of time.....	91
Figure 4.8: Plot of (a) volumetric water content (VWC) and (b) pore-water pressure (PWP) with time .....	96
Figure 4.9: Characteristics of the factor of safety for slope angles (a) 30°, (b) 40°, (c) 50°, (d) 60° and (e) 70° with time under wetting conditions. Inset: Statistical comparison between model and experimental data for correlation purposes.....	102
Figure 4.10: Variation relative displacement with time.....	103
Figure 4.11: ANN structure .....	106
Figure 4.12: Absolute error between the actual and forecasted values for each row .....	108
Figure 4.13: Comparison between actual and forecasted values for the training session	108
Figure 4.14: Input importance by percentage to the target .....	110
Figure 4.15: Comparison of actual and predicted factor of safety for validation dataset	112

## LIST OF ABBREVIATIONS, ACRONYMS, AND SYMBOLS

$\phi''$	friction angle with respect to changes in matric suction
$\rho_{XY}$	coefficient of correlation of a pair of random variables $X$ and $Y$
$c'$	cohesive stress
$\phi'$	effective internal angle of friction
$\sigma'$	effective normal stress
$\sigma_x$	standard deviation
$\gamma_d$	dry unit weight
$\tau_d$	shear stress
$\gamma_e$	effective unit weight
$\sigma_n$	normal stress
$\tau_r$	shear strength
$\mu_x$	the mean of a random variable ( $x$ )
$a$	ANN output
ANN	Artificial Neural Networks
$b$	bias value ANN
$COV$	coefficient of variation
$e$	void ratio
$E[x]$	expected value of a random variable ( $x$ )
$f$	ANN transfer function
$f(x)$	probability density function
FFNN	Feedforward Neural Network
FS	Factor of Safety

$G$	specific gravity
$h$	saturated thickness of the soil above the failure plane
$L$	length of sliding plane
$m$	wetness index
$MAE$	mean absolute error
MLP	multi-layer perceptron
MNN	Modular Neural Network
$N$	normal force
$n$	soil porosity
$p$	input ANN network
PWP	pore-water pressure
$q$	weight on the soil surface by vegetation or structures
$r$	correlation coefficient
RBF	Radial basis function Neural Network
$RMSE$	root mean squared error
RNN	Recurrent Neural Network
$S$	degree of saturation
$u_a$	pore-air pressure
$u_w$	pore-water pressure
$VAR[x]$	variance of a set of random variables
VWP	volumetric water content
$w$	synaptic weight to ANN
$W$	weight of slope material

$\alpha$	slope angle
$\gamma_m$	moist unit weight
$\theta$	volumetric moisture content
$\theta_s$	saturated volumetric water content,
$\psi$	soil suction
$\psi_r$	residual soil suction

## ACKNOWLEDGEMENTS

*For the LORD is the great God, the great King above all gods.*

*In his hand are the depths of the earth, and the mountain peaks belong to him.*

*The sea is his, for he made it, and his hands formed the dry land.*          Psalms 95:3-5.

I wish to acknowledge with utmost appreciation the selfless efforts, professionalism, strict derivation, guidance, support and mentoring extended to me by my supervisors Prof. W. Ng’etich and Prof. S. Rotich regarding the theory, experiment and write-up of this dissertation. Words only cannot express their contributions of talent, extreme patience, enlightening instruction, dedication and time given unselfishly. Special thanks to Prof. Ng’etich for his technical insight, careful appraisal of my manuscripts and for all the helpful suggestions concerning the direction and execution of this research work.

The support extended to me by the entire department of physics is sincerely acknowledged. The input and company of my course mate Kosgei as well as my mentors in the department especially Prof. J. Tonui, Prof. Mwamburi, Dr. K. Muguro, Dr. Z. Mapelu, Dr. C. Ronno, Dr. N. Makau Dr. D. Cherus and Dr. D. Waswa cannot be overstated. Their advice and encouragements are sincerely treasured. I acknowledge with love my entire family especially my wife Judy and children who patiently provided the much-needed encouragement during the hard times of my academic life. The efforts of all those who have assisted me in one way or another are highly appreciated. May God Most High bless you abundantly.



## CHAPTER ONE

### INTRODUCTION

#### 1.1 General Introduction

Generally, the lithosphere is not static and stable but rather it is in a dynamic and incessant state of motion leading to deformations either horizontally, vertically or both due to forces emanating from the Earth's inner molten core, variations in the ground water level, tectonic phenomena as well as mass wasting events. Additionally, wind, rain, rivers and human activities continually modify the Earth's surface (Turcotte and Schubert, 2002). Movements of the lithosphere are responsible for all geological processes ranging from volcanoes, earthquakes and mountain ranges, as well as the shape and location of continents. A number of these geological processes account for rampant natural hazards and ecological challenges experienced across the globe (Alaniz et al., 2019; Qin et al., 2018).

Natural cataclysms either of meteorological nature (droughts, cyclones, etc.) or bearing geological dimensions (avalanches, rock falls, etc.) have been acclaimed to cause confounding effects on humans, economies and environment. Many people and communities in the past few years have become more susceptible to natural upheavals but the risk varies from one region to another depending on the predisposing conditions. While the frequency of these occurrences has been increasing gradually, manmade activities have worked to elevate their magnitude, direction and duration. Recent studies have shown that global climate change, population growth and urbanization have immensely increased the degree of vulnerability, frequency and intensity of natural calamities (UNDRR-ISC, 2020; WCDR, 2005).

Most of these geological disasters occur in slanting areas which are considered as ecologically active zones where many infrastructural activities such as road

construction projects, property development, tourism and agricultural practices are prioritized (Ercanoglu and Gokceoglu, 2002). Mass wasting disaster risks are rampant in hilly environments due to slope instability and liquefaction especially during heavy rainfall storms (Baharuddin *et al.*, 2016; Miles and Keefer, 2001).

Slope instability arising from geophysical and hydrological factors on both natural and engineered slanting soil masses is an inherent problem to both civil and geotechnical professionals as well as geophysicists whose solution is a panacea to many researchers, development stakeholders and the community at large. Generally, many slopes become unstable due to increased rainfall intensity and duration, changes in ground water levels, loss of shear strength and abrupt modification of slope geometry (Thielen *et al.*, 2005; Abramson *et al.*, 2002). Earthquakes as well as inappropriate land use practices and other unsustainable anthropogenic activities have also been cited as significant predisposing factors (Singh *et al.*, 2016).

## **1.2 Slope stability – risk, investigation and mitigation measures**

Most mountainous or generally highland regions are usually exposed to soil mass movements throughout their history in varying magnitudes, occurring either at a smaller scale of very short distances (typically a few centimetres per year) and usually un-noticeable, or in other cases involving very large volumes of debris and travelling long distances causing havoc. These movements constitute the largest number of geological disasters, for which debris flows and landslips are the most dominant (Kirschbaum *et al.*, 2015).

Notably, over the last few years, the world has witnessed an upsurge in the number and frequency of these hazards as witnessed from both media and research reports (Froude and Petley, 2018). Globally, an average \$1-5 billion is lost in many countries

in addition to thousands of injuries and around 600 deaths in total per year, as a result of landslides only (Highland and Bobrowsky, 2008). While climate change is cited as the most probable factor for this steady rise in this kind of natural hazards, there has been an upsurge of anthropogenic impacts escalating the risk at an alarming rate (McColl, 2015). The affected population and the damages incurred usually depends on the duration, magnitude and spatial extent as well as on the vulnerability of the exposed location (Dussauge-Peisser et al., 2002).

In Kenya, the number and frequency of soil mass wasting occurrences has been on the rise especially landslide events concentrated in the Central and North-Western highland regions (Ministry of State for Special Programmes, 2009; Ngecu *et al.*, 2004). For instance, in the then Kakamega North District (now Malava subcounty), 13 people died, 26 people injured and an undetermined number displaced on 12<sup>th</sup> August 2007, when a devastating mudslide swept down the Nandi escarpment in Khuvasali village (<https://www.nation.co.ke/news/1056-201434-lvds5gz/index.html>, accessed 15/04/2020). Additionally, in Kairo Village (Muranga County), a deformed landscape following a landslide caused by a heavy downpour was witnessed on 10<sup>th</sup> October 2019, causing massive damage to farmlands. In November 2019, West Pokot county was hit with a series of landslide events that left 53 residents dead while approximately 22,000 more were seriously affected and displaced from their homesteads in Parua, Nyarkulian and Muino villages (<https://citizentv.co.ke/news/photos-west-pokot-landslide-the-aftermath-305535/>, accessed 14/01/2020).

Slope stability studies are undertaken by various stakeholders so as to appreciate and gain a holistic understanding of slopes as ecological localities or construction sites as well as foundation for transport networks such as railways and roads. Slope stability investigations are generally aimed at identifying the causes of instability and

triggering factors in addition to post-failure mitigation countermeasures. These analyses involve static, dynamic, analytical or empirical methods to evaluate the stability of artificial and natural slopes. The most pertinent focus of any analysis is to ensure that slopes are both safe and economically sustainable (Santos *et al.*, 2019; Basahel and Mitri, 2017).

The stability of slopes is generally evaluated using the Factor of Safety (FS), computed as a ratio between the shear strength and the shear stress. The FS is significantly affected by a number of predisposing features or processes ranging from geological and hydrological effects to human interventions. Additionally, the properties of rock mass, slope geometry, state of stress, temperature, cracking, swelling, decomposition of clayey rock fills, creep under sustained loads, leaching, strain softening, weathering, cyclic loading and erosion also affect the stability status of slopes (McColl, 2015; Suh *et al.*, 2011).

In principle, a given slope is said to be globally stable if the FS is greater than unity, and vice versa. As a convention, FS values slightly greater than 1 indicate that the slope is marginally stable but requires urgent intervention, monitoring or amelioration. A number of such intervention activities and mitigation measures (Fayne *et al.*, 2019; Anderson and Holcombe, 2013; Santi *et al.*, 2011) are summarized in figure 1.1.

### **1.3 Problem Statement**

In the past few decades, a sizeable number of research works have been dedicated to studying slope dynamics. Most of these studies are based on pioneering models by Bishop (1955), Morgenstern and Price (1965) and Janbu (1973), for which the stability of any given slope is evaluated by way of its FS values (Najjar *et al.*, 1999).

However, in a number of practical scenarios, these models are inappropriate because of outright deviations from the ideal conditions, lack of adequate data and the inherent non-linearity in the input parameters (Shahin *et al.*, 2001). In addition, since a large number of input parameters are required during computation, conventional models are inadequate in terms of reconciling slope geometry and geophysical properties (Clare *et al.*, 2018).

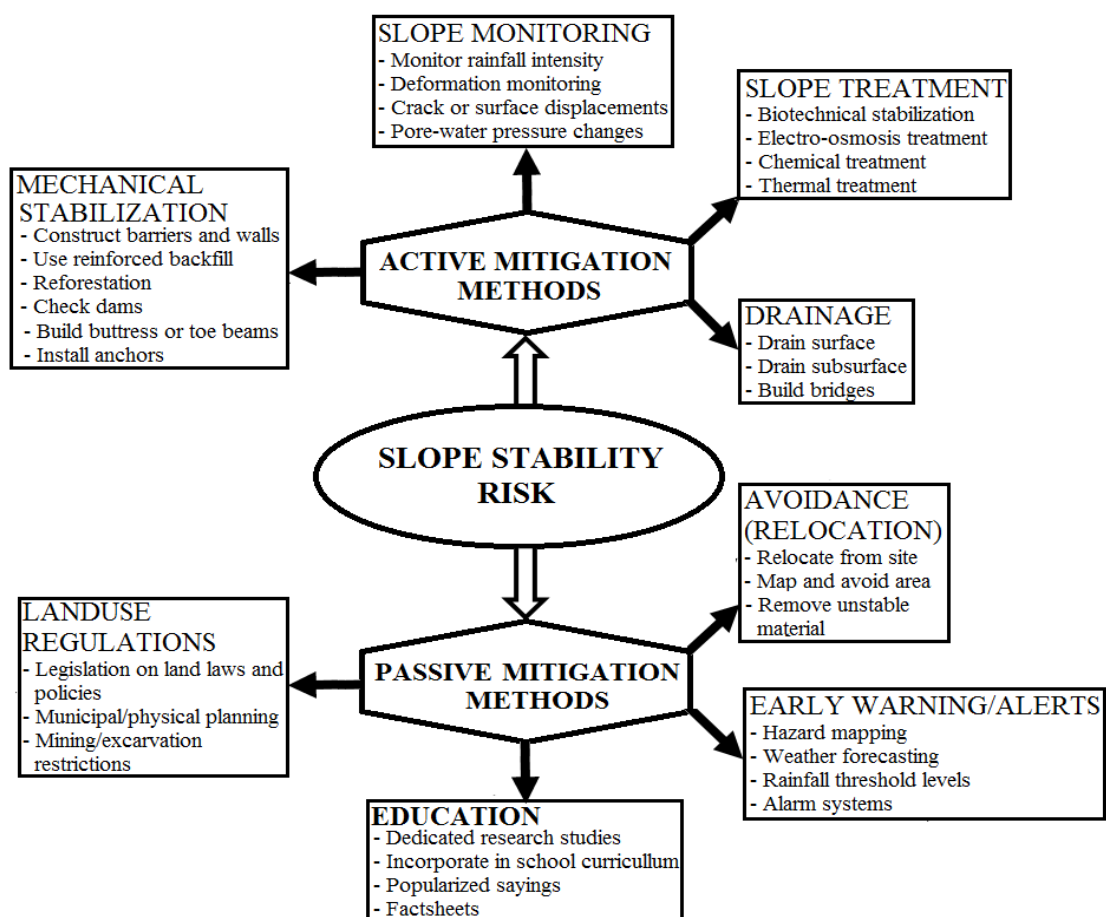


**Figure 1.1: Landslide mitigation methods [modified from Fayne *et al.*, (2019), Santi *et al.* (2011) and Anderson and Holcombe (2013)]**

Furthermore, majority of the existing numerical constitutive models are formulated based on subsurface hydrological processes while taking minimal attention in the conceptually important dynamics of geophysical aspects such as pore-water pressure

characteristics in the soil matrix (Serdarevic and Babic, 2019; Iverson *et al.*, 2001), slope profile as well as the morphology of the slip zone and sliding plane which dictates the mechanism of failure. While a number of research works have been focused on studying the pore-water pressure build-up and its impacts on slope health (Conte *et al.*, 2020; Chao and Ning, 2019; Fredlund *et al.*, 1978), slope configuration especially the slip zone morphology has not received serious consideration as a vital parameter in stability analysis.

Pioneering research works confirmed that the configuration of the slip surface is usually nonlinear and is a function of the conditions of soil properties, water content and slope angle (<https://theconstructor.org/geotechnical/slope-failures-types/28467/>, accessed 04/04/2020; Lanni, 2012; Arora, 2008; Morgenstern and Price, 1965). Nonetheless, most constitutive models in soil mechanics are derived based on the infinite slope configuration (also called surficial slide) which is formulated assuming that the slip plane is parallel to the slope surface and that the slip zone is planar or cuboidal in shape with infinite or unit width (Halty, 2014; Casadei *et al.*, 2003). Other constitutive models are derived based on the slip circle including the method of slices while assuming that the slip surface is purely circular. In summary, these models are formulated based on the assumption that the width of the sliding matter is of unit length (to simplify computations) (Tai *et al.*, 2020; Zheng *et al.*, 2020; Charles and Soares, 1984), leading to an erroneous computation of the total volume of the slip zone and resultant shear stresses.

Evidently, post-failure analysis of regions that have experienced mass wasting processes has revealed that the void left after slope failure (such as a landslide) resembles a section of a sphere especially for convergent slope forms. Even if curvilinear slip surface is mentioned in literature many times, there is no slope

stability model used to assess landslide susceptibility and hazard has considered a spherical-cap shaped soil mass as the slip zone.

As a consequence, the existing inadequacies in modelling soil slopes especially regarding the failure mechanism and morphology of the slip zone should be addressed by developing more descriptive constitutive equations with minimal assumptions. In essence, a combination of unsophisticated and more precise numerical models considering spherical-cap shaped slip zones, rigorous instrumentation systems for real-time monitoring, and the utilization of intelligent tools such as artificial neural networks (ANNs) for forecasting soil mass movements is inevitable (Kumar *et al.*, 2020; Carro, 2003).

Therefore, physical processes affecting the dynamics of soil slopes are studied with a view of developing numerical and intelligent artificial neural network models based on soil characteristics, hydrological and geomorphological factors that can be utilized in the characterization of natural and engineered slope sections. The models are then validated through rigorous experiments based on a laboratory flume.

#### **1.4 Justification**

The main motivation of slope stability analysis is to reduce the number of fatalities, reduce property damages and advance the scientific knowledge about these natural hazards. Slope stability evaluations are therefore performed for a wide variety of geophysical, civil engineering and academic applications. Some of these applications include determination of short- and long-term stability of both temporary and permanent cut-and-fill slopes, embankments, foundations for structures and retaining walls, assessment of slope stability under vibration processes such as seismic events

and lastly analysis of mechanisms, design procedures and mitigation techniques in cases of soil mass movements (Thennavan *et al.*, 2020; Bahareh *et al.*, 2018).

Furthermore, a comprehensive slope analysis framework that involves formulation of constitutive models which take into consideration all geotechnical and geophysical factors as well as geometric factors is inevitable (Halty, 2014; Gray, 2013). Therefore, a detailed study of landslide modelling, prediction techniques and mitigation measures are long overdue.

Rheological and constitutive models derived from rigorous experimental sessions serve as effective tools of analyzing slope material in a variety of physical scenarios. Artificial neural networks (ANNs) are employed to give more precise predictions/forecasting of imminent slope failure. Research findings can then be utilized to inform government, non-governmental organizations and other stakeholders to educate communities, prepare early warning alerts as well appropriate mitigation measures. The overriding goal of this study was to derive numerical and physical models, validate these models based on laboratory experiments and develop an artificial neural network model for prediction of slope failures.

### **1.5 Objectives of the study**

The overall objective of this research project is to perform an explicit characterization of convex configuration slopes under modest hydrological conditions. This involves development of constitutive models considering slopes with convex configuration morphology, design of a real-time monitoring system and development of an intelligent artificial neural network model to predict the occurrence of these processes both in space and time. Therefore, the study focused on the following specific objectives:



- (1) To formulate physically-based numerical and constitutive models to simulate the characteristics of shallow landslip processes for spherical-cap-shaped slip zones,
- (2) To formulate a hydromechanical model for shallow soil mass wasting processes,
- (3) To develop a solar-powered system for real-time monitoring, processing and transmission of slope geophysical and geotechnical parameters,
- (4) To develop, as well as train, test and validate an artificial neural network model to forecast slope stability characteristics.

### **1.6 Significance of the project study**

People obviously settle in sloping regions that are prone to soil mass movements because of the ever-increasing population, while farmlands, roads and other structures are constructed in such locations. As a result, massive damage to infrastructure accompanied by serious injuries or loss of lives are witnessed in events of slope failure (Zou *et al.*, 2018; Zhang *et al.*, 2015). The most common, prevalent and frequent types of slope movements in sloping regions are landslides and debris flows (Wu *et al.*, 2015). In the USA, the documented destruction caused by landslides is estimated to cost approximately \$3.5 billion per year in addition to about 20 - 50 deaths each year (<http://pubs.usgs.gov/fs/2004/3072/pdf/fs2004-3072.pdf>, accessed 21/03/2020; National Research Council, 2004). In Central America, about 2730 people died in 128 landslides between 2004 and 2013 (Sepulveda and Petley, 2015). Recently, a couple and their two children were buried by the debris inside their house in the village of Turung, Marakwet East Constituency, Elgeyo-Marakwet County, Kenya (<https://www.nation.co.ke/counties/elgeyo-marakwet/Four-killed-inMarakwet-landslide/3444818-5316280-15446p9z/index.html>, accessed 20/10/2019). On the global scale, reports indicate that close to one thousand people lost their lives due to

debris flows and landslips (<https://www.aa.com.tr/en/environment/environmental-disasters-across-world-in-june-2020/1895500>, accessed 30/07/2020; Petley, 2012).

As a consequence, appropriate physically-based and numerical models as well as reliable instrumentation systems are expected to provide the necessary direction in slope analysis and policy making. In addition, the use of intelligent tools such as artificial neural networks for purposes of forecasting these catastrophies will aid in disaster preparedness and mitigation.

Therefore, all stakeholders including governments and the community at large require as a matter of necessity, an appraised information base about landslide processes especially in highland areas so as to make appropriate decisions and policies. This will go a long way in ensuring minimal disruption to both human activities and infrastructural installations (Morgan *et al.*, 1992). The acumens realized from the study will also be employed in the development of an early warning system, which emboldens the old adage "to be forewarned is to be forearmed".

## **CHAPTER TWO**

### **LITERATURE REVIEW**

#### **2.1 Introduction**

This chapter mainly focuses on an exposition of the general theoretical background regarding physical, geological and engineering principles behind soil mass movements as well as giving highlights on the methodological approaches employed in modelling, simulation, monitoring, early warning systems and artificial neural networks.

#### **2.2 Slope Stability**

##### **2.2.1 Soils, Soil Mechanics and Mass Wasting Processes**

Soils are composed of a heterogeneous mixture of solid particles (clay, silt, sand, and gravel), fluids (air, water) and organic matter. Soils are formed primarily from weathering of rocks (igneous, metamorphic or sedimentary). In other words, rocks split into minute units to create soil through the various weathering processes (biological, chemical, physical) or manmade activities (blasting, excavation, waste disposal) (Mitchell and Soga, 2005; Powrie, 2004).

Soil mechanics is a branch of physics which involves the analysis of dynamics, deformations and fluid flow within natural and engineered matrices of soil (Lambe and Whitman, 1991). Soil mechanics is geared towards solving three major stability problems i.e. earth pressures, bearing capacity and slope analysis. While each of these three branches involves the knowledge of the stress state of a soil mass, the differences amongst them lies in the boundary conditions imposed. For earth pressure problems, the soil mass is considered to be in a state of failure implying that the remedy lies in the computation of the external force required to maintain it in that

state. Bearing capacity problem arises from stresses induced by external loads on a soil mass such as foundations of structures and vegetation. Lastly, slope analysis is mostly confined to stresses induced by self-weight on the soil mass in a slanting position (Morgenstern and Price, 1965).

A soil slope is a slanting surface of soil mass either man-made or natural, whose stability depends on a number of internal and external factors. Slope instability usually occurs as a consequence of many predisposing factors principal among them being precipitation, seismicity and human activities. Slope instabilities always lead to mass wasting events that fall under the category of severe natural disasters on the earth's surface (Petley, 2009).

Mass wasting or mass movements (or sometimes referred to as slope movement) is defined as the geomorphic process by which soil, sand, or even rocks move downslope in the form of a continuous, discontinuous or solid lump, due to the action of gravitational force or an imposed external force ([https://en.wikipedia.org/wiki/Mass\\_wasting](https://en.wikipedia.org/wiki/Mass_wasting), accessed 24/10/2019). Mass movements are disastrous and intricate geological natural disasters occurring in many parts of the world, mostly highland areas and embankments. There exist many types of mass movements and are distinguished based on the manner in which the rock, regolith, or soil moves down the slope. In the category of rapid movements are landslides, rock falls, slumps, rockslides and debris flows or mudflows, while slow movements includes creep and solifluction (<http://pubs.usgs.gov/fs/2004/3072>, accessed 24/10/2019; Hungr *et al.*, 2014).

### 2.2.2 Factors Affecting Slope Stability

Slope failures occur when either shear stresses and gravity exceed the mobilized shear strength, or when certain external and internal factors that lead to an increase in the shear stresses or a decrease in the shear strength. Factors that affect the shear strength of slope materials include pore-water pressure, presence of cracks, type of soil, etc. On the other hand, shear stresses are affected by additional loads on top of the slope, excavation or erosion at the toe, rise in soil weight, pressure in cracks, and seismic events (Lupiano *et al.*, 2019; Bordoni *et al.*, 2015).

The destabilizing factors to slopes are classified into three main categories. First, are the preparatory factors that cause the slope to be vulnerable to movement such as soil texture and rock type. Secondly, are the triggering factors which are responsible for initiating motion such as high intensity precipitation or seismic events. Finally, perpetuating factors, which dictate the characteristics and nature of projection for instance topographic factors. In combination, these three factors control the nature, intensity and rate of these movements in space and time (Ma *et al.*, 2019; Crozier 1986).

Overall, slope stability is dependent on material properties, state of stress and slope geometry. Amongst other factors, the most significant parameters that influence the stability status of slopes include:

- (i) **Geological discontinuities:** Slope stability is directly dependent on the structural discontinuity in the rock in which the slope is excavated. The properties of discontinuities such as orientation, persistence, roughness and infilling dictate the type of slope failure and can exist in form of cracks, schistosity, bedding planes, joints, fault planes, fractures, fissures, or cleavages. The orientation of geological discontinuities relative to engineering structures determines the stability

conditions of the slope material. The mutual orientation of discontinuities determines the shape of the individual blocks.

- (ii) **Slope Geometry:** Slopes with higher gradients are considered steeper and vice versa. Steeper slopes pose a greater risk of instability and eventual failure because of higher tangential gravitational force. Slope materials will tend to move downslope either naturally on their own under gravitational force or when disturbed until an appropriate angle of repose is attained. Therefore, the slope angle is the principal factor determining slope stability in all geological and hydrological conditions.
- (iii) **Effect of water:** Presence of water in slopes can serve to stabilize or to destabilize a slope depending on its volumetric content. Moderate water content leads to increased soil cohesion and consequently higher shear strength. Excessive water destabilizes the slope by adding weight, destroying cohesion between grains, and reducing friction, thereby diminishing the shear strength of the soil mass.
- (iv) **Vegetation cover:** The type and percentage of vegetation on a slope determines its shear strength. Root cohesion and controlled erosion are positive effects that plants offer to slopes.
- (v) **Geotechnical parameters:** These factors determine the cohesive stress, the magnitude of the confining pressure, strain rate, effective stresses, shear strength, internal friction angle of the slope and by extension, the factor of safety.
- (vi) **Anthropogenic factors:** A number of human activities are known to directly cause instability and failure of slopes. These activities include surface or groundwater rechannelling, blasting, deforestation, etc (Riquelme *et al.*, 2016; <http://www.soilmanagement-india.com/soil/slope-stability/stability-of-earth-slopes-soil-engineering/14489>, accessed 04/04/2020).

### 2.2.3 Slope Forms and Failure Modes

Slope stability is an important factor that should be considered during design and planning of environmental roadmaps, agricultural activities, civil and structural developments. Whenever slope failures occur, they are accompanied with a number of negative effects on the environment and the community. Amongst other geophysical factors, slope form is the most important factor that influences the mechanism or mode of failure. The three dominant slope forms observed in contour direction are convex (divergent) straight (planar) and spoon-shaped (concave). The combination of steep slopes and convergent topography has the highest potential for mass wasting (Halty, 2014; Gray, 2013).

There are several modes of slope failure ranging from translational, wedge, rockfall to rotational (circular/non-circular) and compound failure types (figure 2.1). The mode of failure largely depends on the material properties, water content and foundation strength (Arora, 2008). Translational failure occurs mostly in infinite slopes where the slip plane is parallel to the slope gradient. This type of failure is common in slopes composed of stratigraphic layers.

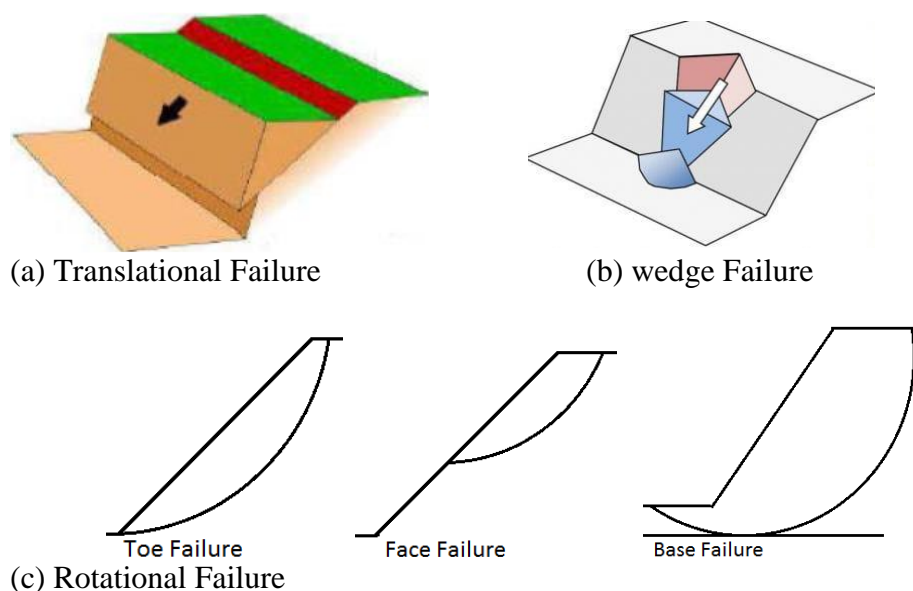


**Figure 2.1: Modes of slope failure (Source: <https://theconstructor.org/geotechnical/slope-failures-types/28467/>, accessed 04/04/2020)**

Wedge (block) failure occurs when distinct wedge-like blocks of soil mass become separated from the rest of the earth slope and move downslope. This type of failure occurs in both infinite and finite slopes made up of heterogeneous materials or in a slope with discontinuities.

Rotational failure occurs by a gyration of the unstable mass of soil along a failure surface by the downward and outward movement of soil, for which the slip surface is generally curved i.e. circular for homogeneous soils and non-circular for non-homogeneous conditions.

Lastly, compound failure is a combination of all the other types i.e. translational and rotational failure. The failure surface can be flat or curved depending on the properties and conditions of the soil beneath or adjacent layers (<https://theconstructor.org/geotechnical/slope-failures-types/28467/>, accessed 04/04/2020; Morgenstern and Price, 1965).

## **2.3 Landslides**

### **2.3.1 Overview of landslide processes**

Landslides or landslips are among the dominant types of slope movements. A landslide is the motion of soil, rock or debris downslope due to influence of gravitational force or ground vibration (Cruden and Varnes, 1996). A comprehensive exposition of the factors causing landslips are discussed by Varnes (1984), Crozier (1986), Hutchinson (1988) and Hungr *et al.* (2014).

Majority of landslide phenomena occur in regions of the earth surface exposed to destabilizing conditions such as intensive rainfall and seismic events. Landslide processes encompass a wide range of ground movements including rock falls, deep failure of slopes and shallow debris flows. They can occur in coastal, offshore and



onshore environments (Deschamps and Leonards, 1992). Figure 2.2 depicts a graphic illustration of an idealized landslide morphology (<http://pubs.usgs.gov/fs/2004/3072>, accessed 24/10/2019). In general, landslides are caused by either natural, manmade or a combination of these factors as summarized in figure 2.3.

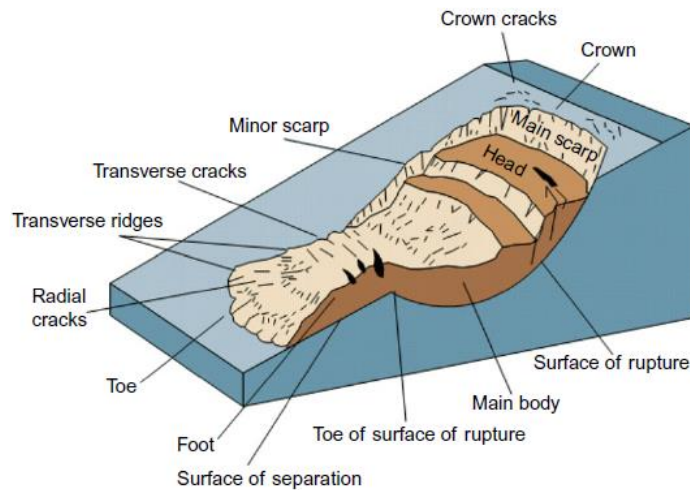


**Figure 2.2: Typical landslide morphology (Source: Highland and Bobrowsky, 2008)**

### 2.3.2 Types of Landslides

Landslide processes manifest in different forms differentiated by the mode of movement, rate of movement and kind of material involved (Varnes, 1978). The basic outline of the different types of landslides is presented in table 2.1 below.

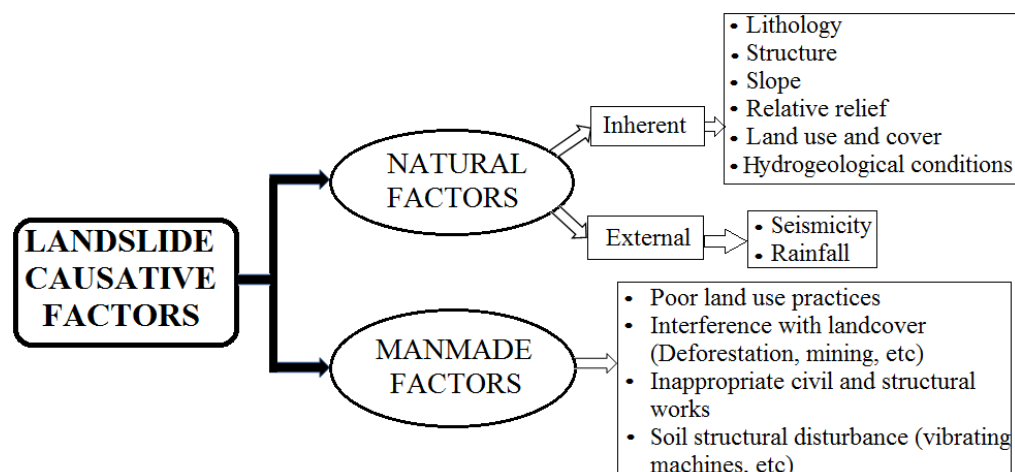


**Figure 2.3: Landslide causative factors**

**Table 2.1: Landslide types [Modified from classification of slope movements by Varnes' (Hungri et al., 2014)]**

<b>Type of movement</b>	<b>Rock</b>	<b>Soil</b>
Fall	Rock/ice fall	Boulder/debris/silt fall
Topple	Rock block topple	Gravel/sand/silt topple
	Rock flexural topple	
Slide	Rock rotational slide	Clay/silt rotational slide
	Rock planar slide	Clay/silt planar slide
	Rock wedge slide	Gravel/sand/debris slide
	Rock compound slide	Clay/silt compound slide
	Rock irregular slide	
Spread	Rock slope spread	Sand/silt liquefaction spread
		Sensitive clay spread
Flow	Rock/ice avalanche	Sand/silt/debris dry flow
		Sand/silt/debris flowslide
		Sensitive clay flowslide
		Debris flow
		Mud flow
		Debris flood
		Debris avalanche
		Earthflow
Peat flow		
Slope deformation	Mountain slope deformation	Soil slope deformation
	Rock slope deformation	Soil creep
		Solifluction

#### **2.4 Effect of water content on the stability of slopes**

Slope instabilities especially in hilly environments have been found to occur as a result of a combination of hydrological and geophysical factors ranging from pore-water pressure change, reduction in cohesive strength and internal angle of friction to infiltration-induced interflow along the soil–bedrock interface (Zhao and Zhang, 2014). Fang *et al.* (2012) underscored the fact that most shallow landslides occur because of an upsurge in pore-water pressures leading to a corresponding reduction in the shear resistance.

Water that affects the stability of slopes originates from two sources i.e. ground or aquifer water below the surface that generates pore-water pressures and, rainwater infiltration that seeps through the surface and flows along the slope generating water pressure (Brady and Brown, 2004). Water pressure acting within a discontinuity reduces the effective normal stress acting on a given plane, thus reducing the shear strength along that plane, consequently lowering the stability condition of natural or artificial slopes. The percentage of water content in the soil or rock material depends on a number of geotechnical, hydrological, and geological aspects such as soil permeability, rate of surface irrigation, intensity and duration of rainfall (Ng *et al.*, 2001).

Generally, the stability of most slopes is weakened when large amounts of water enter into the unsaturated soil matrix via infiltration leading to full saturation or liquefaction (Zhang *et al.*, 2018; Ray *et al.*, 2010). Such failures usually occur in areas where intense rainfall events are witnessed. Slope stability can also be compromised by the build-up of excess pore-fluid pressures arising from hastened infiltration rate especially in undrained and unsaturated soils. External loads applied on the soil surface usually set up destabilizing stresses within the slope mantle. Results from other research studies indicated that soil water decreases the shear strength lubricating the soil grains and reducing basal friction. Additionally, rainfall water or snow melt leads to a significant increase in the weight of the slope material thus increasing the effective stress (Kristo *et al.*, 2017; Kilburn and Petley, 2003).

Additionally, water content controls the angle of repose of unconsolidated sediments. Unconsolidated material with relatively low water content will exhibit a very high angle of repose as opposed to a saturated material. This is as a result of capillary attraction forces leading to surface tension that tends to hold the wet material together

as a cohesive unit. On the other hand, for a saturated material, the water molecules between the grains eliminates grain to grain frictional contacts thereby reducing the angle of repose reduces substantially (Sidle and Bogaard, 2016; Terzaghi, 1960).

While high intensity, short duration rainfall events are known to trigger soil mass movements, even long duration, low intensity rainfall and rapid snow or ice melt have also been found to activate landslides (Guzzetti *et al.*, 2009). In analysing landslide processes, two methods are preferred. The first approach employs statistical inferences to establish the relationship between rainfall characteristics and landslide event probability while the second method employs physical mechanisms of the rainfall infiltration or soil water content variation to trigger landslide events (Zhang *et al.*, 2018; Conte *et al.*, 2017; Wu *et al.*, 2015; Springman *et al.*, 2013).

## **2.5 Appraisal of Slope Stability Analysis Methods**

### **2.5.1 Background**

The main objective of slope stability analysis is to gain background knowledge on the precursors, nature and triggers of mass wasting events as well as mitigation measures. The analytical method used at any given time depends on the kind of data, availability, scale, reliability and in-situ conditions, as well as the purpose of analysis (Salunkhe *et al.*, 2017).

A comprehensive slope stability analysis method incorporates the evaluation of various design parameters such as slope angle, slope height, internal friction angle and construction or excavation sequencing. The inspiration behind any analysis is to give guidance on the utilization of slopes safely and economically (Huang, 2014).

Owing to the current interest in highland regions for purposes of building settlements and other infrastructural developments, both governments and local communities

require a detailed analysis of slope dynamics. Many researchers and geotechnical professionals have strived for many years proposing models and postulates relating certain physical parameters to the stability state of slopes. The two most common slope stability analysis methods are Limit Equilibrium (LE) and Finite-Element (FE) presented by Duncan (1996), but there exist other methods which were proposed in the latter years (Ishak and Zolkepli, 2016). A schematic representation of the different slope stability analysis methods is illustrated in the figure 2.4. The following sections give an outline of some of the methods that have been proposed over the years in the analysis of slope stability.

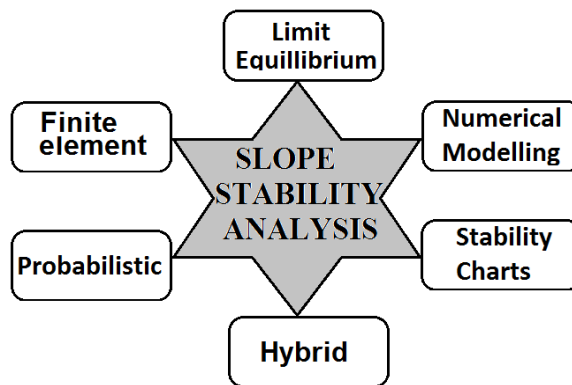


**Figure 2.4: Common slope stability analysis methods [modified from Duncan (1996)]**

### **2.5.2 Classical Limit Equilibrium Methods**

The most commonly used and well documented slope stability analysis methods fall under the large category of Limit Equilibrium (LE) methods. LE methods employ the Mohr-Coulomb criterion which involves solving instability cases by assuming force and/or moment equilibrium. These methods include the ordinary method of slices (Fellenius, 1936), Bishop's modified method (Bishop, 1955), force equilibrium methods (Lowe and Karafiath, 1960), Morgenstern and Price's method (Morgenstern and Price, 1965), Spencer's method (Spencer, 1967) and Janbu's generalized

procedure of slices (Janbu, 1973). All these methods were used to develop slope stability charts, though currently computer algorithms are used instead.

LE methods employ the Mohr-Coulomb criterion to compute the shear strength ( $\tau_r$ ) along the slip surface of a given soil sample, while the mobilized shear stress ( $\tau_d$ ) is defined in terms of the shear strength if the limit equilibrium state exists (Janbu, 1973). The shear strength is a function of soil type as well as the cohesive stress ( $c'$ ), effective normal stress ( $\sigma'$ ) and effective internal angle of friction ( $\phi'$ ) according to equation (2.1):

$$\tau_r = c' + \sigma' \tan \phi' \quad (2.1)$$

The mobilized shear stress on the other hand will therefore be defined by

$$\tau_d = \frac{\tau_r}{FS} = \frac{c' + \sigma' \tan \phi'}{FS} \quad (2.2)$$

where FS is the factor of safety.

Equation (2.1) is valid to fully saturated soils only. In contrast, for unsaturated soils, the Mohr-Coulomb failure criterion is modified as (Fredlund *et al.*, 1978):

$$\tau_r = c' + (\sigma_n - u_a) \tan \phi' + (u_a - u_w) \tan \phi'' \quad (2.3)$$

where  $u_w$  is the pore-water pressure,  $u_a$  is the pore-air pressure,  $\sigma_n$  is the normal stress, while  $\phi''$  is the internal angle of friction with respect to changes in matric suction (Fredlund and Rahardjo, 2014). The choice of shear strength equation to be used at any given time between equations (2.1) and (2.3) depends on the duration after excavation, soil type and loading conditions. Equation (2.1) is normally utilized for short-term conditions mostly in clay-rich soils, while equation (2.3) can be applied to all kinds of soils, long-term situations and in circumstances where the pore pressures are known (Pantelidis, 2009).

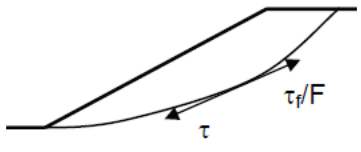
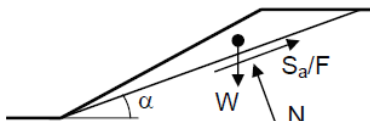
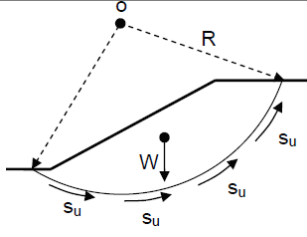
When employing the conventional LE methods, the slope stability is evaluated by the factor of safety (FS) at any given time. In these methods, the failure surface can bear planar, circular or non-circular configuration should be ascertained even if through assumption before the equilibrium analysis commences (Duncan, 1996). From the definition of FS, failure will occur when the shear strength which is assumed to be mobilized along a certain slip surface is exceeded. In this case, the FS is defined in three ways namely force, moment and limit equilibrium (Abramson *et al.*, 2002) as illustrated in figure 2.5.

In this consideration, LE analyses suffer from a number of limitations. Firstly, LE methods involve defining a critical sliding surface with minimum FS usually assumed to be circular except for slope material with geological layers in which case planar failure surface suffices (Duncan, 1996). However, post-failure investigations carried out at the sites of slope failure have indicated that the slip surface is not purely circular or planar as presumed in the LE approaches. Secondly, most LE analysis approaches are less accurate especially in the computation of the FS which is based on the preferred method of analysis and supposed mode of failure. Lastly, since LE analysis methods are anchored in a deterministic framework, there are errors in the chosen input parameters used in the calculation of FS (Chugh, 2002).

### **2.5.3 Finite Element Methods**

Finite element (FE) methods of stability analysis were developed to cure the inadequacies of LE methods. They are more accurate, adaptable, and require minimal theoretical assumptions regarding the slip surface and failure mode. They have also been used to precisely analyze slopes with asymmetrical boundaries and uneven potential/flow lines (Zaman, 2000; Griffiths and Lane, 1999). In general, the

advantages of FE methods over LE approaches range from the assumption of the slip surface, consideration of internal forces, and deformation process (Alemdağ *et al.*, 2015). FE methods can also be merged together with random field generators (RFG) to form the more versatile Random Finite Element Method (RFEM) which is used to analyze complex slope scenarios with spatially random soil properties (Baba *et al.*, 2012; Griffiths and Fenton, 2004).

	<p><b>Limit Equilibrium</b></p> $FS = \frac{S_u}{\tau_d} \quad \text{(Total Stress)}$ $FS = \frac{c' + \sigma' \tan \phi'}{\tau_d} \quad \text{(Effective Stress)}$
	<p><b>Force Equilibrium</b></p> $FS = \frac{\text{Sum of resisting forces}}{\text{Sum of driving forces}}$ $FS = \frac{S_a}{W \sin \alpha} = \frac{cL + N \tan \phi}{W \sin \alpha}$ <p>where <math>L</math> is length of sliding plane, <math>W</math> is weight of slope material, <math>N</math> is normal stress and <math>\alpha</math> is slope angle</p>
	<p><b>Moment Equilibrium</b></p> $FS = \frac{\text{Sum of resisting moments}}{\text{Sum of driving moments}}$ $FS = \frac{R \int_0^L S_u dl}{Wx}$

**Figure 2.5: Factor of safety definitions (Abramson *et al.*, 2002)**

FE methods are characterized by a variational formulation, a discretization plan, a solution algorithm and post-processing measures. In FE framework, the region to be analysed is divided into small elements joined together by nodes, and the displacements at each node are computed using calculus of variations to obtain stress and strain fields within the slope material (Logan, 2011).



Although FE methods have been adopted in the analysis of many geotechnical problems, they also suffer from a number of demerits. Firstly, they are time consuming especially during the development of models and computer algorithms. Secondly, they require advanced technical knowhow owing to the complex theory involved in the formulation of the models. Lastly, interpretation of the FE model results requires scholarly deduction (Duncan, 1996).

#### **2.5.4 Probabilistic Methods**

In the past few decades, probabilistic methods of analyzing slope stability have gained momentum in many research studies. The principal advantage of probabilistic methods over conventional LE and FE methods lies in the analysis of slope stability while taking into consideration the variability of soil physiognomies (Griffiths *et al.*, 2009). Additionally, probabilistic methods do not rely on the FS as the indicator of slope stability but rather employs the probability of failure or reliability index to evaluate slope health (Wolff, 1996; Mostyn and Li, 1993). There exist a number of probabilistic methods in use namely first order second moment (FOSM) method, Monte Carlo simulation (MCS) method, random finite element method (RFEM) and point estimate method (PEM).

While probabilistic slope stability analysis methods are comparatively more superior to conventional methods in terms of accuracy and versatility, there is a tendency to neglect the significant effects of soil variability. As such, inherent errors will be propagated in the computation of the probability of failure when spatial correlation of soil properties is not accounted for (El-Ramly *et al.*, 2002).

In probabilistic methods, parameters that influence the properties of soils are usually treated as random variables. In this case, the analysis shifts from a single deterministic

value to a range of values which constitute the probability density function (PDF). A number of statistical measures are employed in the analysis ranging from the mean, variance to standard deviation.

## **2.6 Slope Monitoring**

### **2.6.1 Overview**

The outer layers of the earth's crust are in continuous movement leading to deformations either horizontally, vertically or both due to physical aspects such as variations in the ground water level, tectonic phenomena and mass wasting events. The deformations can be monitored in sloping areas either in real-time or by remote sensing techniques so as to prevent or minimize the effects of these geologic hazards (Setan and Singh, 2001).

Slope monitoring is a vital tool for prevention and prediction whose potential must be appreciated by not only academic and engineering professionals but also non-technical and non-scientific stakeholders. Monitoring of slopes can prevent loss of life, infrastructure, and environment. Before any slope fails, there is usually measurable movement or small displacements and/or the development of tension cracks which act as precursors to imminent overall failure. It is documented that landslide occurrence is as a consequence of very small displacements over a very long period of time. However, these displacements can also be rapid in cases of ground vibrations such as during earthquake events (Ding *et al.*, 1998).

Monitoring involves the systematic observation and recording of the properties of a given system or process over time. In geotechnical analysis, the main focus is monitoring deformation, which involves regular tracking and measurement of the variations in the dimensions of a soil mass due to internal or external factors. The two

most common parameters monitored are displacement and groundwater levels, though most monitoring systems also incorporate other parameters such as erosion rate, pore-water pressure, cohesive stress, and vegetation cover in addition to historical information and geomorphology (Moore and Burchi, 1986).

Monitoring and data collection is a process which is normally implemented in five steps i.e. identification of monitoring objectives, establishing requirements, pinpointing the variables, actual measurement and recording of data as well as interpretation together with reporting of the results (Ding *et al.*, 1998). Generally, factors considered during the fabrication of a monitoring system include installation complexity, implementation, equipment selection and design specifications. Design specifications relate to the likely magnitudes of movement, parameters to measure, purposes of different instruments, type and scale of deformation to be monitored, locations of equipment and checks using different survey methods and equipment. Planning stage entails an outline of the design specifications together with the desired accuracy and precision. Design specifications give a detailed procedure and guide of attaining the intended objectives by giving a step by step direction on human resources, reporting methods, size and frequency (Pardo *et al.*, 2013).

A monitoring instrument can be packaged as a single sensor such as a vibrating wire piezometer or designed in form of a set of sensors bundled together into a single panel. Examples of instruments commonly used in deformation monitoring include theodolites, Global Positioning Systems (GPS) (Jeffreys, 2004) and total stations (Rueger *et al.*, 1994). On the other hand, remote sensing methods (Kaab, 2002) include satellite imaging (ASD-Network, 2006), laser (McIntosh and Krupnik, 2002), photogrammetric and radar surveys (GroundProbe, 2005; Anglo Coal and Reutech

Radar Systems, 2005). The following section gives a description of the common slope monitoring methods and interpretation of the results.

### **2.6.2 Slope monitoring methods**

Effective geotechnical monitoring of structures including slopes must incorporate the right design, compliance to legislation, system scaling and monitoring requirements. Each monitoring task has specific requirements depending on the application, versatility and accuracy. Generally, slope monitoring involves a multifaceted approach from civil and structural engineers, geologists, geophysicists and hydrologists (Wunderlich, 2004). Conventional slope monitoring devices or sensors are subdivided into four main classes i.e. geodetic, geotechnical, geophysical and remote sensing.

#### **1. Geodetic monitoring**

This involves accurate mapping and measurement of the Earth's fundamental properties such as movements or displacements in 1D, 2D or 3D (Dai *et al.*, 2016). In slope monitoring, geometric elements such as height differences angles, and displacements are measured. Fundamentally, geodetic monitoring systems are composed of an interconnected web of reference, object and observation networks (figure 2.6) (Voyat *et al.*, 2006; Welsch *et al.*, 2000). Basically, a reference network usually consists of stable control points and a multiplicity of witness points, located outside of the expected deformation area. The observation points which consist of sensors and transducers are placed either on the surface or inside the slope material being monitored. In other words, observation points are also known as measurement points. Finally, object points are used to discretize the slope. In most cases, the object

points are prismless tacheometry, terrestrial laser scanning or Global Positioning System (GPS).

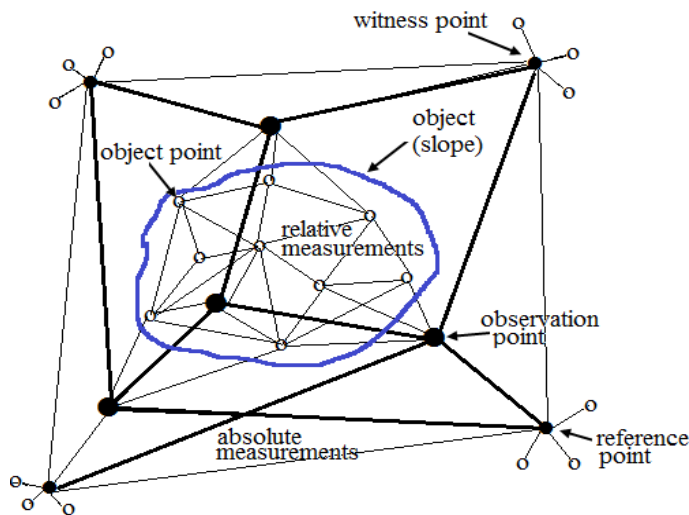


**Figure 2.6: Design of a geodetic monitoring network (Welsch et al., 2000)**

## 2. Geotechnical monitoring

Geotechnical monitoring generally deals with constant health check-up and observation of the ground behaviour and/or performance of structures such as slopes. The principal parameters of interest in geotechnical monitoring are ground water pressures, soil deformations and stresses. Instruments used include crackmeters, rain gauges, accelerometers, etc. (Diaz et al., 2018). A comprehensive discussion on geotechnical instrumentation is provided by Dunnicliff (1993), Sellers (2005) and McKenna (2006).

## 3. Geophysical monitoring

Geophysical monitoring entails systematic collection of data for spatial studies. Basically, gravitational and magnetic fields that originate from the interior of the Earth's regarding the internal structure and seismic activities. Geophysical measurements are focused on the variations of these electromagnetic and gravitational

waves in space and time. For instance, a gravimeter or a gravitational wave sensor as well as a magnetometer can be used to monitor changes in the gravitational and magnetic field (Mussett and Khan, 2000). Geophysical monitoring can provide information concerning temporal and spatial changes in a number of physical factors within a slope (Takahashi et al., 2006). The key factors that can be monitored using geophysical methods are listed table 2.2.

#### **4. Remote Sensing**

There are several remote sensing technologies employed for various purposes including Ground-based Radar Interferometry, Satellite-borne Radar Interferometry, Photogrammetry, and airborne laser scanning. Comprehensive literature on remote sensing techniques with regard to soil/rock mass characterization can be found in research publications such as Sturzenegger and Stead (2009), Warneke et al. (2007) and Tonon and Kottenstette (2007).

### **2.7 Artificial Neural Networks (ANN)**

#### **2.7.1 Introduction**

ANNs are sophisticated connectionist systems inspired by human brain used in computational processes to establish the relationships between certain inputs and outputs from experience (Chen et al., 2019; Tsangaratos, 2012). ANNs are machine learning algorithms capable of learning, recalling and generalizing. Generally, ANNs belong to a group of advanced modelling techniques which are capable of modelling extremely complex systems. In the past few decades, ANNs have been used to predict the outcomes of independent variables for different systems. In geophysics and geotechnical processes, ANNs are employed in prediction of the stability status of slopes. The most common ANNs used in solving geophysical problems are the multi-

layer perceptrons (MLPs) usually trained using back-propagation algorithm (Adeli, 2001; Shahin et al., 2001; Rumelhart et al., 1986).

**Table 2.2: An outline of landslide features analysed using geophysical methods**  
(Whiteley et al., 2019)

<b>Slope factor</b>	<b>Property contrast</b>	<b>Monitoring technology</b>
Landslide extents ( $x, y, z$ )	Slip surface (subsurface and surficial extent) caused by or indicated by changes in density, water content, etc., of material	Electrical resistivity, seismic reflection, seismic refraction, surface wave methods, ground-penetrating radar (Chambers et al., 2011)
Subsurface material type and structure	Material density	Microgravity (Sastry and Mondal, 2013)
	Relative degree of saturation	Electrical resistivity, electromagnetics (Springman et al., 2013)
	Relative clay content	Electrical resistivity, electromagnetics (Göktürkler et al., 2008)
	Material velocity (as a function of density)	Seismic reflection, seismic refraction, surface wave methods (Renalier et al., 2010)
Water table	Height of water table	Electrical resistivity, electromagnetics, seismic refraction (Le Roux et al., 2011)
	Relative flow direction	Self-potential (Perrone et al., 2014)
Tension features (e.g., surface fractures)	Saturation contrasts (e.g., preferential infiltration pathways)	Electrical resistivity, electromagnetics, ground-penetrating radar, self-potential (Bièvre et al., 2012)
Compression features (e.g., ridges)	Variations in material composition	Electrical resistivity, electromagnetics, ground-penetrating radar (Schrott and Sass, 2008)

### 2.7.2 ANN Basics

Rafiq et al., (2001) defines an ANN as “*a computational mechanism able to acquire, represent, and figure mapping from one multivariate space of information to another,*

*given a set of data representing that mapping*". It usually consists of numerous processing elements that are interconnected to each and working in collaboration to accomplish a given function.

ANNs are classified based on a variety of factors including training procedure and the number of layers. In terms of layers, they can be single or multi-layered. Based on training procedure, they can be classified under supervised or unsupervised training. In this case, unsupervised training means training an input data set without knowledge of the output. For supervised learning, training an input data set requires clear knowledge of the output and as such a comparison is made between the input and desired output (Adeli and Wu, 1998).

A general model of a single layer (or perceptron) consists of a single input and a single output. The product of the scalar input and the scalar weight together with a bias (offset) are fed to a summer, the result of which is sent into a transfer (activation) function producing an output (figure 2.7). Generally, the neuron output is calculated as

$$a = f(wp + b) \quad (2.11)$$

with  $a$  as the output,  $f$  is the transfer function,  $w$  is the weight,  $p$  the input and  $b$  is the bias value. If a single artificial neuron has more than one input, the dimensions of these inputs is represented by a vector, while the corresponding weights by a matrix. Transfer functions are either linear or nonlinear based on the nature of the problem under consideration. However, linear, hard-limit and log-sigmoid transfer function are commonly used (Anderson, 1995).



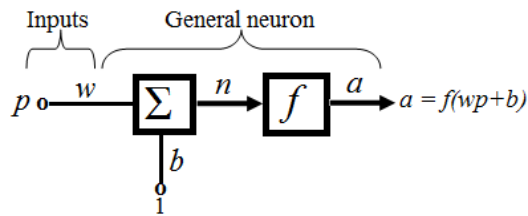


**Figure 2.7: Artificial Neuron Model (modified from McCulloch and Pitts, 1943)**

### 2.7.3 ANN Architectures

In a given network, a number of neurons can be combined to form layers. A complex network consists many interconnected layers. A layer consists of an output vector, transfer function, weight matrix, boxes, bias vector and summers. The different types of networks are classified according to the input characteristics and mathematical procedures required to compute the outcome. The most common ANN architectures include (Masri et al., 2000):

1. **Feedforward Neural Network** – FF-NN is the most basic form of ANN in which data processing is unidirectional i.e. data passes through the input nodes and exit on the output nodes. In other words, it has a front propagated wave and no back propagation by using a classifying activation function usually. This kind of ANNs are used in computer vision and speech recognition applications.
2. **Radial basis function Neural Network** – RBF-NN functions work by comparing the distance of a given point with the centre, similar to the radius and centre of a circle. The model relies on the radius which is usually a Euclidean function to classify points into categories. One advantage of RBF based ANNs lies in the ability to have a memory i.e. remembering the previous output that can then be fed in the next time-step. They are used mainly in power restoration systems.
3. **Kohonen Self Organizing Neural Network** – In this kind of ANN, the input vectors are organized into a discrete map referred to as Kohonen map. The map is

usually trained to create its own organization of the training data. The self-organization process occurs into stages whereby in the first phase every neuron value is initialized with a small weight and input vector, while in the second step, the neuron closest to the point is the 'winning neuron' and the neurons connected to it also move towards the point. By repeated iterations, all the points are clustered and each neuron represents each kind of cluster. They are mainly applied in pattern recognition.

- 4. Recurrent Neural Network (RNN)/Long- Short-Term Memory** – This ANN works on the principle of saving the output of a layer and feeding this back to the input to help in predicting the outcome of the layer. In this case, each neuron will remember some information it had in the previous time-step, making each neuron act like a memory cell in performing computations. Therefore, the neural network will work on the front propagation but remember what information it needs for later use. Here, if the prediction is wrong, the learning rate or error correction is used to make small changes so that it will gradually work towards making the right prediction during the back propagation. RNNs are mostly applied in text to speech (TTS) conversion models and auto correct text programs.
- 5. Convolutional Neural Network (ConvNet)** - in this neural network, the input features are taken in batches like a filter which helps the network to remember the images in parts and can compute the operations. ConvNet are applied in signal processing and image classification models. The technique of image analysis and recognition is usually applied when agricultural and weather aspects are extracted from the open source satellites like LSAT to predict the future growth and yield of a given farmland.

**6. Modular Neural Network** – MNNs consist of a combination of different networks working independently and contributing towards the output. Each individual neural network has a set of inputs which are unique compared to other networks in terms of its structure and sub-tasks performed. These networks work independently and as such do not signal each other in accomplishing the tasks. MNNs are applied in many fields of study ranging from biological, psychological, hardware, to computational systems.

#### **2.7.4 ANN Models**

ANN models are specially designed by following certain rules and procedures depending on the problem being addressed. The three standard procedures involve identification of appropriate data consisting of input and output (target) data emanating from rigorous experiments or full-proof numerical models, using these data to train the network (i.e. to compute the connection between the inputs and outputs) and finally testing the workability of the trained network with another set of data to obtain a comparable output to the target (Caner et al., 2011). The most important attribute in ANN modelling is having a thorough understanding of the physical problem. The general procedure involves first identifying the input and output variables for the model (Maier and Dandy, 1997).

Basically, an ANN contains a set layers and nodes that are organized in a certain structure to perform a particular function in a particular manner at a given time. There is a large number of ANNs distinguished from each other in terms of the transfer function used to get the output from the nodes, connection between the nodes of the layers, method of determining the weights between the nodes of different layers, the direction of information flow, and the number of layers (Sinha et al., 2015). Basically,

an ANN consists of three layers i.e. input, hidden and output layer as shown in Figure 2.8 (Caner et al., 2011).

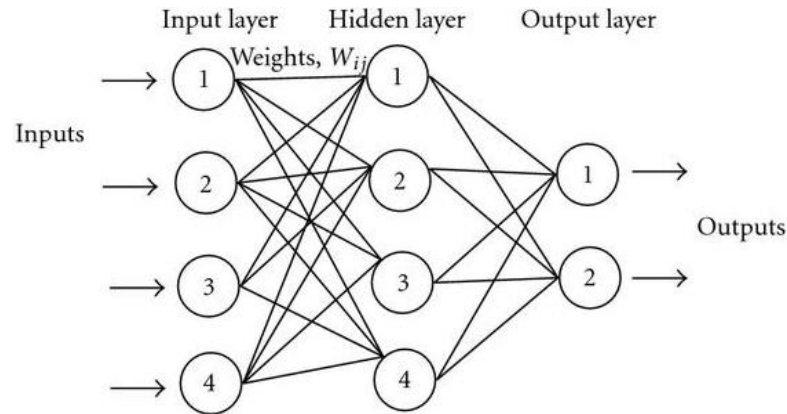


**Figure 2.8: General configuration of a three-layered feed-forward artificial neural network (Caner et al., 2011)**

An ANN consists of a set of processing elements referred to as nodes connecting one layer to another. The number of nodes in input and output layers is a function of the intricacy of the problem at hand though determined from a trial and error process. The relative connection strength between nodes is achieved by assigning a synaptic weight to each link that is used to predict the input-output relationship (Sinha et al., 2015).

The output,  $y_j$  of any node  $j$ , is given as

$$y_j = f\left(\sum_{i=1}^z W_i X_i + b_i\right) \quad (2.12)$$

where,  $z$  is the total number of inputs to node  $j$ ,  $W_i$  is the input connection pathway weight,  $b_i$  is the node threshold,  $X_i$  is the input received at node  $j$  and  $f$  is the transfer function.

Conventionally, a sigmoid transfer function is preferred as it is continuous and differentiable everywhere defined as ASCE, (2000a)

$$f(x) = \frac{1}{1 + e^{-x}}. \quad (2.13)$$

where  $x$  is the input variable. For supervised learning, every input data feed in to the network will be trained comparing with the desired output. In that case, an error will appear together with the desired and the actual output. This error should be minimized and NN should be trained adhering to that. This is the case for most Back-Propagation (BP) algorithms. The error generated when the ANN output is compared with the target output, is given by

$$E(x) = \sum_{\varepsilon} \sum_{\lambda} (y_i - t_i)^2 \quad (2.14)$$

where  $\lambda$  is the number training patterns,  $\varepsilon$  is the number of output nodes,  $y_i$  is the ANN generated output and  $t_i$  the component of the desired output/target  $T$ . The error obtained is then fed back into each thereby updating the weights (ASCE, 2000b).

### 2.7.5 ANN Model Development

As a convention in most ANN models, about 70% of the data is set aside for model training and testing (calibration datasets) while 30% is reserved for model validation. However, it should be noted that fixed requirements regarding the percentage of data to be utilized in each category do not exist. In most geotechnical problems, ANN models are developed by arbitrarily dividing the data into their subsets (Shahin et al, 2004).

Data pre-processing is an important exercise in ANN model development and applications. In this process, the activation function adjusts the output of each neuron to its limiting values. For instance, the data will be scaled and normalized to a range between -1 and 1 for the hyperbolic tangent function and a range of between 0 and 1 for the logistic sigmoid function (Masters, 1993; Stein, 1993).

The most common scaling and normalization is the simple linear mapping method where the variables' extreme to the neural network's practical extreme is adopted

(Masters, 1993; Stein, 1993). In this case, for a variable,  $x$ , with a maximum and minimum values of  $x_{max}$  and  $x_{min}$ , respectively, the scaled value,  $x_n$ , is computed as

$$x_n = \frac{x - x_{min}}{x_{max} - x_{min}} \quad (2.15)$$

Determination of ANN model architecture is carried out after pre-processing and data division. In this step, the number of optimal hidden layers is ascertained through a number of iterations (Maier and Dandy, 1997). During learning or training, the connection weights are optimized. The most frequently used training method is the back-propagation algorithm (Rumelhart et al., 1986; Brown and Harris, 1994).

Cross-validation is performed on the test data set in order to make a decision on when to stop training and avoid overfitting (Stone, 1974). After training, validation of the trained model is done utilizing validation set of data with the aim of evaluating the ability of the model to generalize and establish the input-output relationship.

The prediction performance of the ANN model is usually measured using statistical tests such as the root mean squared error (*RMSE*), the mean absolute error (*MAE*) and the coefficient of correlation ( $r$ ). First, the coefficient of correlation is a standard statistical test used to measure the relative correlation and goodness-of-fit between the predicted and observed data. The correlation coefficient varies from 0 to 1 where  $r = 1$  denotes strong correlation and  $r = 0$  representing the weakest correlation.

Mathematically, the correlation coefficient is computed as

$$r = \frac{C_{y_i d_j}}{\sigma_{y_j} \sigma_{d_j}} \quad (2.16)$$

for which

$$C_{y_j d_j} = \frac{1}{n-1} \sum_{j=1}^n (y_j - \bar{y})(d_j - \bar{d}) = \frac{1}{n-1} \left( \sum_{j=1}^n y_j d_j - \frac{\sum_{j=1}^n y_j \sum_{j=1}^n d_j}{n} \right),$$

$$\sigma_{y_j} = \sqrt{\frac{\sum_{j=1}^n (y_j - \bar{y})^2}{n-1}}, \quad \sigma_{d_j} = \sqrt{\frac{\sum_{j=1}^n (d_j - \bar{d})^2}{n-1}}, \quad \bar{y} = \frac{\sum_{j=1}^n y_j}{n}, \quad \text{and} \quad \bar{d} = \frac{\sum_{j=1}^n d_j}{n},$$

where  $n$  = number of data;  $y_j = y_1, y_2, y_3 \dots y_n$  is the predicted (model) output;  $C_{y_j d_j}$  is the covariance between the model output ( $y_j$ ) and the desired output ( $d_j$ );  $\bar{y}$  the mean of the model output,  $y_j$ ;  $d_j = d_1, d_2, d_3 \dots d_n$  is the desired (observed) output;  $\sigma_{y_j}$  is the standard deviation of the model output,  $y_j$ ;  $\sigma_{d_j}$  is the standard deviation of the desired output,  $d_j$ ;  $y_j$ ; and  $\bar{d}$  the mean of the desired output.

On the other hand, root mean squared error refers to the measure of error computed as (Hecht-Nielsen, 1990)

$$RMSE = \left\{ \frac{1}{n} \sum_{j=1}^n (y_j - d_j)^2 \right\}^{\frac{1}{2}}, \quad (2.17)$$

while MAE is calculated as (Twomey and Smith, 1997)

$$MAE = \frac{1}{n} \sum_{j=1}^n |y_j - d_j| \quad (2.18)$$

### 2.7.6 Application of ANNs in Slope Stability Analysis

ANNs have found application in many disciplines of arts and sciences for regression analysis, prediction and forecasting (Jenkins, 1999). In slope stability studies, ANNs have been employed mostly to predict the health status of embankments and slopes. A number of researchers have strived to apply ANNs with substantial success such as

stability analysis of slopes (Sakellariou and Ferentinou, 2005), digital soil mapping (Behrens et al., 2014), stress- strain modelling of soils (Ellis et al.,1995), assessment of geotechnical properties (Yang and Rosenbaum., 2002), capacity of driven piles in cohesionless soils (Abu Kiefa., 1998), and optimum moisture content in chemically stabilized soils (Alavi et al., 2016).

A research study by Ni et al. (1996) postulated a model which combines fuzzy sets theory with ANNs to assess slope stability. In their approach, several input parameters including maximum daily precipitation and maximum hourly precipitation, height, geological origin, land use, depth of weathering, gradient, direction of slopes, horizontal and vertical profile, location, soil texture and vegetation were used, while the output was being the slope failure potential. This model produced a good agreement with the analytical model.



## CHAPTER THREE

### SLOPE STABILITY MODEL FORMULATION AND EXPERIMENTAL SETUP

#### 3.1 Introduction

Soil mass wasting processes especially debris flows and landslides in sloping locations of the earth's crust have become regular events in the past few decades and as such they form the most significant factors that should be considered during local or territorial management and physical planning. An in-depth study of these disaster risk scenarios will serve the critical purpose of reducing such calamities and by extension lay ground for developing a forecasting and prevention framework. It is therefore pertinent to develop methodologies of data collection using numerical approaches and real-time monitoring system in addition to fabrication of intelligent artificial neural network-based models on the available scenarios in order to implement an early warning system or forecasting platform. To achieve this, a set of electrical, optical and soft computing instruments were selected based on a number of factors including instruments vulnerability, time to install and get results, availability, ruggedness, site accessibility, and weather conditions, to develop a monitoring system.

Experimental tests were carried out at the laboratory level using a hybrid Solar-Powered Monitoring (SPM) system that consists of a combination of both electrical and optical transducers and customized to relay processed information via wireless broadcasting to a remote server. Deriving from the experimentally archived data, an intelligent artificial neural network was developed to learn from the acquired array of datasets and predict the health status of slopes.

In this chapter, an outline of the principal methods of investigation and monitoring techniques are discussed. In summary, the investigation and monitoring methods are

divided into three main groups: numerical model formulation, real-time monitoring technology and fabrication of artificial neural network hierarchy. Details of the equivalent theoretical background for the derivation of numerical models are exposed, theory and working principles of the various transducers and system architecture are discussed and finally the basic structures of the ANN are described. The statistical tools and assumptions used in analysis and optimization in the study are also presented.

### **3.2 Study Area**

Soil samples used in the experiments were excavated from Taptengelei and Kamelil escarpment along the foothills of Tinderet, Nandi County. Geographically, Kamelil area lies within latitude  $0^{\circ} 34'$  North and longitudes  $34^{\circ} 44' - 35^{\circ} 25'$  to the East with an altitude ranging from 1,300 to 3500 m above sea level (Republic of Kenya, 2014). Geological survey of this site reveals that the basement system consists of metamorphosed and sheared volcanic rocks mainly of original basaltic composition belonging to the broader Nyanzian System which consists of mudstones, grits and phyllites of which the principal minerals are montmorillonite, quartz, feldspar, micas and actinolite. The resultant soils are well drained, shallow, dark red to brown, friable sandy clay, rocky, bouldery with acid humic topsoil manifesting as either dystic regosols, lithosols, humic cambisols or rock outcrops (Huddleston, 1951).

The second study area, i.e. Taptengelei ( $35^{\circ}21'00''\text{E}$ ,  $00^{\circ}40'00''\text{E}$ ), is an area known by locals to be very volatile and prone to landslides during prolonged rain seasons. Topographically, there exist elevations ranging from 2000 – 2400 m above sea level with slope gradients in the range of  $0^{\circ} - 58^{\circ}$ . The predominant soil type in this area is kaolinite clay. Most landslides were found to occur along the upper and mid sections

of the valley, where stratigraphy is characterized by a 0.5 - 5 m thick film of colluvial soil overlying the rock mantle (Republic of Kenya, 2014).

### **3.3 Numerical Formulation**

#### **3.3.1: Overview**

The study of land mass deformations and movements whether in sloping regions or dam walls has been done for many years by different researchers using several approaches to try and explain these disastrous spectacles. There exist a number of numerical methods employed for the stability analysis of pure soil, mixed rock-soil or pure rock slopes ranging from the conventional LE methods to the more complex probabilistic approaches (Chen, 2000). Currently, there is access to several methods for slope analysis with varying strengths and limitations. Generally, there are three approaches widely used by engineers and geophysicists worldwide to model landslides and other related soil mass flows (Geist et al., 2009).

The first approach is mostly applied to submerged masses where interactions with water, free surface flows and landslide kinematics are computed using the full Navier-Stokes, Euler or potential flow equations (Løvholt et al., 2015; Geist et al., 2009; Tappin et al., 2008; Watts et al., 2003; Lynett and Liu, 2002). These models are limited in application as they cannot be applied to subaerial slope materials.

In the second approach, also known as longwave model, a time dependent landslide kinematics theorem is computed by taking the slope material as a secondary and coupled fluid film obeying longwave approximations (Cecioni and Bellotti, 2010; Fuhrman and Madsen, 2009; Ataie-Ashtiani and Jilani, 2007). Longwave models are generally complex in terms of computational procedures and limited physics applied;

hence they are usually more applicable in modelling deeply submerged underwater landslides.

The third approach involves a detailed appraisal of either landslide kinematics, deformations and/or both to model full 3D multi-physics/multi-material Euler expression, Navier-Stokes equations or fully nonlinear potential flow equation. These models can be formulated as a one-way coupling e.g. for a rigid body, or computed as a two-way coupling e.g. for solid or deformable slides (Grilli et al., 2010; Abadie et al., 2010; Weiss et al., 2009). Notably, these models are more appropriately applied to subaerial landslides as is considered in this study.

For all the above-mentioned approaches, scientific models are employed to aid in the understanding of these phenomena. A scientific model is a depiction of a physical process in the real world using something else to represent it, for purposes of predicting its characteristics in space and time. There are several types of models ranging from visual to mathematical/numerical and computer models. In addition, visual models represent intangible facts in form of pictures, diagrams, and flowcharts. On the other hand, numerical models use mathematical concepts to describe a particular phenomenon. Generally, Newton's laws and their derived theorems are used to explain and simulate the behaviour of phenomena (<https://study.com/academy/lesson/scientific-models-definition-examples.html>, accessed 11/03/2020).

In this study, four models were proposed to aid in the understanding of soil mass movements. The first two, are physically-based models applied on an idealized spherical-cap-shaped soil mass undergoing translational displacement, the third is an explicit hydro-dynamical numerical model derived from the conventional Mohr-Coulomb postulates to be applied on any given slope, and finally a BP-FF ANN model for landslide prediction.

### **3.3.2 Spherical-cap-shaped slope morphology under planar translational failure**

#### **3.3.2.1 Introduction**

This section is focused on the formulation and implementation of a numerical model applied on a special case of a spherical-cap-shaped soil mass on a convex configuration slope. Soil samples used for validation of this model were extracted from Kamelil escarpment. As alluded to earlier, soil movements occur when preparatory and triggering factors diminish the mobilized shear strength (Rybar et al., 2002). Seismicity, storms and anthropogenic activities are the most common triggers of mass movements (Petley, 2009), as outlined in detail in chapter two.

In this study, soil mass movement processes were studied with a view to develop physical models based on geomorphological (slope gradient, aspect, relative relief), soil characteristics (depth, structure, permeability, porosity), and hydrological factors, which can be employed in the characterization of a wide range of slope sections. For this case, empirical physics-based models are derived from first principles based on inertial forces that build up when a soil mass is inclined at an angle under modest wetting conditions. The objective of the study was to investigate the initiation of translational movement beginning from inertial forces acting on a soil mass, to the build-up of pore-pressures and shear stresses to the effect of these forces on the factor of safety and by extension the displacement downslope.

#### **3.3.2.2 Numerical Model Formulation**

A numerical model was proposed that describes the dynamics of a soil mass inclined at an angle,  $\alpha$ , in a laboratory flume. In this study, a simplified case of a nearly concave-shaped slope section that resembles a spherical cap of relatively small height on a slope of approximately infinite lateral extent as depicted in Figure 3.1 below was

considered. The soil mass was considered as a homogeneous rigid-perfectly plastic material which undergoes shear failure when driving and frictional forces are not balanced. The volume in consideration is illustrated by the portion  $abcd$  which is approximated to a spherical cap of height  $H \cos \alpha$  and base length  $L$ . From the definition of the volume of a spherical cap, the weight of a dry soil skeleton is derived as

$$W_d = \frac{\pi \gamma_d H \cos \alpha}{6} \left( \frac{3L^2}{4} + H^2 \cos^2 \alpha \right) \quad (3.1)$$

where  $\gamma_d$  is the dry unit weight of the soil defined by

$$\gamma_d = \frac{G \gamma_w}{1 + e} \quad (3.2)$$

with  $G$ , the specific gravity of soil; and  $e$ , the void ratio.

When the soil mass is exposed to wetting conditions usually through a rainfall simulator or irrigation event (introduction of water into the soil crystal matrix), the new weight of the saturated soil segment assuming there is negligible run-off is

$$W_s = \frac{\pi \gamma_e H \cos \alpha}{6} \left( \frac{3L^2}{4} + H^2 \cos^2 \alpha \right) \quad (3.3)$$

where  $\gamma_e$  is the effective unit weight of the soil defined by De Vleeschauwer and De Smedt (2002) as

$$\gamma_e = \frac{q \cos \alpha}{H} + (1 - m) \gamma_d + m \gamma_s \quad (3.4)$$

for which  $q$  is the additional weight on the soil surface by vegetation or structures.

The factor  $m$  in equation (3.4) above is the wetness index defined by Ray et al. (2010) as

$$m = \frac{h + (H - h)S}{H} = \frac{h + (H - h) \left( \frac{\theta}{n} \right)}{H} \quad (3.5)$$

where  $h$  is the saturated thickness of the soil above the failure plane and  $S = \theta/n$  is the degree of saturation;  $n$  is the soil porosity and  $\theta$  is the volumetric moisture content derived from the modified soil-water characteristic curve proposed by Fredlund and Xing (1994) as

$$\theta = \left[ 1 - \frac{\ln\left(1 + \frac{\psi}{\psi_r}\right)}{\ln\left(1 + \frac{10^6}{\psi_r}\right)} \right] \left[ \frac{\theta_s}{\ln\left(e_n + \frac{\psi}{\beta}\right)^{\zeta}} \right] \quad (3.6)$$

where  $\theta_s$  is the saturated volumetric water content,  $\psi$  is the soil suction,  $\psi_r$  is the residual soil suction,  $e_n$  is a natural number while  $\beta$ ,  $\varsigma$ ,  $\zeta$ , are curve fitting parameters with  $\beta$  carrying the units of pressure.

The mathematical model for the effective unit weight of the soil (equation 3.4) as proposed by De Vleeschauwer and De Smedt (2002) is valid with its assumption that water pressures in the wet pores are transmitted to the failure plane through the interconnected wet soil pores. In contrast, we propose that for more precise results, the unsaturated zone soil moisture content must be accounted for in the computation of the wetness index and the effective unit weight as opposed to earlier studies where effective unit weight of the soil was either considered for purely saturated conditions or on purely dry soil skeleton. Based on earlier studies by Sidle and Ochiai (2006), we propose substitution of the dry unit weight with the moist unit weight ( $\gamma_m$ ) in equation (3.4) resulting in

$$\gamma_{em} = \frac{q \cos \alpha}{H} + (1-m)\gamma_m + m\gamma_s \quad (3.7)$$

where

$$\gamma_m = G\gamma_w(1-n)(1+\theta) \quad (3.8)$$

is the moist unit weight of the soil, and  $\gamma_w$  is the unit weight of water.

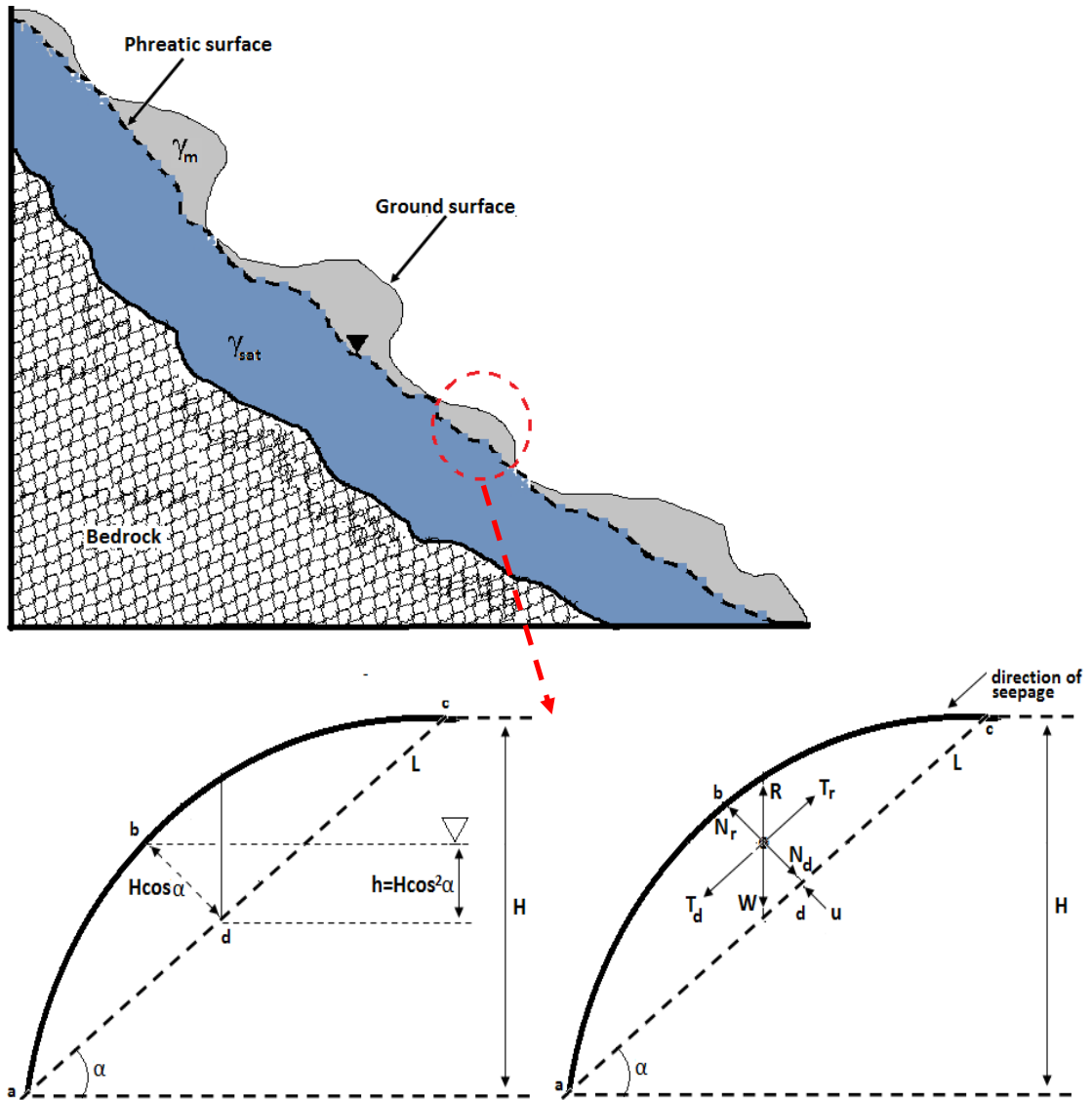


**Figure 3.1: Schematic illustration of a spherical-cap-shaped slope section (shaded) and an extract of the inertial forces acting on it**

Therefore the total weight of the moist but unsaturated soil ( $W_{moist}$ ) will now be obtained by utilizing equation (3.7) as

$$W_{moist} = \frac{\pi \gamma_{em} H \cos \alpha}{6} \left( \frac{3L^2}{4} + H^2 \cos^2 \alpha \right). \quad (3.9)$$

Consequently, the effective normal and shear stresses for moist soil mass respectively are derived (considering the base area =  $\pi L^2/4$ ) as



$$\sigma_n = \frac{2\gamma_{em} H \cos^2 \alpha}{3} \left( \frac{3}{4} + \frac{H^2}{L^2} \cos^2 \alpha \right) \quad (3.10)$$

$$\text{and } \tau_d = \frac{2\gamma_{em} H \cos \alpha \sin \alpha}{3} \left( \frac{3}{4} + \frac{H^2}{L^2} \cos^2 \alpha \right) \quad (3.11)$$

The empirical model for precipitation representing a single rainfall event over a period of time is derived from an odd Fourier Series expression as

$$Rn(t) = \frac{k}{\eta} \sum_{\eta=1}^{\infty} \frac{\sin(2\eta-1)t}{(2\eta-1)} \quad (3.12)$$

where  $k$  and  $\eta$  are curve fitting parameters, determined from experimental validations. Conventionally, unsaturated soil hydraulic properties are evaluated from water retention characteristic curves. These curves are used to give the relationship between water content ( $\theta$ ) and water (matric) potential ( $h$ ) in the soil. van Genuchten (1980) proposed a mathematical model that has been used in describing water retention curves as

$$S = \frac{\theta - \theta_r}{\theta_s - \theta_r} = \frac{1}{\left(1 + |\mathfrak{I}h|^n\right)^{\frac{1}{n}}} \quad (3.13)$$

where  $S$  is the effective water content,  $\theta$  is the volumetric moisture content, while  $\theta_s$  and  $\theta_r$  are saturated and residual water contents respectively,  $h$  is the soil matrix potential,  $\mathfrak{I}$  is related to the inverse of the air entry suction, and  $n$  is a measure of the pore-size distribution. Therefore, as infiltration proceeds, the pore-water pressure in the soil mass at point  $h$  with respect to the phreatic surface is given by

$$u = \gamma_w h = \gamma_w H \cos^2 \alpha. \quad (3.14)$$

An empirical equation relating the apparent soil cohesive stress and volumetric water content is proposed taking the form,

$$c' = \varpi \theta^{-1} e^{-\frac{g}{\theta}}, \quad (3.15)$$

where  $\varpi$  is the coefficient of cohesive stress which is a function of porosity, surface tension and matric suction within the soil grains, while  $\mathcal{G}$  is a curve fitting parameter.

Assuming that there is minimal seepage through the soil mass in consideration and that the groundwater level in this segment is parallel to the incline plane, then the shear stress of the soil with effective cohesion  $c'$  and effective angle of shear resistance  $\phi'$ , is given by (Bishop, 1967):

$$\tau_r = c' + (\sigma - u) \tan \phi'$$

$$\text{or } \tau_r = c' + \left[ \frac{2\gamma_{em}H \cos^2 \alpha}{3} \left( \frac{3}{4} + \frac{H^2}{L^2} \cos^2 \alpha \right) - \gamma_w H \cos^2 \alpha \right] \tan \phi' \quad (3.16)$$

Assuming that slope stability is characterized by the Mohr-Coulomb failure criterion and that there are no external loads, the factor of safety will then be computed as

$$FS = \frac{2c' \csc 2\alpha}{\square \gamma_{em} H} + \left( 1 - \frac{1}{\square} \frac{\gamma_w}{\gamma_{em}} \right) \frac{\tan \phi'}{\tan \alpha} \quad (3.17)$$

$$\text{where } \square = \frac{2}{3} \left( \frac{3}{4} + \frac{h^2}{L^2} \cos^2 \alpha \right).$$

The time-independent displacement component of the soil mass downslope which is a function of the  $FS$ , slope and internal friction angle has been modelled by the relation

$$S = \frac{1}{2} g \Upsilon \langle t \rangle^2 (1 - FS) [\sin \alpha - \cos \alpha \tan \phi], \quad (3.18)$$

where  $\Upsilon$  is a curve fitting parameter.

### 3.3.2.3 Experimental setup and design

A solar-powered monitoring (SPM) system was fabricated comprising of a model flume (hereinafter referred to as the 'Chep-flume') installed with both electronic and optical displacement sensors connected to a data acquisition panel and a rainfall simulator system. The dimensions of the Chep-flume were 1.6m long, 0.6m width and

0.5m high (figure 3.2 - schematic diagram and picture). The flume framework was made from steel angle bars while the sides were made from sheets of plywood sheets. The base was made of thick iron sheeting material covered on the upper part by a layer of rough concrete. The inclination/slope angle of the flume was achieved by the use of a hydraulic jack that could lift or lower the rear side.

A rainfall simulation system consisting of a water source, sprinkler set and flow rate controller was designed. The sprinkler system was composed of an array of equally spaced nozzles placed 2 m above the flume. It was mounted on the system in such a way that the flow rate could be controlled remotely via an electronic switch. Monitoring of the incident rainfall was realized via a rain gauge which was wirelessly connected to a Steven's™ Vantage Console for onward transmission of data to a remote computer.

Several transducers and sensors were connected to the system for purposes of monitoring physical parameters including pore-water pressure, volumetric water content and translational displacement. Two moisture probes, two vibrating wire piezometers and one set of ultrasonic sensors were installed on the system at different points. Pore-water pressure in the soil mass was measured by means of a vibrating wire piezometer connected to a 4–20-mA data logger. Soil moisture content and displacement were monitored using Arduino-based resistivity and ultrasonic transducers, respectively. Arduino-based sensors were connected to a microprocessor for interface with a PC. A flowchart of data from the array of transducers to the data loggers connected to the remote server is shown in figure 3.3.

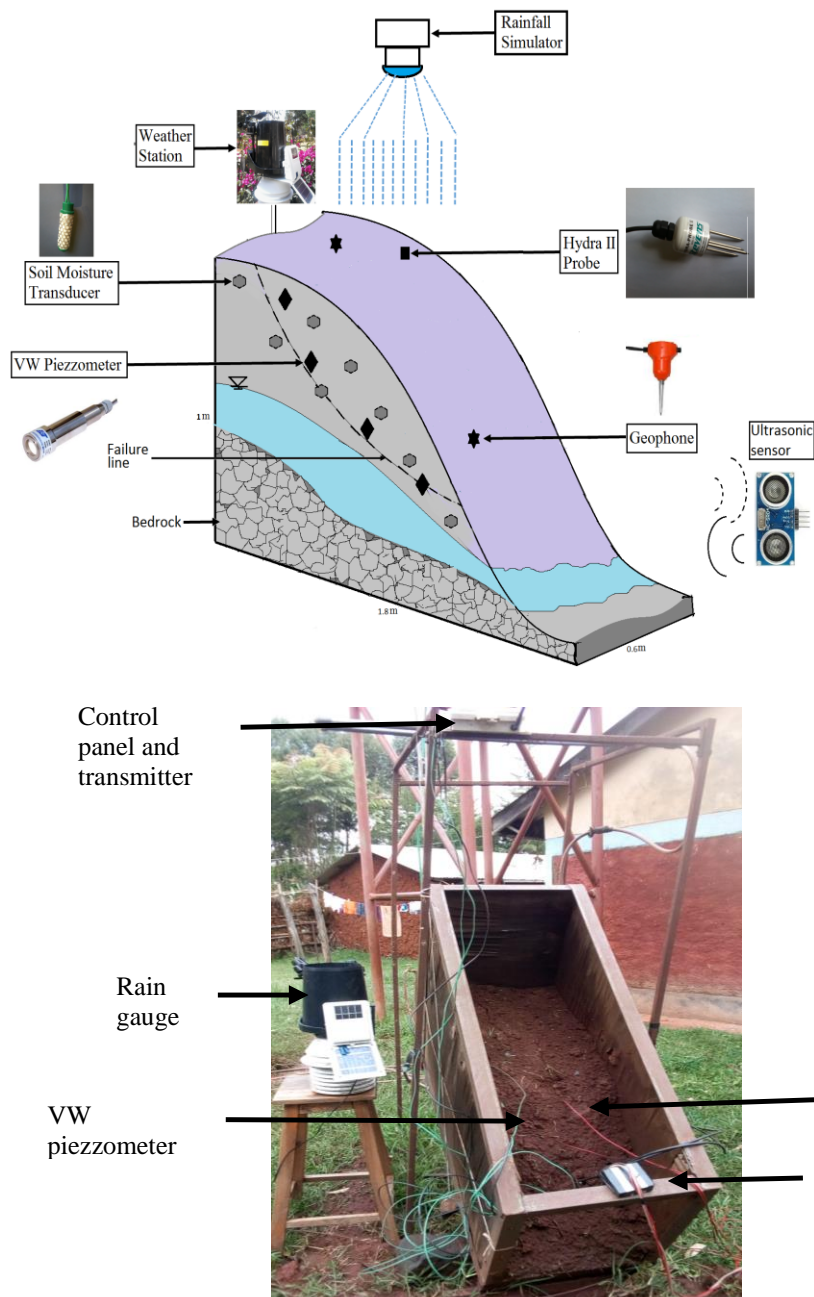


**Figure 3.2: SPM system setup (schematic diagram and picture) (Source: Author, 2020)**

Four experiments were carried out with a rainfall simulator, while one control system was set up with no rainfall applied to it. For each soil sample collected, approximately 80% of it ( $\approx 120$  kg) was placed in the model flume to form a single flat layer and then the remaining 30 kg was poured at the centre to form the spherical-cap-shaped mass. No compaction of the soil was conducted. One side of the flume was then tilted at an

angle of  $58^\circ$  to the horizontal using a high-lift jack. Failure of the soil mass was facilitated by the use of an artificial rainfall from the simulator. The spherical-cap-shaped model of the slope was chosen from the fact that, for a given slope of relatively high gradient with negligible vegetation cover, due to uneven erosion incidences, moderate bump-shaped soil masses are left behind which resemble spherical caps of finite length along the incline plane.

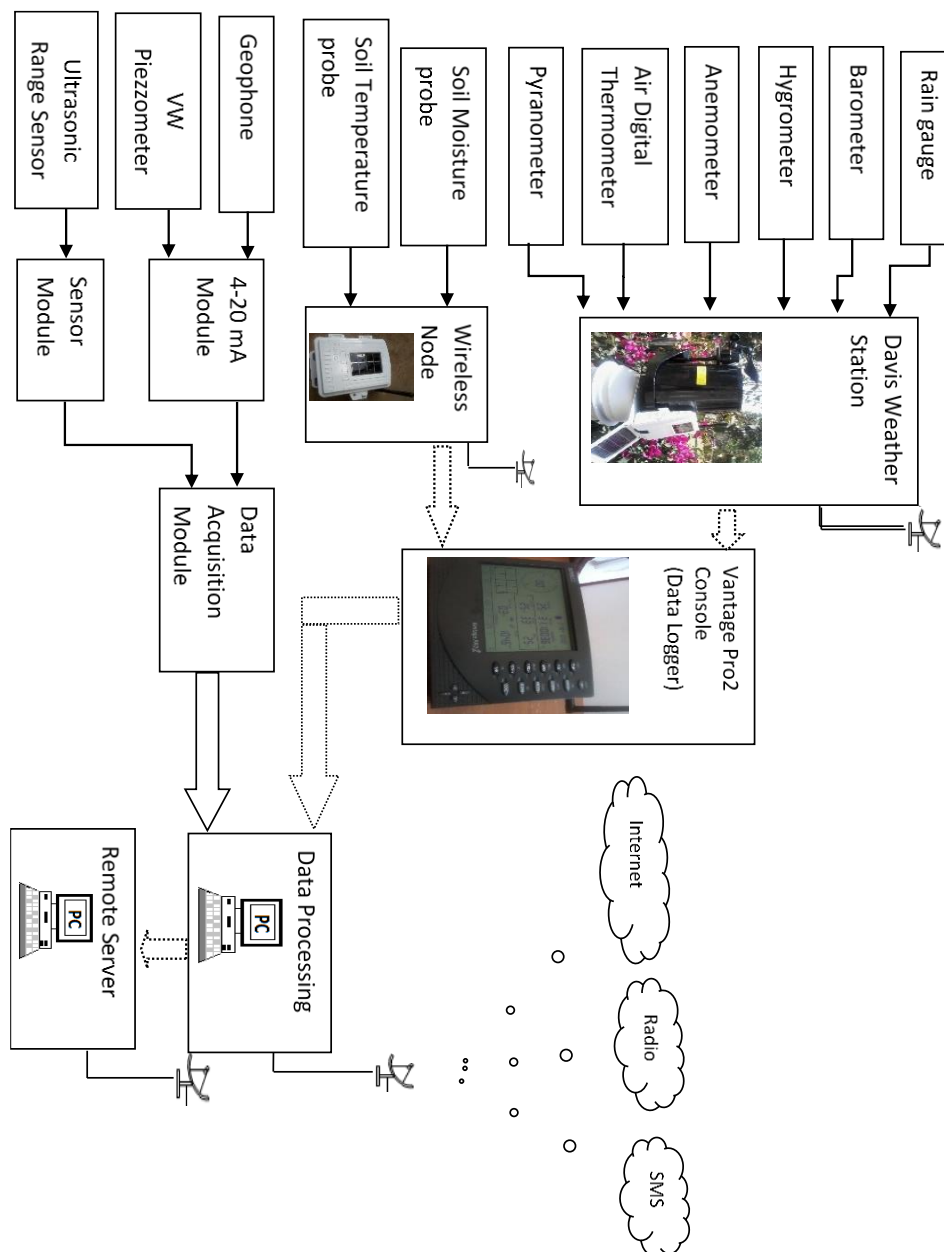


**Figure 3.3: SPM flowchart**

### **3.3.3 Double-Spherical-Cap-Shaped Slope Morphology Under Planar**

#### **Translational Failure**

##### **3.3.3.1 Introduction**

Along most slopes of relatively high gradient, the terrain is never uniform but rather composed of majorly hill-like or more precisely, spherical-cap shaped soil masses of height less than 5 m. In this study, we consider a model of a slope section composed of a homogeneous rigid-perfectly plastic material having a nearly double spherical-cap-shaped morphology defined on the lower side by a concave-shaped failure surface as illustrated in Figure 3.4 below.

The pertinent assumption in this model is that failure must be preceded by crack formation at the head-side of the landmass while the toe must be saturated hence eroded. Cracks are usually caused by differential settling, drying and shrinking of soil, as well as associated construction activities. For unsaturated conditions, the crack must be deep enough to make a connection with the ground water table or perched phreatic surface.

During a rainfall storm, three scenarios are likely to manifest. Primarily, overland waterflow will fill the crack thus pushing the soil mass laterally and also increasing negative pore-water pressure for the region just above the ground water table resulting into formation of a failure plane, which is concave-shaped because of preferential gravitation water flow defining the phreatic surface. Furthermore, infiltration of rain water into the soil mass will act to increase its weight and by extension the gravitational driving force downslope. Finally, for shrinking and swelling soils, infiltration of rain water will lead to swelling especially for regions above the phreatic surface thus pushing it downwards.

At any given time, when driving forces exceed the shear strength of the soil mass, failure can occur in many ways but in general two forms are dominant. First, when the soil mass becomes saturated, considering seepage force and steady infiltration at the same time, it will undergo liquefaction and therefore flow like a non-Newtonian fluid along the failure plane; and secondly, the unsaturated soil mass will undergo translational failure (even when the failure plane is nearly circular) downslope along the failure plane (in this case seepage force is ignored) as long as the failure line is composed of saturated granules thus acting as a lubricating surface.

### 3.3.3.2 Numerical Model Formulation

In this study, a derivation of kinematic and constitutive equations was conducted relating the inertial forces acting on a slope material (a soil mass) and the factor of safety at different slope angles for a given set of hydrological conditions. For mathematical convenience, we consider a simplified case of a soil mass resembling a spherical cap on a slope of height  $H \cos \alpha$  (measured from a line defining the incline plane) but with infinite lateral extent. It is assumed that after failure, the vacancy/hole left when the soil mass undergoes translation downslope or is liquified, resembles a mirror image of the upper spherical cap thereby leading to the conclusion that the total volume of soil failed is equivalent to two spherical caps sharing a common base (double spherical-cap-shape) as illustrated in figure 3.4.

The volume in consideration is illustrated by the portion *abcdefg* (figure 3.4) which is approximated to double spherical caps of base length  $L$ . From the trigonometric relations involving spherical caps, the weight of the double cap for moist soil (computed through geometry of the slope) will therefore be given by

$$W_{moist} = \frac{\pi \gamma_e H \cos \alpha}{12} (3L^2 + H^2 \cos^2 \alpha) \quad (3.19)$$

where  $\alpha$  is the slope angle and  $\gamma_e$  is the modified effective unit weight of the moist soil.

In this consideration, it is assumed that all the incident rainfall infiltrates into the soil mass neglecting surface runoff and/or evaporation. It is further assumed that surface runoff can only occur when the soil mass in consideration is fully saturated i.e. precipitation rate is less than equilibrium infiltration capacity. As the soil mass is subjected to moderate infiltration rate, the volumetric water content continues to increase thereby necessitating a corresponding change in pore-water pressure defined by

$$u = \gamma_w h = \gamma_w H \cos^2 \alpha, \quad (3.20)$$

where  $\gamma_w$  is the unit weight of water.

Considering the base area of a spherical cap as,  $A_{curve} = \frac{\pi}{4} (L^2 + H^2 \cos^2 \alpha)$ , the effective normal ( $\sigma_n$ ) and shear stresses ( $\tau_d$ ) for this moist soil mass respectively is then computed as

$$\sigma_n = \gamma_e \zeta H \cos^2 \alpha \quad (3.21)$$

$$\text{and } \tau_d = \gamma_e \zeta H \cos \alpha \sin \alpha \quad (3.22)$$

$$\text{where } \zeta = \frac{1}{12} \left( \frac{3L^2 + H^2 \cos^2 \alpha}{L^2 + H^2 \cos^2 \alpha} \right)$$



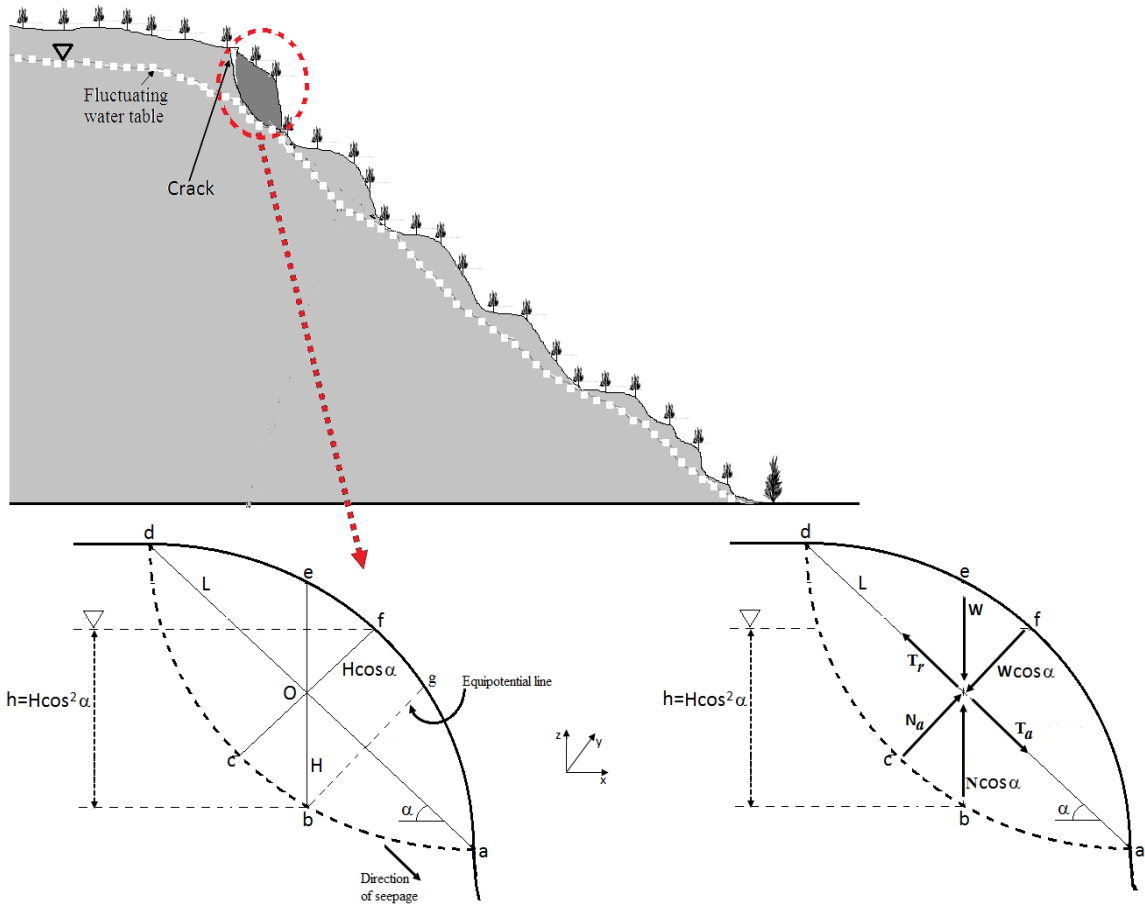


**Figure 3.4:** A section of a concave shaped rigid-perfectly plastic soil mass on a slope with an exploded view of the shaded part of the slope indicating Inertial forces acting on the soil mass.

Considering that the groundwater level coincides with the failure plane, then the shear strength of the soil with effective cohesion,  $c'$ , and effective internal angle of friction,  $\phi'$ , is given by (Bishop, 1967):

$$\tau_r = c' + (\sigma - u) \tan \phi'$$

or re-arranging to make use of equations (3.20) and (3.21), to obtain,

$$\tau_r = c' + [\gamma_e \zeta H \cos^2 \alpha - H \cos^2 \alpha] \gamma_w \tan \phi',$$

$$\text{or } \tau_r = c' + [\zeta \gamma_e - \gamma_w] H \cos^2 \alpha \tan \phi'. \quad (3.23)$$

Bearing in mind that slope stability is controlled by the Mohr-Coulomb failure criterion void of external stresses, then the factor of safety is therefore derived as

$$FS = \frac{c'}{\gamma_e \zeta H \cos \alpha \sin \alpha} + \left(1 - \frac{\gamma_w}{\gamma_e} \frac{1}{\zeta}\right) \frac{\tan \phi'}{\tan \alpha}. \quad (3.24)$$

The time-dependent displacement of the soil mass downslope which is also a function of the crack depth, factor of safety, slope angle and internal friction angle will take the form of equation (3.18).

### 3.3.3.3 Experimental setup, design and assumptions

The samples used in the experiment are friable sandy clay soils excavated from Taptengelei escarpment (35°21'00"E, 00°40'00"E) averagely composed of 50% sand, 18% silt and 32% clay (Gachene and Kimaru, 2003). Validation experiments were done using the SPM system as described in section 3.3.1.3 above. A set of sensors including two moisture probes, two vibrating wire piezometers and one set of ultrasonic sensors were installed in the flume. A stand-alone wireless rain gauge was positioned next to the flume. All the sensors were attached to the SPM system for data acquisition.

A total of five soil samples were collected from the study site, four of which were exposed to the rainfall simulation process while one was used as a control experiment for comparative study. Each of the uncompacted and unconsolidated soil samples were placed in the flume carefully so as to minimize structural disturbance. The setup was prepared in such a way that only water from the rainfall simulator was allowed to infiltrate into the soil sample so that the volumetric water content measured was confined to infiltration only. Each soil sample was placed in the flume and exposed to constant rainfall intensity and duration. Rainfall simulation tests were performed on each soil sample at different angles ranging from 30°–70° for a period of about 45 minutes. An embedded flow rate control device was fitted to a simple shower system to simulate rainfall at an intensity of approximately 45 mm/hr. For each slope angle,

parametric data of water content, pore pressure and displacement were collected under these constant rainfall conditions until mass failure occurred (Orense et al., 2004).

These experiments were anchored on three major assumptions. First, it is assumed that all the incident rainfall water should infiltrate into the soil with no runoff or radial seepage. Secondly, the variation of the mean values of VWC and PWP with time remained unchanged for all the experiments. Finally, it was assumed that the soil mass will become nearly saturated after 45 minutes when a rainfall intensity of 45 mm hr<sup>-1</sup> is maintained.

### **3.3.4 Hydromechanical Landslide Model**

#### **3.3.4.1 Introduction**

Slope failures which have had disastrous impacts to human life and the environment in general have been linked to many factors including lithological properties, soil behaviour, slope geometry, hydraulic conductivity, rainfall intensity and duration, surface cracks and percentage of vegetative cover (Chen and Zhang, 2014). Slope stability analyses especially those based on flume-based experiments identified grain size, sand content, shear strain and maximum pore pressure as the triggering factors (Olivares and Damiano, 2007).

Earlier research reports had also indicated a strong dependence of soil shear strength on the amount of soil moisture present (Muntohar and Liao, 2009; Rahardjo et al., 2007). In essence, the most dominant factors that have been pinpointed to modify the stability status of slopes in unsaturated soils are hydrological in nature with rainfall intensity and duration emerging conspicuously as the key parameter (Zhao and Zhang, 2014; Ray et al., 2010).

Over the years, researchers have employed several models in varied forms and scenarios to analyze hydrologically influenced landslide processes and mechanisms. The two dominant approaches utilized in most scientific studies are physically-based and statistical models. Statistical models are based on relations and assumptions between triggering factors and the probability of occurrence of slope failure, while physically-based models employ the relationship between soil water content and predisposing aspects to analyze landslide phenomena (Wu et al., 2015; Springman et al., 2013). Because of the spatial-temporal variability of landslide processes, physically based models are preferred over statistical ones.

In this study, a hydro-dynamical empirical equation has been derived that falls under the broader category of physically-based models, to describe rainfall induced landslide phenomena. This model as derived from first principles, outlines the effect of VWC derived from rainfall events, on the slope parameters ranging from the resultant inertial forces to slope failure due to shear stress. The model was then validated by experimental tests on a laboratory flume. The ultimate goal in this research study was twofold: firstly, is to derive and validate a mathematical expression that describes the dependence of the factor of safety (FS) and eventual slope failure on the VWC, and secondly, to ascertain the minimum value of the VWC that can cause slope stability for purposes of developing an early warning system.

#### **3.3.4.2 Numerical Model Formulation**

Physical processes are usually described by mathematical models in form of equations for purposes of enhancing the understanding of the scientific facts associated with them. In this study, we considered a soil mass located on a slope of infinite lateral extent inclined at an angle  $\alpha$  as a homogeneous rigid-perfectly plastic material (as

shown in figure 3.4) held in position by basal friction due to cohesive forces between soil grains and/or internal friction along a linear failure plane as our base prototype. From theorems of mechanics, the downward component of the gravitational force along the incline plane for moist soil will take the form,

$$F_d = m_T g \sin \alpha = G_s \gamma_w (1-n)(1+\theta) V \sin \alpha \quad (3.25)$$

where  $\gamma_w$  is the unit weight of water,  $n$  is the porosity,  $V$  is the total volume of the soil,  $m_T = m_s + m_w$  is the total mass of the moist soil, and  $\theta$  is the volumetric moisture content.

The resultant resistive force considering the friction component at the base of the soil mass with the coefficient of dynamic friction,  $\mu = \tan \phi$ , is given by

$$F_r = G_s \gamma_w (1-n)(1+\theta) g V \cos \alpha \tan \phi, \quad (3.26)$$

with  $\phi$  as the soil internal angle of friction.

For cohesionless soils such as coarse sand, Newton's second law of motion will yield

$$ma = G_s \gamma_w (1-n)(1+\theta) g V \sin \alpha - G_s \gamma_w (1-n)(1+\theta) g V \cos \alpha \tan \phi,$$

$$\text{or} \quad a = g (\sin \alpha - \cos \alpha \tan \phi). \quad (3.27)$$

Askarinejad et al. (2012) formulated a simplified equation of defining apparent cohesion as a soil property dependent on the degree of saturation ( $S_r = \theta/n$ ), matric suction ( $u_a - u_w$ ) and internal friction angle ( $\phi$ ), mathematically expressed as,

$$C = S_r (u_a - u_w) \tan \phi. \quad (3.28)$$

Therefore, the cohesive force component in three degrees of freedom is derived from equation (3.28) as,

$$F_c = \frac{3}{2} A S_r (u_a - u_w) \cos \alpha \tan \phi, \quad (3.29)$$

where  $A$  is the cross-sectional area of the base along the plane.

Consequently, by taking into consideration equation (3.29), Newton's second law of motion law for cohesive soils will therefore be derived as

$$ma = G_s \gamma_w (1-n)(1+\theta) V \sin \alpha - G_s \gamma_w (1-n)(1+\theta) V \cos \alpha \tan \phi - \frac{3}{2} AS_r (u_a - u_w) \tan \phi$$

or 
$$a = g(\sin \alpha - \cos \alpha \tan \phi) - \frac{3}{2} \left( \frac{1}{HG_s \gamma_w} \right) \left( \frac{1}{n(1-n)} \right) \left( \frac{1}{\frac{1}{\theta} + 1} \right) (u_a - u_w) \tan \phi \quad (3.30)$$

Equation (3.30) defines the tangential acceleration as a function of the slope angle, internal friction angle, slope height, pore water pressure and water content, as opposed to earlier models which incorporated many other parameters such as cohesive stress.

Computationally, the factor of safety is defined as the ratio of resistive to driving forces for a given soil mass on a sloping plane. For the two scenarios i.e. for cohesionless and cohesive soil models, the factors of safety respectively are expressed as

$$FS_{cohesionless} = \frac{F_{resistive}}{F_{driving}} = \frac{\tan \phi}{\tan \alpha} \quad (3.31)$$

and

$$FS_{cohesive} = \left[ 1 - \frac{3}{2} \left( \frac{1}{HG_s \gamma_w} \right) \left( \frac{1}{n(1-n)} \right) \left( \frac{1}{\frac{1}{\theta} + 1} \right) (u_a - u_w) \right] \frac{\tan \phi}{\tan \alpha} \quad (3.32)$$

While equation (3.31) is a standard expression for the factor of safety for many non-cohesive soils, as conventionally derived by geotechnical engineers, equation (3.32) as derived in our study, differs substantially from conventional constitutive equations. In equation (3.32), the FS in the model is expressed as a function of the slope height and angle, porosity, internal friction angle, matric suction and VWC. This equation is simplified in the sense that once the slope height and angle of a soil mass are

ascertained, slope stability measurements will only require two sets of sensors (i.e. PWP and VWC transducers) as opposed to conventional models requiring monitoring of very many parameters. More precisely, measurement of soil cohesion is usually tedious and relatively expensive as it requires a triaxial machine. In this model, the cohesion term is simplified by expressing it in terms of the degree of saturation (and by extension VWC) and PWP, making it comparatively easier to monitor.

According to studies by Vanapalli and Fredlund (2000), it is desirable to use the normalized water content in the calculation of factor of safety which was derived by van Genuchten (1980) as

$$\Theta = \frac{\theta - \theta_r}{\theta_s - \theta_r} \quad (3.33)$$

where  $\theta$  is the water content,  $\theta_r$  and  $\theta_s$  are the residual and saturated water contents respectively.

The equation for the factor of safety (3.32) describes the dependence of FS on normalized VWC only when other lithological factors of the soil mass are known. This is a remedy to geotechnical engineers and scientists who have employed so many sensors to measure several parameters that affect the FS. This therefore is a cost-effective and relatively easier method of computing the FS.

Finally, at the critical safety factor, i.e. FS = 1, the corresponding value of the critical water content after algebraic rearrangement of equation 3.32 yields

$$\Theta = \frac{3}{2} \left( \frac{\lambda}{HG_s \gamma_w} \right) \left( \frac{1}{n(1-n)} \right) \frac{\tan \phi}{\tan \alpha} - 1 \quad (3.34)$$

where  $\lambda$  is a dimensionless curve fitting parameter.

This is the threshold VWC necessary for a slope to fail. The threshold VWC is vital when designing an early warning system or disaster mitigation control centre. When the FS is equal or less than unity, there is high probability of shear failure. This

process can be quantified by monitoring local displacement of certain sections of the slope. The proposed empirical equation for displacement is derived from kinematic equations of motion i.e.

$$S = \xi \langle t \rangle^2 \left[ g (\sin \alpha - \cos \alpha \tan \phi) - \frac{3}{2} \left( \frac{1}{HG_s \gamma_w} \right) \left( \frac{1}{n(1-n)} \right) \left( \frac{1}{\theta + 1} \right) (u_a - u_w) \tan \phi \right],$$

(3.35)

where  $\xi$  is a curve fitting parameter and  $t$  is the time duration. Again, in this regard, the time-dependent displacement has been expressed in terms of only three measurable parameters i.e. PWP, VWC and time. This therefore means that we can ascertain the time of onset of failure by making  $t$  subject of the formula in equation 3.35. Experimentally, measured data of VWC, PWP and displacement can be computed in the equation to obtain the critical time for onset of slope displacement.

### 3.3.4.3 Experimental setup, design and assumptions

The soils used in the experiment were of igneous origin which belong to ferralic cambisols classification excavated from Kamelil escarpment (34° 44' - 35° 25'). Averagely, they are composed of 60% sand, 16% silt and 24% clay with a pH of 4.5–5.0 (Gachene and Kimaru, 2003).

An SPM system described in section 3.3.1.3 above was used for validation experiments. As alluded to earlier, the SPM system is composed of the flume, rainfall simulator, and embedded sensing elements including one wireless rain gauge, two moisture probes, two vibrating wire piezometers and one set of ultrasonic sensors. Data from all the sensors was captured via a control panel which could relay them wirelessly to a remote pc as depicted in the flowchart (figure 3.3).



A series of six experiments were setup to evaluate the performance of the derived hydromechanical model on a soil mass at different inclination angles ( $30^\circ - 70^\circ$ ) in terms of the factor of safety (FS) and shear displacement. Since FS is a dependent variable i.e. a function of slope angle, pore-water pressure, internal friction angle and cohesive stress, which are also controlled by the VWC, it is computed from data obtained for each of these parameters based on the derived equation.

### **3.4 ANN model**

#### **3.4.1 Introduction**

ANNs possess very vital features which make them valuable and attractive for classification and forecasting processes. Most importantly, they are data driven self-adaptive models which can learn from examples and identify unknown linear/nonlinear relationships among the input and output data. In this section, an ANN model, more specifically a multilayer perceptron (MLP) network trained with a back-propagation algorithm, is developed to estimate the Factor of Safety (FS) of an artificial slope confined in a laboratory flume. Soil sample parameters including apparent cohesion, slope angle, pore-water pressure and volumetric moisture content (which form the input layer) were varied during the experiment while computing the corresponding FS (output layer) using the hydro-dynamical landslide model discussed in section 3.3.4. Results obtained were used to develop the ANN model whose results were compared with the numerical results from the hydro-dynamical model.

#### **3.4.2 ANN model formulation**

Multilayer perceptron (MLP) networks are the most commonly used category of ANNs in the study of geotechnical processes. The architectural structure of MLPs is

normally feed-forward though they are trained with a back propagation (BP) algorithm. MLPs usually consist of an input layer, one or more hidden layer(s) and an output layer (Rumelhart et al., 1986). The most general procedure of developing an ANN model for a given task involves a number of basic steps namely identification of the inputs and output(s), pre-processing and division of data, pinpointing the appropriate network architecture, determination and optimization of the synaptic weights (training), setting up of the stopping criteria and model validation (Caner et al., 2011; Shahin et al., 2002).

From experimental studies, five parameters were identified to have a significant impact on the stability of a cohesive slope. These parameters which include slope angle ( $\alpha$ ), internal friction angle ( $\phi$ ), cohesive stress ( $C$ ), volumetric water content (VWP) and pore-water pressure (PWP) are treated as the inputs to the ANN model while the factor of safety (FS) is taken as the desired output. A cross-validation procedure is used as the stopping criterion in calibrating the ANN so as to avoid overfitting (Stone, 1974).

During ANN model development, data was divided into three sets i.e. 247 data points were set aside for training, 50 for testing and 59 for validation, in line with the ANN modelling rules for a given statistical population (Shahin et al., 2004; Masters, 1993). The calibration data was further pre-processed by scaling or normalization to give a transformation bounded in the range of -1 to +1 with the aid of equation (3.36)

$$X_n = \frac{X_{value} - X_{mean}}{X_{max} - X_{min}}, \quad (3.36)$$

where  $X_n$  is the normalized dataset;  $X_{value}$  is the original/experimental value in the dataset;  $X_{min}$  and  $X_{max}$  is the minimum and maximum value of dataset respectively.

When data division and pre-processing was complete, the ANN model was trained by repeatedly presenting a series of input and output pattern sets to the network for it to learn from and establish a connection relationship. The network gradually learns the input/output relationship by adjusting the synaptic weights to attain minimal error between the target and predicted output from the training sample. Furthermore, cross-validation is utilized as the stopping criterion in order to eliminate overfitting. Validation data sets were then used to evaluate the precision of the ANN model developed.

The network architecture and parameter settings determine the performance rating of the developed ANN model. Usually, a trial-and-error method is used to determine the network architecture but in general, the universal approximation theorem proposes that a network with one hidden layer is capable of approximating any nonlinear or continuous function MLP (Cybenko, 1989). Generally, the transfer function, epochs, learning rate, number of hidden nodes and layers, determines the ANN model design (Mollahasani et al., 2011).

In this study, the *tanh* and *sigmoid* transfer functions were used in the hidden and output layers respectively, while learning rate and momentum were determined by the software program. The software program also generated reports of the mean absolute error (*MAE*), root mean squared error (*RMSE*) and correlation coefficient (*r*) values for each model. As a result, the network with the optimum *R*, lowest *RMSE* and *MAPE* values on the training data sets was selected as the optimal model.

By definition, *RMSE* is the measure of the difference between values predicted by a model and the actual experimental values defined mathematically as

$$RMSE = \sqrt{\frac{\sum_{i=1}^j (X_{obs,i} - X_{model,i})^2}{j}} \quad (3.37)$$

where  $X_{obs}$  and  $X_{model}$  are observed and modelled values at time/place  $i$  respectively, while  $j$  is the number of data points (Nahm, 2016).

On the other hand, the correlation coefficient indicates the strength and direction of a linear relationship between model output and experimental values. For a series with  $i$  observations and  $j$  model values, the correlation coefficient is used to estimate the correlation between the model and observations as

$$r = \frac{\sum_{i=1}^j (x_{obs,i} - \bar{x}_{obs}) \cdot (x_{model,i} - \bar{x}_{model})}{\sqrt{\sum_{i=1}^j (x_{obs,i} - \bar{x}_{obs})^2 \cdot \sum_{i=1}^j (x_{model,i} - \bar{x}_{model})^2}} \quad (3.38)$$

If the correlation is +1, it indicates the case of a perfect increasing linear relationship, and -1 if it is a decreasing linear relationship. Values in-between +1 and -1 indicates the degree of linear relationship between two sets of observations. A correlation coefficient of 0 implies there is no linear relationship between the variables. The square of the correlation coefficient ( $R^2$ ) indicates how much of the variance between the two variables is described by the linear fit.

## CHAPTER FOUR

### RESULTS AND DISCUSSION

#### 4.1 Introduction

The use of computational methods in analyzing soil mass dynamics makes it possible to evaluate, with a sufficient degree of precision and in a simple manner, the characteristics of a given slope under conditions of intense but periodic rainfall or irrigation events modelled from simple physics-based equations. Data from numerical results arising from the derived model are then compared with experimental data obtained from the laboratory flume for purposes of validation (Trani et al., 2020; Wines, 2020). Although the validation samples were independent of *in-situ* field conditions because they were disturbed in one way or the other during sample collection, the change in geology and other soil properties was assumed negligible.

This chapter gives an exposition of both numerical and experimental results as well as the deductions drawn from the findings arising from the study. The first part deals with spherical-capped slope sections mostly found in relatively steep slopes of Kamelil study area, which is characterized by soils of low clay content and by extension low cohesive strength. The second section outlines the results and discussion of the hydrological and kinematic characteristics regarding the relatively more cohesive soils found in Taptengelei area, for which double spherical-capped slope failure morphology is prevalent. Thirdly, hydro-dynamical model results as compared with experimental findings are discussed, with a view of applying this model to a wide range of slope sections. Finally, results of ANN models are discussed and compared with experimental data, with the aim of developing a framework for prediction and development of an early warning system.

## **4.2: Numerical Results, Experimental Validation and Discussion**

### **4.2.1: Spherical-cap-shaped slope morphology under planar translational failure**

#### **4.2.1.1: Overview**

This study is based on geotechnical and geophysical investigations undertaken on soil samples from Kamelil location, Nandi county. The first stage of the investigation involved derivation of a number of numerical models based on inertial forces and geophysical factors, while the second and final step was focused on testing the derived models with respect to laboratory experiments.

The overriding focus in this study was to formulate numerical models to be applied on a special case of a spherical-cap-shaped slope section. Amongst other assumptions, was first to consider the soil mass as a homogeneous rigid-perfectly plastic material obeying Mohr-Coulomb failure criterion, and secondly, assume the critical slip surface is parallel to the inclined homogeneous undrained slope (tangent to a firm base) through the toe. This is in accordance to earlier investigations by Zhu et al. (2015), who found out that for slope angle greater than about  $53^\circ$ , the slip plane is parallel to the inclination plane. For this research study, an inclination angle of  $58^\circ$  was selected. Five samples were tested, one of which was a control experiment. The results of each parameter measured were recorded and an average computed that was then used in the model for comparison.

#### **4.2.1.2: Results and Discussion**

In this study, a number of numerical models were derived from first principles based on inertial forces, shear state and rheological behaviour of the slope material, in this case, a soil mass (section 3.3.2.1). A number of physical parameters ranging from rainfall intensity to PWP were expressed as empirical equations while derived

quantities, especially FS and displacement, were expressed as dependent functions of the other factors. A comparative study of the numerical and experimental results for each parameter considered is outlined below.

#### **(a) Rainfall Model**

In general, most researchers use rainfall simulators that have been developed to simulate the typical conditions of natural rainfalls, such as impact velocity and size distribution of raindrops (Davidová et al., 2015). In this consideration, a numerical model (equation 3.12) describing a single pulsed representation of constant rainfall intensity (Ojha et al., 2014) over time was derived to describe the characteristics of the simulated rainfall, and by extension natural precipitation. In the experiment, a rainfall amount of 45 mm/hr lasting for 45 minutes was maintained for all the experiments. It was assumed that 45 minutes was long enough for all the rainfall water to infiltrate into the soil. This rainfall conditions were maintained in the study of soil-water characteristics of the slope at any given time. Computational results from the model for a single rainfall event as a function of time are compared to experimental data as illustrated in figure 4.1(a). The numerical model simulation results were found to fit experimental findings well with  $R^2$  value of 0.9641, implying this model holds a promise in describing rainfall characteristics in the field.

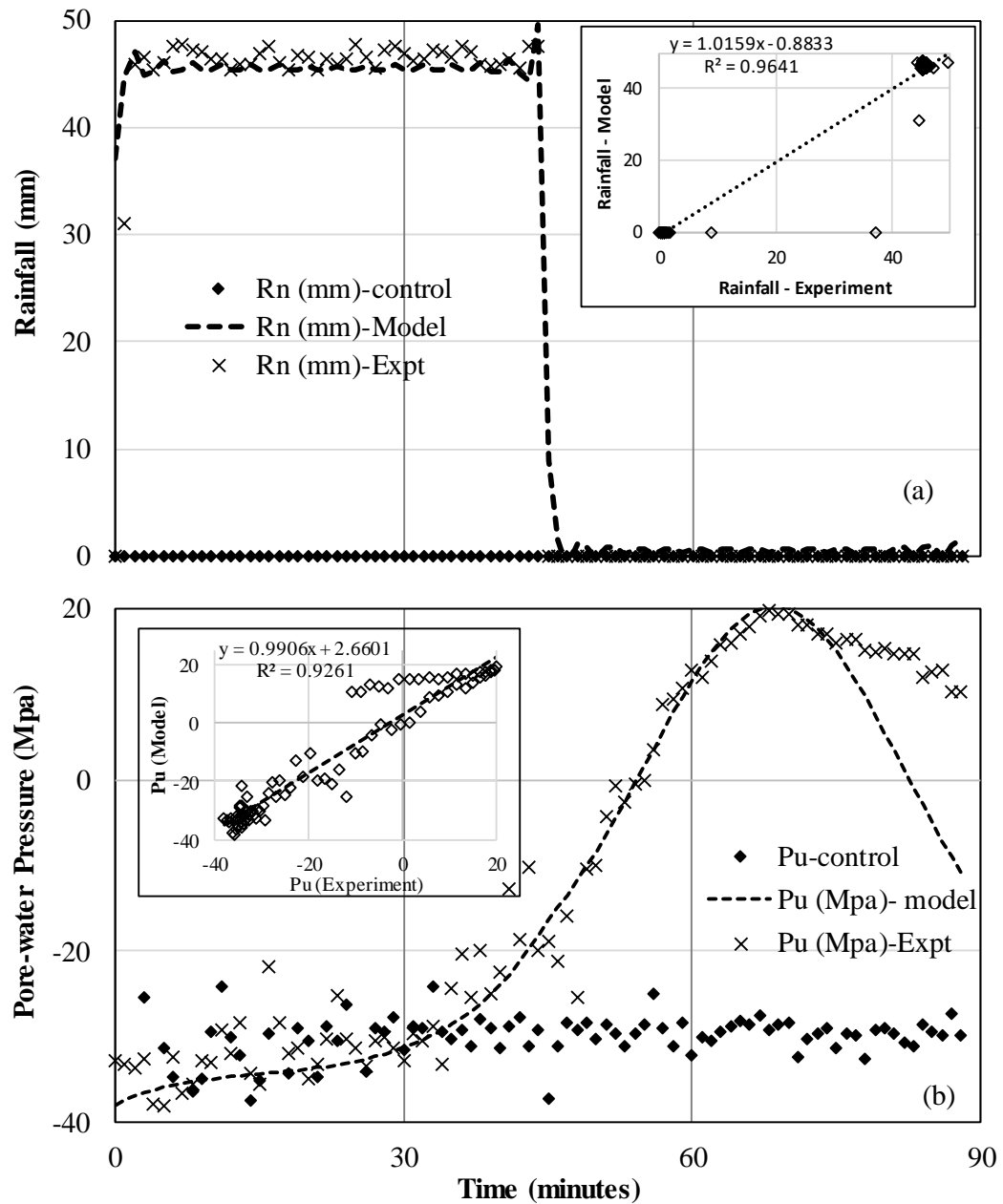


**Figure 4.1: Results of computational and experimental (a) Rainfall intensity; (b) Pore-pressure; as a function of time in minutes. Inset: statistical analysis**

### (b) Soil Moisture Content

Modelling and monitoring of VWC is a key step in understanding its variability in time and space as well as its exchange relationships with the surface and atmosphere for purposes predicting weather and climatic conditions as well as forecasting geological disasters and developing early warning systems (Brocca et al., 2017; Li et al., 2016). In this study, a numerical model for the VWC proposed by Fredlund and



Xing (1994) was employed in describing the soil water characteristics. This model was derived based on hydraulic properties of the soil, topographic characteristics, interaction with surface water systems, precipitation features, and meteorological conditions. Further studies led to the expansion of this model to take into consideration other factors such as specific moisture capacity, specific storage (computed as the inverse of the soil skeleton bulk modulus), pore water pressure (negative in unsaturated zone), time elapsed, relative permeability, dynamic viscosity of water and vertical elevation coordinates (Huang et al., 2016).

Since the intensity of rainfall was lower than the intensity of absorption, then according to Chekalin et al. (2017), the water layer that appears on the soil surface, will be too small and hence neglected in computation of the volumetric water content (VWC). In effect, all the water from the incident rainfall finds its way into the soil matrix by way of infiltration which serves to increase the VWC (Santos et al., 2014) leading to a corresponding rise in the weight of the soil mass (and by extension the normal stress) as well as a change in PWP, internal friction angle and cohesive stress. Numerical model simulation results for VWC over time were compared with experimental data as illustrated in figure 4.2(a) below. From the results, VWC was found to rise from a modest value of 20% (equivalent to the residual soil moisture content) to nearly saturation i.e. 93%, and began to drop steadily but with variations between model and experimental results.

Discrepancies between the simulated and measured soil moisture time series were noted especially at the fringes and near saturation conditions, which was attributed to variations in the hydraulic parameters (Gabiri et al., 2018) observed at different depths, soil heterogeneity, model uncertainty, and measurement errors (Gribb et al., 2009). The variations in the saturated hydraulic conductivity are caused by sampling

and measurement errors in addition to existence of macro pores due to soil cracking (Bodner et al., 2013). In addition, due to the hysteretic effect of water filling and draining the pores, different wetting and drying curves are obtained especially near saturation conditions (Chou, 2016). In general, this numerical model simulated the soil moisture characteristics with time reliably with a coefficient of determination of 0.9291.

### **(c) Pore water pressure**

Pore-water pressures (PWP) play an important role in defining the stability of rainfall-triggered landslides or debris flows, more precisely, in defining the slip surface (Cascini et al., 2013; Fredlund et al., 1978). PWP in the soil is a function of rainfall infiltration regime but the presence of coarse-textured unsaturated pumiceous layers at different depths also determines the PWP profiles (Damiano et al., 2017). Unfortunately, there exists no direct empirical or mathematical relationship between PWP and other parameters (Mustafa et al., 2015). In this study, an empirical mathematical model (equation 3.14) was derived from the van Genuchten equation to describe the relationship between PWP and VWC. This model is a function of rainfall infiltration, water flow, and drainage.

The derived model results were compared with experimental findings as illustrated in figure 4.1(b). Evidently, as the VWP rises as a result of the steady infiltration, the negative pore pressures remained almost constant in the initial stages because of the unsteady lateral water flow from a higher part to the lower part of the slope system, presence of pumiceous layers delaying the flow and impartial filling of pore spaces (Zhang et al., 2019). But after some time (for this case 30 minutes) there was an exponential rise in the negative pore-pressure peaking at 20 MPa, a point at which it

stagnates for some time, when the soil is nearly saturated, signifying almost all pore spaces are filled. The time taken for the PWP to peak is determined by the infiltration rate, drainage and type of soil (Zhang et al., 2019).

Computational results from the model agree well with the experimental data except that after failure, the model envisages a faster drop in pore pressures because of the envisaged steady drainage, but in the experiment, PWP remained almost constant because of the impermeable base of the flume retarding the vertical drainage. It was also observed that the pore-water pressures in the soil mass continued to rise even when the rainfall event had been halted indicating its strong dependence on infiltration rate rather than rainfall intensity directly. This means that pore-pressures will therefore vary according to the moisture content present in the soil at any given time regardless of the source of water. Numerical model results as compared to experimental data produced RMSE and correlation coefficient of 0.5473 and 0.9261 respectively, which indicates a close concurrence.

#### **(d) Factor of safety**

Introduction of water into the soil mass on a slope through rainfall infiltration or irrigation event serves to increase the weight of the sliding plane and lubricating the soil particles, thereby increasing the driving forces downslope and/or significantly reducing the shear resistive forces consequently leading to a drop in the factor of safety (FS). The value of the FS indicates the health status of a given slope. Values greater than unity indicate higher shear strength, while values lower than one point to a very unstable slope. The FS is a function of cohesion, moisture content, pore-pressure, internal friction angle, and slope angle (Wang et al., 2016; Wanatowski and Chu, 2012).

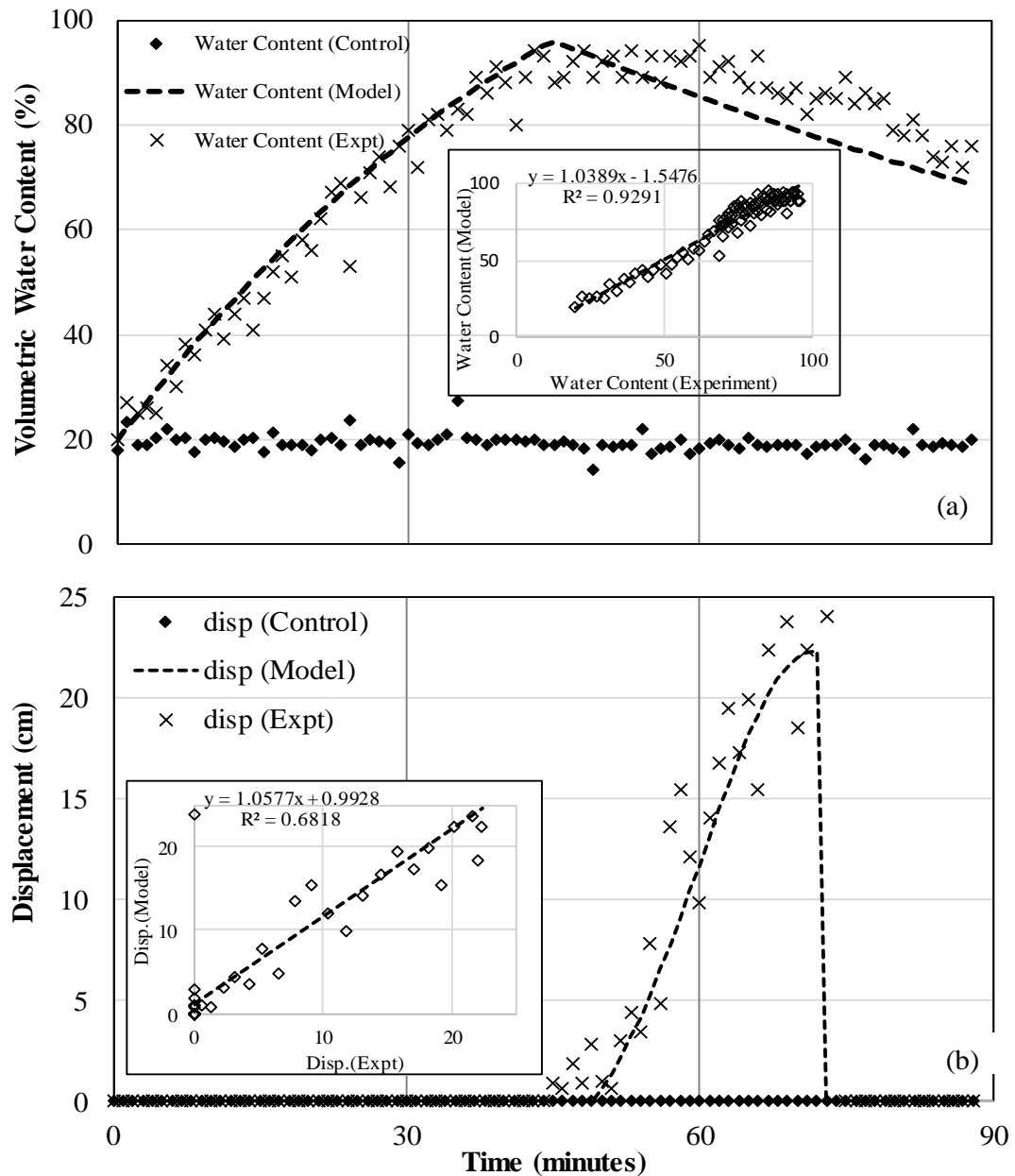


**Figure 4.2: Computational and experimental results of (a) Water content; (b) Displacement; varying with time in minutes. Inset: statistical analysis**

In this study, a numerical model describing the FS as a function of slope angle, cohesive stress, VWC, PWP and internal friction angle was derived. The computational results of this model are compared with experimental findings obtained using a laboratory flume as illustrated in figure 4.3. As evidenced from the figure, in the first 40 minutes, the FS remains averagely constant, because the PWP which is a function of VWC and is directly proportional to FS is still negative and low.

However, as VWC increases, a corresponding exponential rise in negative PWP together with a drop in cohesive stress leads to a decrease in FS to below unity, a state that exacerbates slope failure. Notably, it is observed that FS values drop significantly when the PWP rises to the positive phase. Furthermore, it was noted that PWP continued to rise while FS constantly dropped even when the rainfall event had been halted. These conditions are attributed to the continuous progression of the vertical wetting front and hydraulic conduction in the deeper layers of the soil.

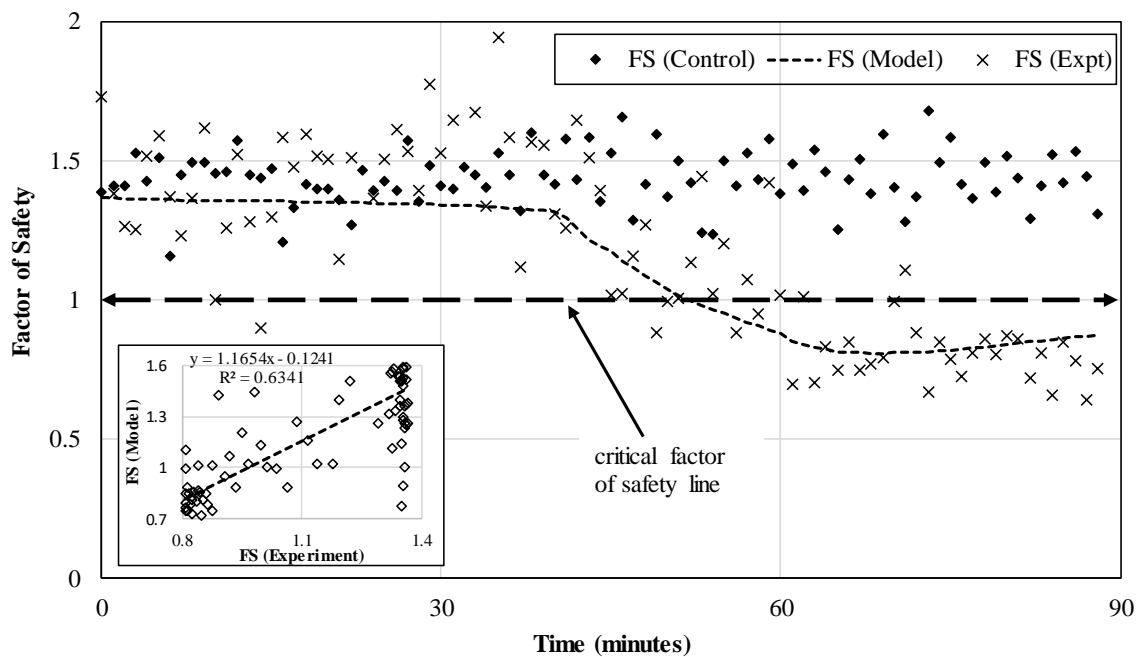


**Figure 4.3: Computational and experimental FS results with time**

Statistical comparison between computational and experimental results indicated a close agreement with RMSE of 0.0385 and  $R^2$  of 0.6341. This implies that the numerical model derived can be successfully employed in describing the stability status of a slope by way of factor of safety computations. However, discrepancies between experimental and numerical model results emanated from systematic errors

and presence of interlayer heterogeneity (Alvioli et al., 2016) in the slope material leading to formation of a number of stratigraphic fringes.

#### **(e) Downslope displacement**

Slopes fail when slope geophysical and geotechnical factors as well as lithological aspects are compelled to change by hydrological, seismic or manmade activities. Slope instability is evaluated by way of FS values less than one. In the unstable state, slopes fail by downslope motion of the soil or rock (Patil and Gopale, 2018; Fredlund and Rahardjo, 1993).

In this research study, a numerical model (equation 3.18) describing the downslope displacement of the soil material under wetting conditions was derived based on the FS, slope angle, gravitational acceleration and internal friction angle. Computational results from this numerical model were compared with experimental findings as illustrated in figure 4.2(b), with *RMSE* of 0.1496 and  $R^2$  of 0.6818.

From the figure (4.2(b)), the soil mass remained in the static state until after the 50<sup>th</sup> minute when FS values fell below unity, when small portions of the material began to move downslope, signifying genesis of imminent failure. It was observed that prior to failure, small cracks developed which slowly coalesced into bigger ones. Failure of the slope was confirmed from downslope displacement of the soil mass, characterized by toppling of small portions commencing from the developed cracks. In all cases, the slip surface was parallel to the slope inclination, because of the tangential gravitational forces.

Conventionally, failure in brittle materials begins with the formation of microcracks or flaws in the material. In rocks, as well as cohesive soils, failure begins at the grain boundaries, inter-granular cracks or tensile cracks that propagate from their tips

when frictional sliding occurs along the flaws (Lade, 2010). Wang et al. (2018), noted that the development of cracks in soils is a typical consequence of cyclic variations of VWC, while Yang et al., 2019 pointed out that cracks occur when soils swell/shrink as induced by drying-wetting cycles. Therefore, mechanical cracking significantly affects the hydraulic conditions of the soil leading to massive displacement downslope (Qi and Vanapalli, 2015), as such, it is a sure indicator of internal shear strains.

From the data, it can be seen that, even after the rainfall event had been halted, the FS continued to drop because the PWP kept on increasing. This explains why most slopes collapse several hours or sometimes a short while after a rainfall event. For this reason, it is recommended that slope monitoring should not be entirely based on rainfall parameters such as intensity and duration only to make predictions and decisions about slope health, as has been the case in many studies (Abraham et al., 2020; Pradhan, 2019; Zhao et al., 2019), but rather, monitoring internal triggers such as VWC profiles and PWP (Conte et al., 2020; Carey et al., 2019) should be made a continuous activity. In other words, monitoring of internal parameters especially VWC and PWP should be sustained for several days after the storm, as they are responsible for the development of internal stresses manifesting as microcracks (Qi and Vanapalli, 2015), leading to eventual slope failure.

#### **4.2.1.3: Summary, Conclusion and Recommendations**

Climatic changes, erosion, deposition, weathering, biological and human activities as well as other geological processes are responsible for the irregular morphology of the ground surface (<https://sciencing.com/topography-deserts-8178249.html>, accessed, 30/06/2020). In sloping areas, a variation in the soil characteristics usually gives rise

to uneven ground surface topography. Additionally, erosion processes and readjustment of the soil mass always leads to detours on the slope covered by vegetation or in some cases bare (Baartman et al., 2018; Gandhi et al., 2018). In this study, a novel hypothesis of considering the convex-shaped detours as spherical caps whose base lies along the incline plane is conceived.

Geohydrological and kinematic studies performed on these spherical-cap-shaped slope formations have given rise to a number of inferences. Firstly, for steep slopes whose inclination is greater than  $53^\circ$ , for which downslope motion is dominated by the gravitational component (Chatterjee and Krishna, 2019), translational displacement was the overriding mode of failure. Secondly, the derived numerical models regarding translational failure for spherical-cap-shaped slope sections have been shown to agree well with the experimental results obtained from measurements using the SPM system, specifically for shallow soil masses.

Finally, the model for the factor of safety and by extension the other hydrological models derived are unique in that they take into consideration the moist soil unit weight as opposed to earlier models which were applied only in extreme conditions of purely dry soil or saturated conditions. This model for the FS is also more convenient as it contains fewer variables as many of them are computed as empirical functions of the water content. This model for the factor of safety is convenient for shallow landslides at relatively steep slopes.

Since the study was confined to one particular angle throughout the experiment, it is recommended that further investigations should be done to extent the validation of these models in other hydrological conditions and angles. Similarly, different soil types should be tested to ascertain the reliability of these models. We also recommend an experimental testing of this model in the *in-situ* conditions at different locations.



#### 4.2.1.4 Novelty in the formulation

In this study, as anchored on the first objective, five significant findings were realized based on numerical formulation and experimental validation. These findings will serve the purpose of enriching the existing literature and constitutive modelling as well as introduce new mathematical equations that describe the motion of granular slope material, in this case soil from Kamelil escarpment, under antecedent rainfall conditions. These novel ideologies include modification of the existing constitutive models to better describe the experimental results as well as deriving new empirical models to represent slope parameters. These include:

- (i) Consideration of the soil mass as a nearly spherical-cap-shaped unit as opposed to the conventional method of slices;
- (ii) Consideration of the moist unit weight ( $\gamma_m$ ) in the computation of the wetness index and the effective unit weight as opposed to earlier studies where effective unit weight of the soil was either considered for purely saturated conditions or for purely dry soil skeleton.
- (iii) Proposal to model incident rainfall as a Fourier pulsed expression
- (iv) Modelling soil cohesion as a function of VWC
- (v) Proposed new equation for factor of safety based on the above conditions

## 4.2.2 Double-Spherical-Cap-Shaped Slope Morphology Under Planar Translational Failure

### 4.2.2.1: Overview

The second part of the study focused on soil samples collected from Taptengelei escarpment in Nandi county. The predominant soil type in the study area was averagely composed of 50% sand, 18% silt and 32% clay (Gachene and

Kimaru, 2003), with slope gradients rising up to  $58^\circ$  at the upper regions. Physical observation of these soils during the dry season indicates deep cracks at various sections, implying shear strains underneath due to drying-wetting cycles, common in clayey soils. Conventionally, soils with high content of swelling and shrinking clay will in general plastically deform at high volumetric water contents (Ngecu et al., 2004).

In the study, a model of a slope section composed of a homogeneous rigid-perfectly plastic material having a nearly spherical double-cap-shaped morphology defined on the lower side by a concave-shaped failure plane was considered. The pertinent assumption in the model was that failure must originate from a crack located at the head-side of the landmass while the toe must be saturated. Furthermore, the crack depth is assumed to be relatively deep enough to connect with the ground water table or perched phreatic surface.

A set of numerical expressions were derived with respect to the spherical double-cap-shaped slope sections. The computational results from these numerical models were then compared with experimental findings based on laboratory flume tests. Inferences captured from the results are then discussed forthwith.

#### **4.2.2.2: Results and Discussion**

The response to antecedent rainfall by a nearly spherical double-cap-shaped slope material was investigated in this study. Several geophysical and geohydrological aspects were monitored in order to establish the behaviour and failure conditions of a soil mass with this kind of morphology in a laboratory flume. A study of the numerical and experimental results for each parameter considered is outlined below. A summary of the measured and derived parameters is illustrated in table 4.1. In the

table, rainfall, VWC and PWP were measured directly while cohesive stress and FS were computed.

**Table 4.1: Summary of geotechnical parameters**

	<i>Rain</i> (mm)	<i>VWC</i> (%)	<i>C</i> (Pa)	<i>PWP</i> (Pa)	<i>FS</i> ( $\alpha=45$ )	<i>FS</i> ( $\alpha=50$ )	<i>FS</i> ( $\alpha=55$ )	<i>FS</i> ( $\alpha=60$ )	<i>FS</i> ( $\alpha=65$ )	<i>FS</i> ( $\alpha=70$ )
<i>MIN</i>	0	13.5	14560	-14100	1.39	0.61	0.61	0.06	0.06	0.00
<i>MAX</i>	45.3	79.9	36370	-100	9.27	6.78	5.80	4.02	3.06	2.48

#### (a) Rainfall characteristics

In this study, an artificial slope mounted in a laboratory flume with unconsolidated soil mass from Taptengelei enclave was treated to rainfall events lasting 45 minutes at a rate of 45.3 mm/hr. Because rainfall intensity is considered to take the form of a random temporal series of discrete events, in this study, it is assumed to behave as an idealized series with a uniform distribution. A discrete Fourier series model was chosen to model the simulated rainfall characteristics over time. This model was then compared with simulated rainfall as indicated in figure 4.1(a).

Rainfall intensity and duration has been identified as the key factor that fuels in soil or rock slopes. This is because most slope failures usually occur in rainy seasons or during irrigation events. For highly cohesive soils, instability is induced when rain water fills cracks thus recharging the potential failure surface and causing an upsurge in PWP (Lu et al., 2020).

#### (b) Soil Water Content

The soil water content is a function of topographic parameters (elevation, longitude, latitude, slope angle, and slope aspect), soil properties (soil bulk density, saturated

hydraulic conductivity, soil clay content, field capacity, and soil organic carbon content), climatic factors (potential evaporation, mean annual precipitation, and aridity index), land use, and rock fragment content (Li et al., 2019; Zhu et al., 2014). Assuming the soil mass is not covered by vegetation, the VWC will basically depend on rainfall amount, intrinsic soil properties such as hydraulic conductivity, clay content and slope gradient.

In this study, the cumulative rainfall was incorporated in the Horton's infiltration model, in order to compute the volumetric water content (VWC) in the soil (assuming no surface runoff and negligible evaporation). As a result, the VWC was observed to exponentially rise with time as the incident rainfall was kept constant to maximum value of about 80% but begun to gradually decrease when the incident rainfall simulation was stopped (figure 4.4). It is important to note that when the rainfall simulation was stopped, the decrease in VWC was gradual because of the apparent soil water storage capacity (Groh et al., 2020; Guo, 2020). Results from the numerical model and experimental data agree well within statistical assumptions with a coefficient of correlation of 0.9666.

Soil VWC has a direct impact on climatic factors, geological processes and by extension hydrologic cycles, biochemical sequences as well as the ecosystem (Briggs, 2016; Seneviratne et al., 2010). In slope stability studies, VWC has been identified as the proxy for landslide triggering mechanism as it leads to localized increase in PWP or decrease of matric suction (Wicki et al., 2020). Bogaard and Greco (2018) proposed cause-trigger-framework hinged on a combination of two processes i.e. causal factors (hydrological prewetting as a result of antecedent saturation) and triggering factors (meteorological triggering arising from saturation change), all of which are functions of VWC. They further underscored the fact that the rate of

saturation increase, especially for short-duration rainfall events, is the key trigger for shearing in soils. As a result, therefore, monitoring of VWC continually within an appropriate sensor-reporting framework, can serve as a reliable warning system for landslide processes.

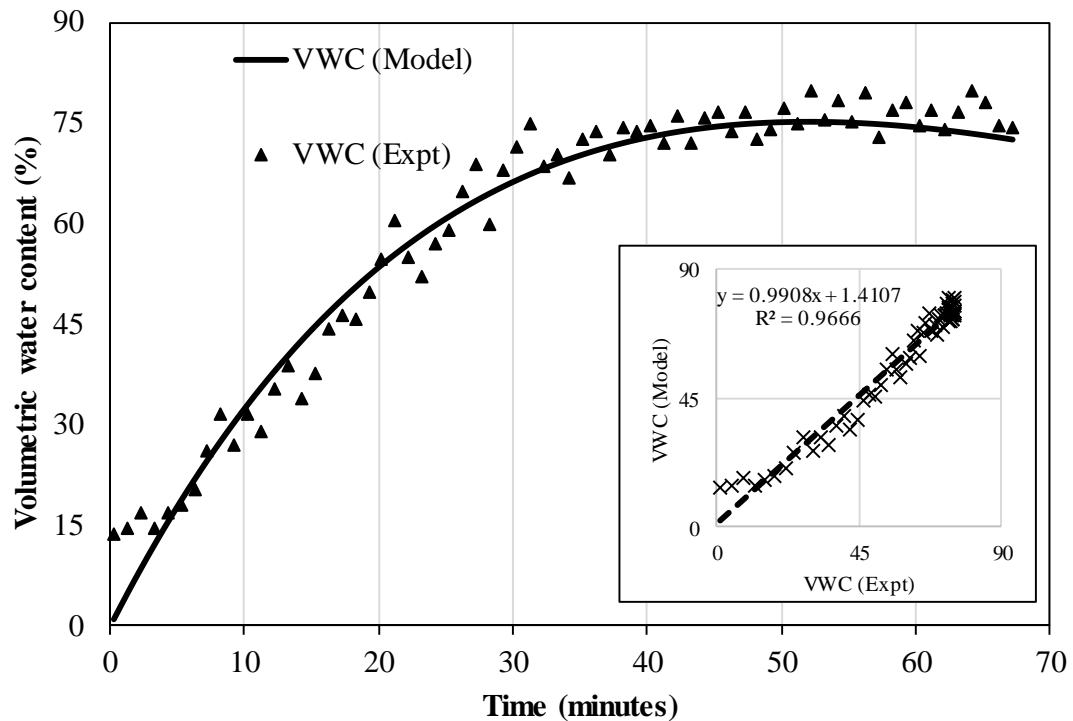


**Figure 4.4: Computational and experimental results of the volumetric water content as a function of time (Inset: statistical analysis)**

### (c) Pore water pressure

Pore-water pressure in the soil develops as a result of several factors including water elevation difference, unit weight, osmosis and water-air interaction (Chao and Ning, 2019). In unsaturated soils, PWP is usually negative, and this is attributed to the surface tension of pore water in voids throughout the vadose zone causing a suction effect on surrounding particles, referred to as matric suction (Das, 2011). When soil

VWC increases in the soil by way of infiltration, the matric suction is reduced causing a resultant decrease in the shear strength of the soil (Zhang et al., 2015).

In this study, a pair tensiometers were installed in the soil mass to monitor PWP characteristics. The results of the measurements were compared with the computational data from the mathematical model (equation 3.20), as illustrated in figure 4.5.

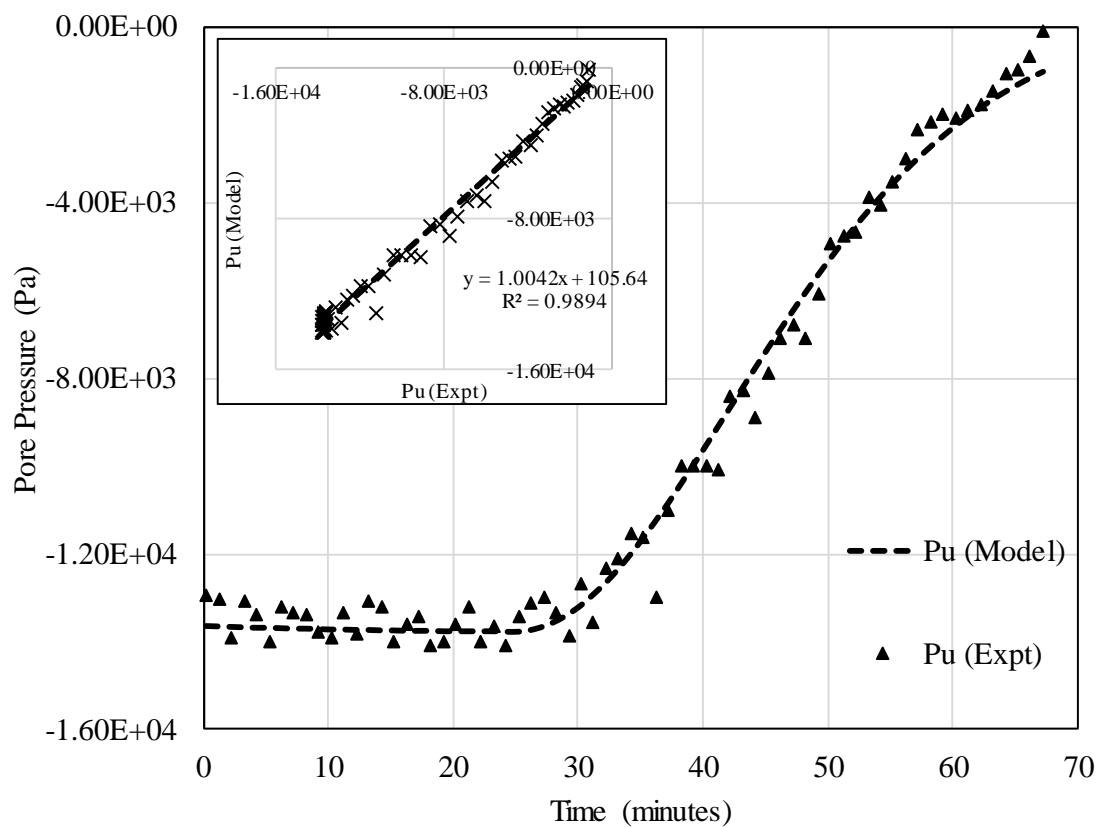


**Figure 4.5: Variation of pore-water pressure with time (Inset: statistical analysis)**

In the initial stages of the experiment, i.e. the first 26 minutes, the PWP remained averagely constant and negative, due to a larger elevation difference between the phreatic surface and wetting front (Coduto et al., 2011; Das, 2011). However, as infiltration gradually took place, the voids in the soil matrix were filled with water molecules, leading to a build-up in PWP. Because PWP is directly dependent on

infiltration rate (<http://environment.uwe.ac.uk/geocal/SoilMech/water/water.htm>, accessed 04/07/2020) and by extension the soil VWC, but not rainfall characteristics, it was established from the results that PWP continued to increase even after the rainfall event had been halted. PWP is a key factor in determining the value of the FS. Results of the model and experiment for PWP agreed well with  $R^2 = 0.9894$ .

#### **(d) Apparent soil cohesion**

In general, the bulk cohesion of granular materials is controlled by intrinsic material properties (surface energies, elastic moduli), particle properties (size, size distribution, morphology) and liquid content in the system (Herminghaus, 2005; Begat et al., 2004). In wet granular media, cohesion arises from van der Waals forces, electrostatic forces, surface tension and liquid bridging (capillary effects) (Landau and Lifshitz, 1987). Cohesive stress is directly proportional to the shear strength of a material and by extension the factor of safety (Piciullo et al., 2018).

Researchers in the field of materials science and fluid mechanics have proposed rheological equations and mathematical models that describe the characteristics of cohesive materials especially granular media. In most cases, the models are based on elasto-plastic, visco-elastic or in combination to investigate the effect of cohesion on the micro and macro behaviour of granular assemblies (Kievitsbosch et al., 2017; Adams and Perchard, 1997). In this study, the apparent soil cohesion was derived from its relationship with VWC and intergranular interface (equation 3.15). computational results from the model were compared with experimental as indicated in figure 4.6.

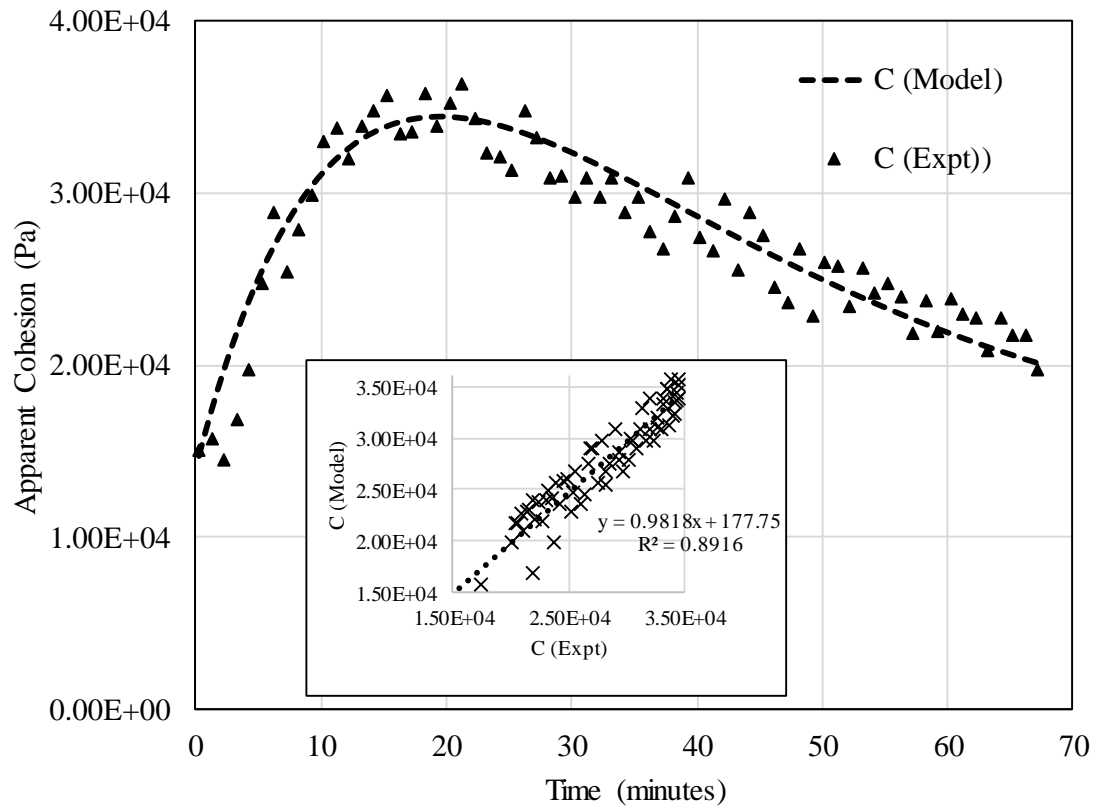


**Figure 4.6: Pore-water pressure profile as function of with time for a soil slope (Inset: statistical analysis)**

From the data, apparent cohesive stress was found to gradually increase from a modest value of  $1.41 \times 10^4$  Pa to  $3.45 \times 10^4$  Pa during the first phase of wetting as a result of infiltration but exponentially dropped as the water content in the soil matrix increased. This trend is attributed to the dependence of cohesive strength on the amount of liquid (in this case water) in the granular system. In other words, the presence of water molecules in the granular medium lead to a change in the cohesion due to capillary, electrostatic, and van der Waals forces (Vondráčková et al., 2016; Kimiaghalam et al., 2016).

In a wet system, particles exist in three distinct states depending on the water content i.e. pendular state (low moisture content), funicular state (intermediate moisture content), and the capillary state (high moisture contents) (Iveson et al., 2001). In the pendular state, all particles are held together by liquid bridges at their contact points,



hence cohesive stress will increase exponentially with VWC. In the funicular state, pores are partially saturated by liquid, leading to a steady decrease in the cohesive stress, proportional to the degree of saturation. Finally, in the capillary state, all voids between particles are filled with water molecules, resulting to complete loss of cohesive strength (Seemann et al., 2008). This is the reason why cohesive stress increases exponentially with VWC at low water contents but decreases when the water content is increased beyond the critical limit (Begat et al., 2004).

#### **(d) Factor of safety**

The stability of soil slopes is a function of shear stresses acting on the slip surface. In general, the stability of a slope is evaluated by way of a factor of safety (FS), basically defined as the ratio of the soil shear strength to the shear stress of a possible sliding surface in the slope. There are several factors that affect the stability of slopes and by extension modify the FS characteristics. These factors include slope angle, cohesive stress, internal friction angle and pore-water pressure (Li and Chu, 2019; Das 2011).

In this study, a numerical model was derived based on intrinsic soil properties and soil water content to describe the characteristics of FS on a soil slope. Six experiments were conducted based on soil slopes at six different inclination angles in a laboratory setup using a flume. For each angle considered, both computational and experimental results were compared and a corresponding coefficient of correlation obtained (figure 4.7).

It is discerned from figure 4.7 that the FS, for all angles, at first increases steadily, but after a short time (approximately 5 minutes), a sudden drop is witnessed. This trend is attributed to an increase in apparent cohesion with VWC in the initial stages, but after a short while, the cohesive stress will begin to decrease while the PWP will begin to

rise leading to a steady drop in FS. In cases where the recorded FS values were below unity, i.e. when shear stresses were dominant/exceeded frictional and drag forces, the slope failed. Because of the non-uniform wetting front in the soil mass, failure was preceded by growth of randomly distributed cracks, collapse of small portions and thereafter translation of the larger mass leaving a dome-shaped void resembling an inverted spherical cap.

Fellenius (1936) proposed the method of slices while Bishop (1955) came up with the method of slip circle in the stability analysis of slopes. These two methods, although still used by some engineers, ignored the impacts of the stress state and its variation as prerequisites of slope stability (Zhu et al., 2017). In the last decade, many researchers have strived to investigate and identify the sliding centre and slip surface (Zheng and Tham, 2009). In most cases, the results of these studies led to overestimation of the available shear strength (and by extension the FS) or underestimation of the FS (Galavi and Schweiger, 2010).

In mitigating the shortcomings of the previous analysis methods, Chae et al. (2015) presented a modified equation of infinite slope stability analysis based on the concept of the saturation depth ratio to analyze the slope stability change associated with the rainfall on a slope. This method eliminates the need for approximating the slip circle location and centre. However, this method does not give any description regarding the shape and form of the sliding mass before and after failure. In reality, post-failure observation in areas where landslides or debris flows have occurred reveals that the sliding mass left a dome-shaped hole with respect to the ground surface (Friele et al., 2020; Wang et al., 2018).

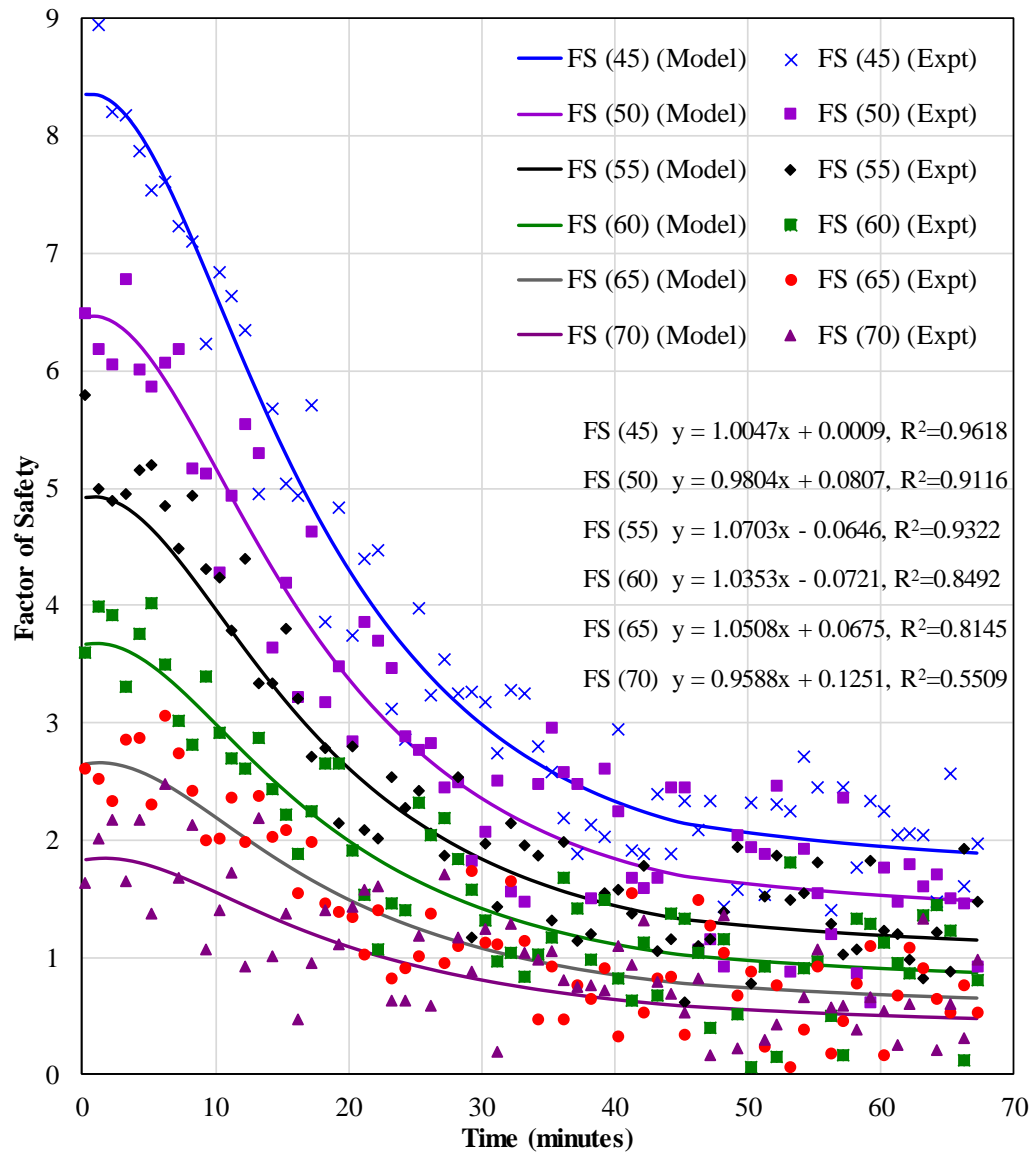


**Figure 4.7: Factor of safety (model and experimental) profiles for different angles as a function of time**

In this study, spherical double-cap shaped soil mass was presented against earlier studies that were based mainly on wedge-shaped failure mass or imaginary slip circles (Hazari et al., 2019; Gutiérrez-Martín et al., 2019), while accounting for the initial shape of the sliding mass as evidenced from the vacancy left after failure. This postulation was based on the fact that rainfall infiltrates into the soil along a gravitational gradient that is not linear but rather curved outwards, like a convex

surface. If a discontinuity like a crack or a flaw exists at the upper end of a cohesive soil mass, it will provide preferential water flow channel that will act as the initial point of the critical slip surface or form a perched phreatic surface for shear displacement to occur. This slip surface originates from the crack tip and terminates at the toe side of the slope, but describing a nearly circular path. This surface acts as a slip surface for the upper soil mass to undergo translational displacement when shear strength is diminished. In this case, the vacancy left after failure will resemble a spherical cap on the lower side, with the incline plane as the base. Since the outer portion of the slope also resembles a spherical cap, the ideology of spherical double-cap morphology with a common base line, as modelled by the numerical equation and confirmed from laboratory experiments, is validated.

Discontinuities in the soil mass such as cracks are usually caused by differential settling, drying and shrinking of soil, and associated construction activities. Presence of cracks in soil slopes affects the stability of the slopes through three effects. First, cracks provide preferential flow channels which increase the soil permeability and decrease the soil strength. Second, water-filled cracks exert an additional driving force on the slope. Finally, cracks can form a part of the critical slip surface that has no shear strength, hence inducing failure (Raghuvanshi, 2019; Salunkhe et al., 2017).

Geological and hydrological characteristics of a discontinuity surface such as orientation, roughness, aperture and continuity determines the potential failure plane on the soil slope (Johnson and Degraff, 1991). For these reasons, experimental as well as numerical simulations have proved the presumption that in the presence of cracks at the upper part of the slope, the failure volume takes the shape of a spherical double-cap.

#### **4.2.2.3: Summary, Conclusion and Recommendations**

Evidently, a cohesive soil (generally rich in clay content) with discontinuities on a slope of modest inclination angle, will most likely fail as a block but not wedge-like as is commonly assumed in many research findings. As has been established in this study, the failure mode is determined by the nature and orientation of discontinuities and from the vacancy left when the soil mass has failed. In this study, it was actually dome-shaped resembling a section of a sphere. Analysis of pre- and post- failure formation of the slope has revealed that the best approximation of this failure mode is double-cap shaped slope morphology, as proposed. The underlying assumption in this study is that the slope material must be relatively shallow, with inclination angle between  $50 - 58^\circ$  (Zhu et al., 2015), high clay content (highly cohesive) and presence of one or more cracks at the head of the landmass.

#### **4.2.2.4 Novelty in the formulation**

In conclusion, two outstanding outputs were realized from the research study as an enrichment to earlier constitutive models:

- (i) Consideration of the sliding soil mass as a spherical double-cap-shaped unit with the failure line appearing as a section of a sphere as opposed to the conventional circular-shaped failure line.
- (ii) Derivation of a new equation for the factor of safety based on spherical double-cap morphology

### **4.2.3 Hydromechanical Landslide Model**

#### **4.2.3.1 Overview**

Soil mass movements are complex processes possessing high spatial-temporal variability. Many scientific studies have strived to establish mechanisms and triggering factors for slope failure through numerical models and rigorous experiments for many years. Amongst many other parameters, the most recent studies through field observations and measurements have indicated that most slope failures in unsaturated soils are triggered by hydrological factors and/or earthquake events (Wicki et al., 2020; Guzzetti et al., 2009). This is in reaction to the realization that most triggering factors are intrinsic functions of the VWC either directly or indirectly (Wu et al., 2015).

In essence, both causal factors (hydrological pre-wetting as a result of antecedent saturation) and triggering factors (meteorological triggering arising from saturation change) are modulated by VWC. In other words, the rate of saturation increase, even for short-duration rainfall events, is the key trigger for shearing in soils (Bogaard and Greco, 2018). As underscored in the mathematical formulation (chapter three), slope parameters are all dependent on VWC and by extension the shear strength of the slope. It is in this context that a hydromechanical model (equation 3.30 - 3.32), which incorporates all hydrological factors affecting slope stability, was derived. Computational as well as experimental results for the hydromechanical model describing both the shear displacement and factor of safety for a soil mass inclined at different angles is presented.

#### 4.2.3.2 Research output and Interpretation

In this experiment, a series of six experiments were setup to evaluate the performance of the derived hydromechanical model on a soil mass at different inclination angles ( $30^\circ - 70^\circ$ ) in terms of the factor of safety (FS) and shear displacement. To achieve these objectives, laboratory flume experiments were undertaken to simulate field conditions. Generally, flume experiments allow the study of these processes under controlled and easily observable conditions (Aldefae et al., 2019).

For each inclination angle considered, a soil mass was placed in a flume in layers beginning with a 5 cm layer of coarse sand at the base, then soil layers on the upper part. The physical properties of the collected soil samples are shown in table 4.2. A rainfall simulation was then applied for a period of 45 minutes. In the process, sensing elements installed in the flume recorded a number of geotechnical and geophysical parameters considered in the computation of the FS. Runoff and radial seepage were assumed negligible in these experiments.

**Table 4.2: Physical properties of the soil samples (before the experiment)**

<i>Parameter</i>	<i>Value</i>
Specific Gravity	2.73
Field Density (Kgm <sup>3</sup> )	15.8
VWC (%)	12.9
C (kPa)	17.2
PWP (kPa)	-47.9
Internal friction angle	23.9

In this study, a hydromechanical model based on elastoplastic properties of the soil was used to describe the variation of the factor of safety with VWC (Chueasamat et al., 2018) at different inclination angles. As such, these experiments were geared towards establishing the behaviour and role of VWC as it infiltrates into the soil on the stability of slopes. Each of the physical parameters affecting the FS are considered in detail in the next section.

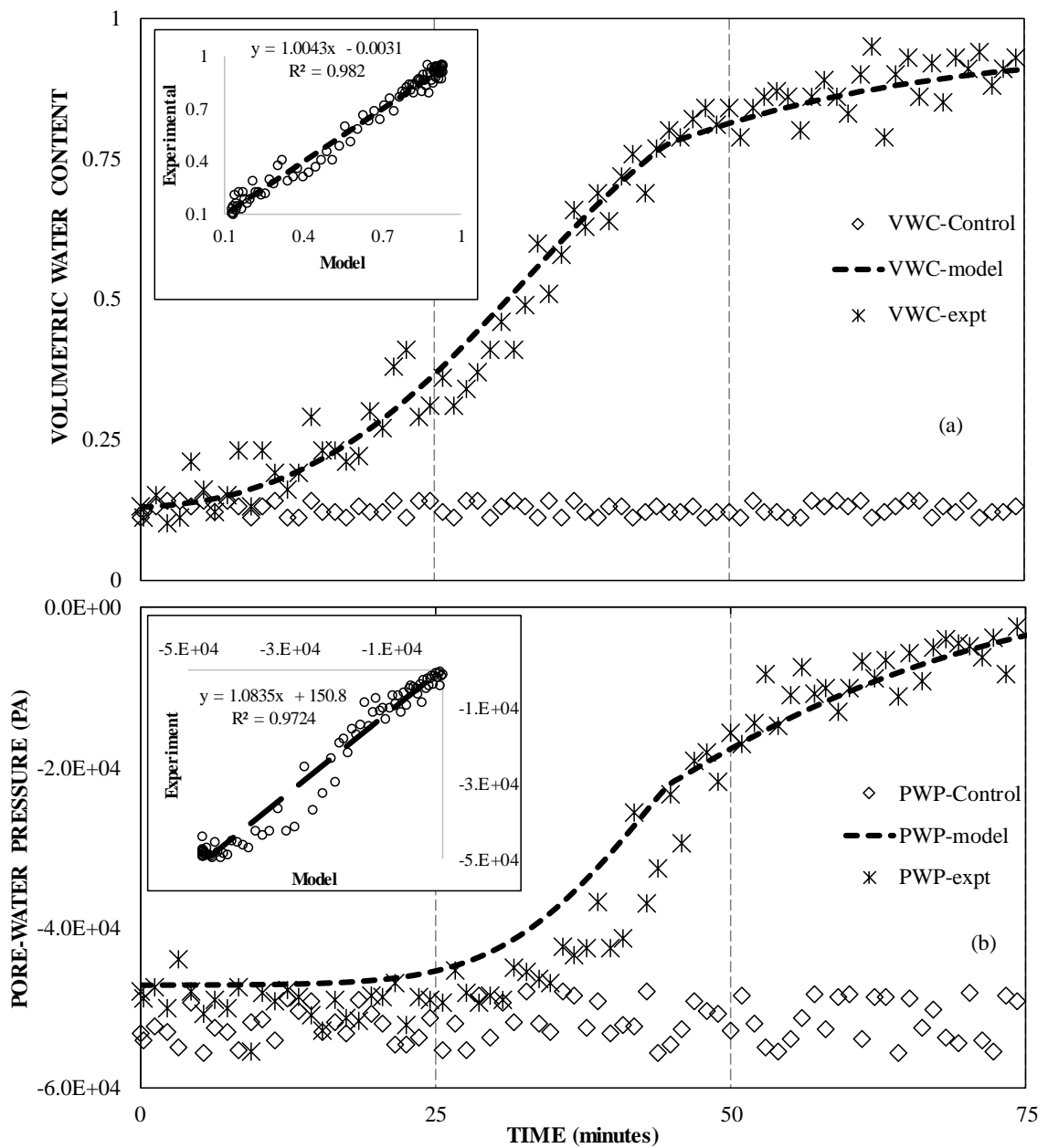


**Figure 4.8: Plot of (a) volumetric water content (VWC) and (b) pore-water pressure (PWP) with time**



**(a) VWC and PWP**

In all the experiments (figure 4.8(a)), a steady increase in VWC as the incident rainfall gained entry into the soil mass via infiltration was observed. Since the distribution of non-triggering infiltration events to slope instability are clustered around 60-75 % antecedent saturation, which is the potential range of the field capacity (Assouline and Or, 2014), a VWC value above this range was chosen. For this reason, the rainfall simulation was halted at 45 minutes into the experiment, corresponding to antecedent saturation of 94%.

Furthermore, it was observed from the data (figure 4.8(b)) that increase in VWC led to a significant change in PWP (Damiano and Olivares, 2010; Rahardjo et al., 2007), for all experimental scenarios. Notably, for the first 30 minutes into the experiment, PWP remained constant and negative, even when the VWC had risen to about 30 – 35%. However, as the wetting front progressed downward, a phreatic surface formed at the base of the flume leading to an increase in PWP with the steady infiltration. After 45 minutes into the experiment, when the rainfall simulator was stopped, the PWP had reached -7.8 kPa, but continued to rise because of the ensuing downward infiltration leading to a rise in the water table.

As a consequence of the rising VWC and PWP, tension cracks began to appear on the surface of the soil mass. It was however deduced from the data that these cracks emanated from the rapid pore-water pressure rise due to the increase in the water level (Damiano et al., 2017). Although shear stress measurements were not performed, because of laboratory limitations in terms of equipment like triaxial machines, it was deduced from the experimental results that the shear strength of the soil mass drastically deteriorated when the PWP increased, leading to crack formation and eventual failure (Yang et al., 2019; Wang et al., 2018; Qi and Vanapalli, 2015).

**(b) Factor of safety**

Conventionally, the health status of slopes is analysed by application of the Mohr-Coulomb criterion and computation of the factor of safety (FS) against probable failure. Basically, the FS is usually calculated as an empirical function of the slope angle, PWP, cohesion, and internal friction angle (Orense et al., 2004). However, in this study, the derived hydromechanical model (equation 3.32) was modified in such a way that FS is directly dependent on the VWC and PWP as well geotechnical factors such as slope angle and internal friction angle.

Experiments based on a laboratory flume together with a rainfall simulator were performed to establish the relationship between VWC and PWP on FS and by extension displacement leading to eventual failure. Results from the measurements were used to compute FS values for inclination angles ranging from 30–70° (figures 4.9(a)–(e)). From the data and as illustrated in figure 4.9(a)–(e), the FS remained above unity (implying no failure or displacement even in near saturation conditions) for slope angles 30° and 40°. At slope angles of 50° and 60°, the soil mass collapsed 19 and 5 minutes after the end of the rainfall event when the VWC had reached 88% and 84% respectively. Finally, for the slope angle of 70°, the soil mass failed 43 minutes from the beginning of the experiment when the VWC approached 76%. Statistical comparison between experimental and computational yielded a significant agreement based on  $R^2$  values which were greater than 0.9 for all the experimental trials. This underpins the accuracy of the derived model in predicting the FS of a soil mass.

From the results, it was noted that, at low values of the VWC, the FS exponentially increased with time corresponding to an increase in VWC until a critical point was reached referred to as the ultimate cohesive strength (UCS). At this point, water

molecules make relatively stronger bonds with soil grains due to adhesive forces compared to soil interparticle bonding. In this case, water molecules form a single layer that acts as an interface between soil grains, resulting in a material with comparatively stronger bonds. When more water is added into the soil mass, more water molecules occupy the space between soil molecules forming a new layer that makes bonds with water molecules adhering to the soil grains. This new layer causes electrostatic shielding between the soil grains and as a consequence the soil cohesive strength is drastically diminished (Zhu, 2019; Wagner, 2013).

Additionally, a drop in the cohesive strength was reflected in the system by a decrease in the FS (Aharonov and Scholz, 2018). However, the instantaneous rise in PWP was responsible for the final loss of soil shear strength and by extension the FS (Li and Chu, 2019; Zhang et al., 2015). Basically, when the inclination angle increased, the downward gravitational component of the driving force also increased in obedience to Newton's second law of motion, consequently lowering the shear strength and FS of the soil mass (Yang, 2019; Parsons and Milburn, 2018).

### **(c) Shear Displacement**

As indicated in section 3.3.4.3, measurement of soil mass displacements was done using a pair of ultrasonic range sensors mounted on the front side of the flume. Displacement occurred when the soil mass lost its residual shear strength (Brakorenko et al., 2019; Fredlund and Rahardjo, 1993). As alluded to earlier, slope failure as evidenced by displacement downslope began with the development of cracks on the surface which coalesced into bigger ones and eventually formed a demarcated boundary of the failing mass (Zhang et al., 2015). Figure 4.10 gives a graphical

illustration of the measured displacements for inclination angles ranging from 30 – 70°.

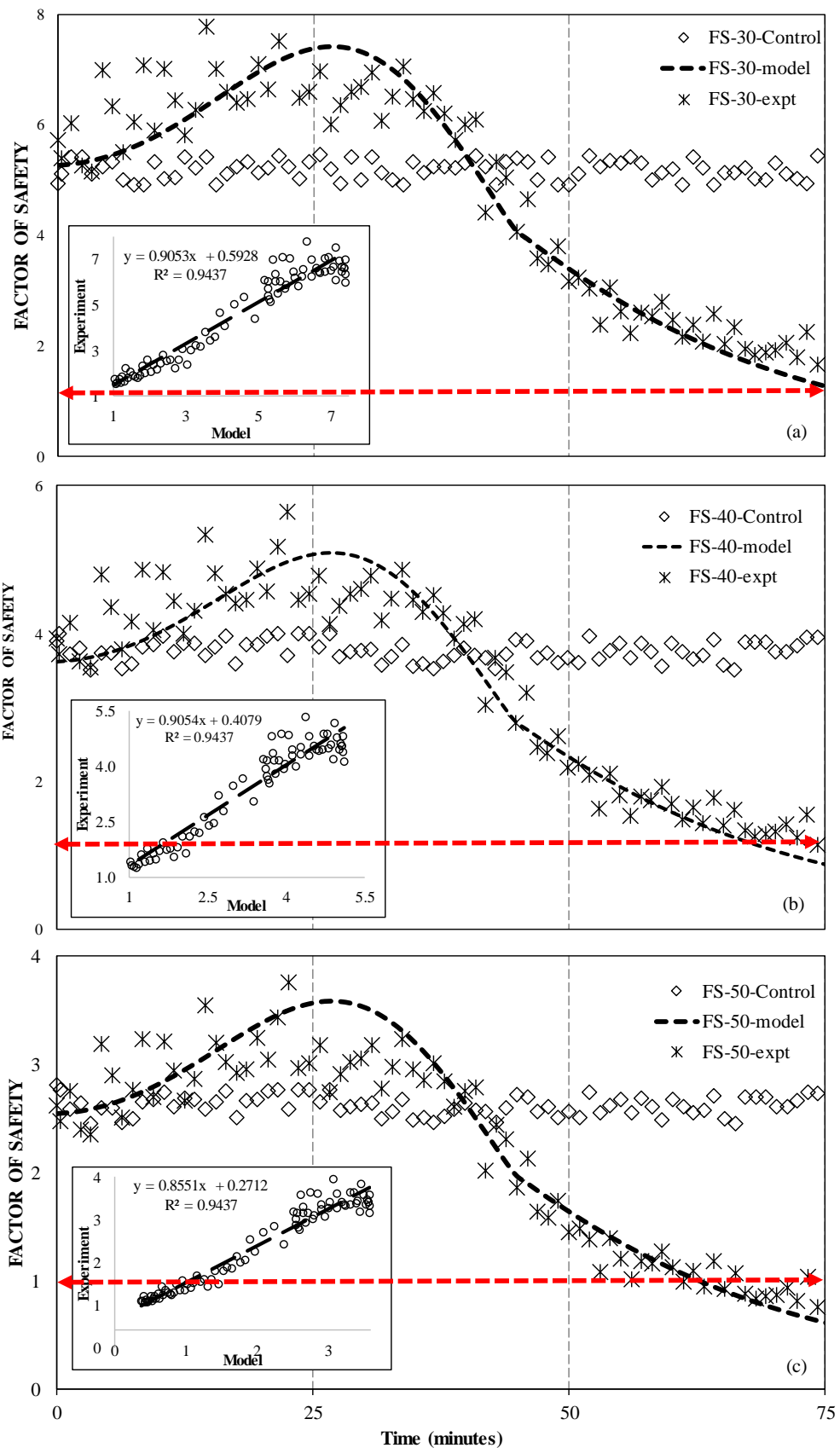
From figure 4.10, it is observed that there is no change in slope movement until 43 minutes (for slope angle 70°), 54 minutes (for slope angle 60°) and 63 minutes (for slope angle 50°) from the beginning of the experiment, when bulk soil displacement was registered. However, there were some infinitesimal displacement values recorded until this time point which were not considered in the analysis because they were regarded as noise arising from the electrical signal generated during transmission of the data.

From the measurements, maximum displacement of 0.8 m was recorded, due to the size restrictions of the flume used. From the data, it was noted that the higher the slope angle the higher the displacement relative to the original position. In addition, results from shear displacements in the soil mass were used to compute the values of the acceleration for each angle considered. The average values of the computed acceleration of the soil mass downslope were found to be 0.01340, 0.01791 and 0.01943 m s<sup>-2</sup> for slope angles 50°, 60° and 70° respectively.

#### **4.2.3.3 Summary, Conclusion and Recommendations**

Based on experimental tests carried out, the type of failure mechanism was found to be retrogressive planar displacement due to gravitational shear stress as recognized from the appearance of tension cracks along the surface of the soil mass before failure (Liu et al., 2020; Bouissou et al., 2012). This is because, crack location, depth, size, and direction on a slope is usually the evidence of rising pore-water pressures underneath (Mukhlisin and Khiyon, 2018). Furthermore, the failure surfaces formed

in these experiments were of the shallow and non-circular (translational) retrogressive type.



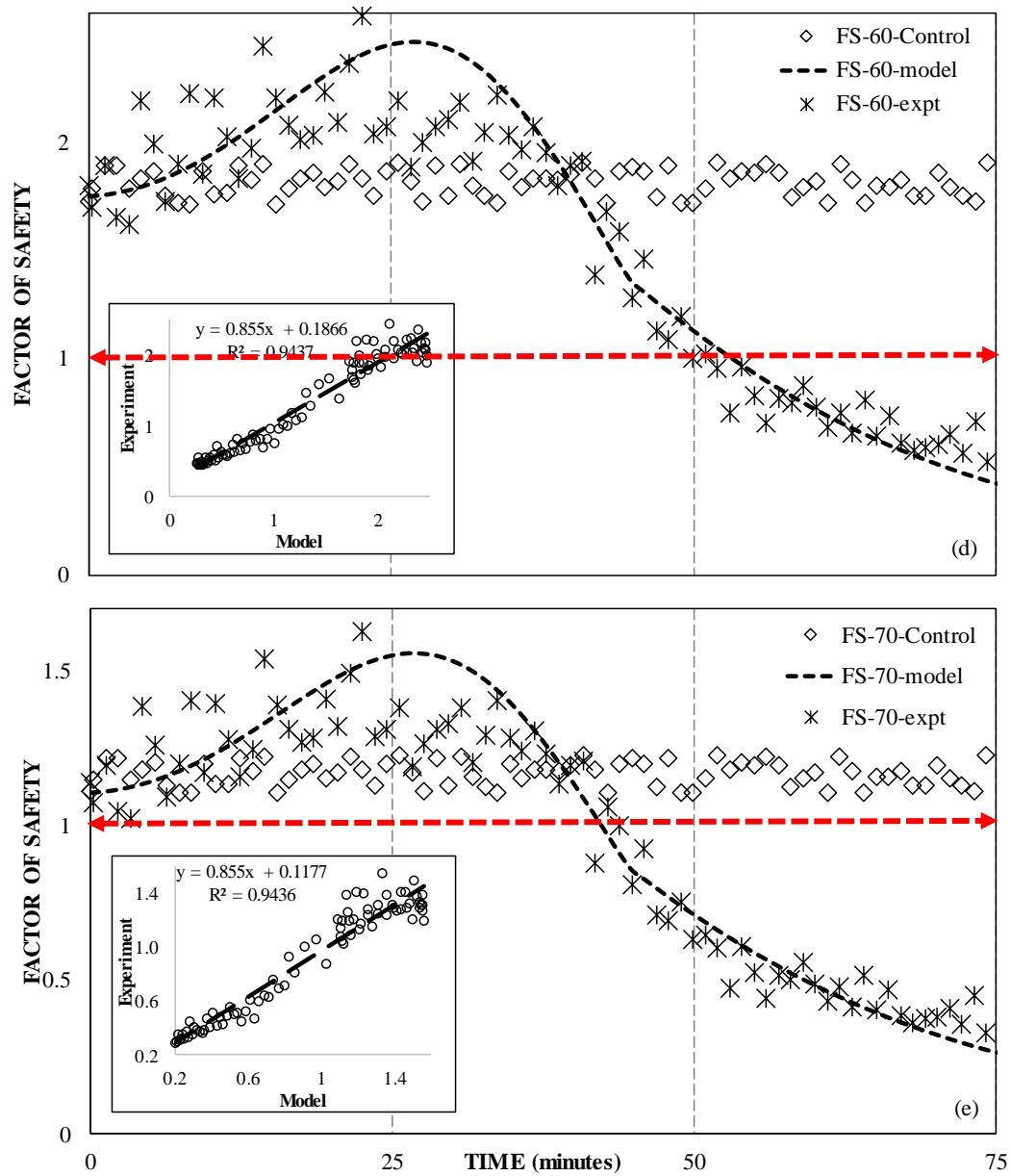


**Figure 4.9: Characteristics of the factor of safety for slope angles (a) 30°, (b) 40°, (c) 50°, (d) 60° and (e) 70° with time under wetting conditions. Inset: Statistical comparison between model and experimental data for correlation purposes**

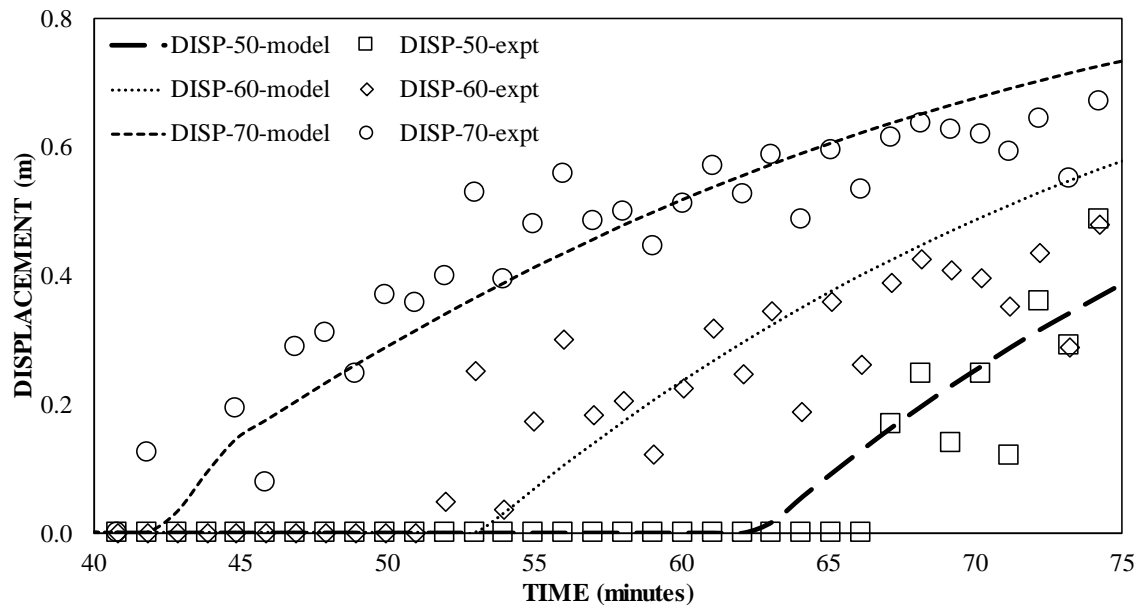


**Figure 4.10: Variation relative displacement with time**

In conclusion, it is discernible from the experiments that the factor of safety, which is an indicator of slope stability, is modified greatly by the slope angle, VWC and PWP (Duncan and Wright, 2005). In addition, based on the above causes, the increase in soil moisture content associated with rainwater infiltration is significant in inducing slope failure.

The hydromechanical model as derived for the factor of safety conceived a remedy to many geotechnical scientists in terms of the simplified equation and the reduced number of variables required. More pertinently is the exclusion of direct measurement of cohesive stress which requires relatively expensive triaxial tests to monitor. The model requires only two physical parameters i.e. VWC and PWP to ascertain the health status of a given slope. An additional measurement of displacement will be used to confirm the initiation of deformation when the FS is below unity. Therefore, the displacement obtained in this study represents the stage at which plastic deformation occurs but not the runout displacement.

A comparison between experimental data and the hydromechanical model revealed a close agreement ( $R^2$  values above 0.9) for both FS and shear displacement. This implies that the derived model can be employed in describing slope stability cases in soil slopes. However, since this model was tested in a controlled environment (laboratory flume), it is recommended that it is also tested in situ field conditions.

In this section, two novel ideologies were presented in the scope of slope stability studies involving cohesive soils, namely

- (i) First, the numerical model for the factor of safety (equation 3.31) is unique in the sense that if the slope height and angle are known, only three measurements (VWC, PWP and internal friction angle) can be made to establish the stability index of the slope, as opposed to earlier models which required monitoring of shear and cohesive stress directly.
- (ii) Lastly, the threshold VWC for slope failure as derived, can be utilized in the development of an early warning system.

#### **4.2.4 ANN Model Results**

##### **4.2.4.1 Overview**

Slope stability is a state influenced by various factors ranging from slope geometry, stress conditions, and soil properties. External water loading, pore-pressure changes, and hydrodynamic impact from water flow are the major determinants of actual soil properties. Prediction of slope movements is complex owing to the non-linear dependence of the causative parameters on each other. This means that common physics-based relations cannot apply and therefore a general need to study these processes together with the underlying uncertainties using new methods of prediction such as using intelligent artificial neural networks. ANNs once trained, will predict



with relatively high precision the likelihood of slope failures (Chakraborty and Goswami, 2017; Lu-Sheng et al., 2002). In this section, a description of the developed ANN model is given together with the training, testing and validation results as well the descriptive statistics relating the predicted and target data.

#### **4.2.4.2 Results and Validation**

##### ***Model architecture***

The prediction power of a model is a function of its generalization competence. To achieve competent generalization, early stopping is usually preferred to avoid overfitting (Carbune et al., 2020; Golovin et al., 2017). In this study, a data set of 297 points collected from experimental trials in Kamelil escarpment were randomly split into two sets; 80% (247) for model training (to compute the gradient and updating of the network parameters, such as weights and biases) and 20% (50) for model testing (to test the model error validation). Input parameters included: soil water content, apparent cohesion, pore-water pressure, slope angle and internal friction angle while the target data was the factor of safety.

A multilayered ANN was used to develop a model using non-linear combinations of the input parameters (Hastie et al., 2001). The ANN employed in this study is a feed-forward network with sigmoid activation functions in the hidden layers and a linear activation function in the output node, as generated from the commercial software Neuroph<sup>®</sup> and Microsoft Excel<sup>®</sup> embedded program ForecastXL<sup>®</sup>. During ANN development, it is a requirement that the learning rate, number of nodes in a hidden layer, and maximum number of training epochs are stated (Hill and Minsker, 2010). In this study, 8 neurons in hidden layers with 5 input variables, 0.8 learning rate, and

1 output variable in the output layer were employed in building the neural network (figure 4.11).

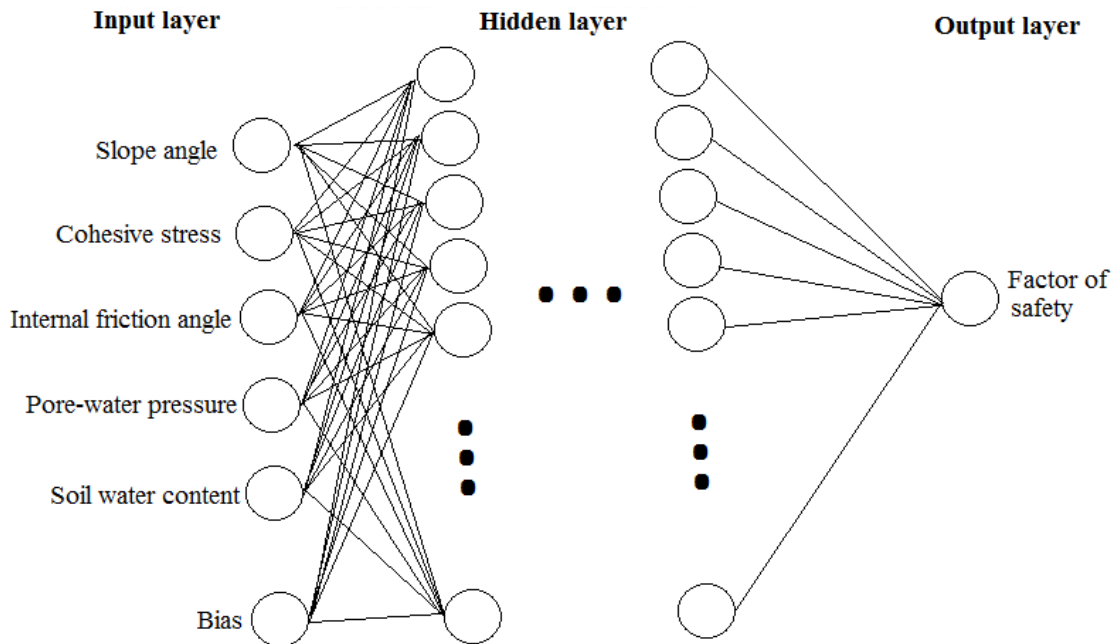


**Figure 4.11: ANN structure**

### **Model calibration**

The input and output data collected from experiments performed on soil samples were first pre-processed by scaling each variable to the range of -1 and +1 (appendix 1) so as to be fed in the network for training. The descriptive statistics of the data used in the development of the ANN model are shown in table 4.3.

During ANN model training, experimental values were compared with predicted output and a mean square error (MSE) calculated for each dataset. A summary of the training and test set is shown in table 4.4 indicating an average mean square error of 0.0047601 for the training data and 0.0026292 for the test set translating to an overall relative error of 4.56 %. From the table 4.4., the coefficient of determination ( $R^2$ ) is very close to unity i.e. 0.9940, implying that the ANN model approximated the factor

of safety of the slope close to the actual values with minimum average absolute error of 0.11 for each row as depicted in figure 4.12.

**Table 4.3: Descriptive statistics of the variables used in the development of the model**

	$\alpha$	VWP	C	PWP	$\phi$	FS
<b>Min</b>	9	12.858	15690	-113300	23.986	0.058
<b>Max</b>	84	92.475	27690	-2868	45.145	20.751
<b>Mean</b>	48.84848	59.67507	20385.13	-42856.7	32.073	2.141303
<b>Sd</b>	21.23913	30.49547	10152.2	43755.45	8.045494	2.961379

**Table 4.4: Summary of the number of training and test sets as well as error estimates from the observed data**

Description	Training set	Test set
Number of rows	247	50
CCR	n/a	n/a
Average AE	0.049046	0.0394455
Average MSE	0.0047601	0.0026292
Tolerance type	Relative	Relative
Tolerance	10%	30%
Number of Good forecasts	222 (90%)	50 (100%)
Number of Bad forecasts	25 (10%)	0 (0%)

$R^2: 0.9940$

Correlation: 0.9970

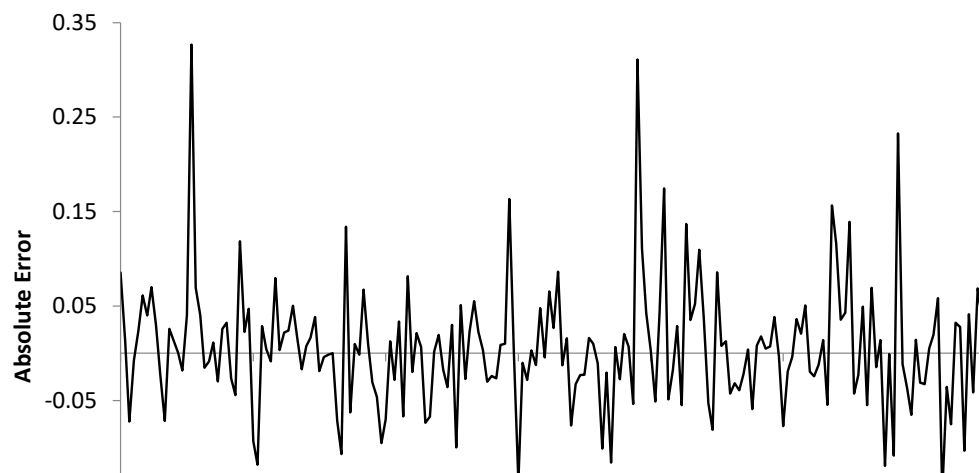


**Figure 4.12: Absolute error between the actual and forecasted values for each row**

Additionally, the trained ANN network was evaluated for its accuracy by comparing the actual observed results to the ANN model results based on the test set using correlation coefficients (appendix II). The comparison between the actual and the ANN model is shown in Figure 4.13 with correlation coefficient of 0.9941. It can be noted from the figure that both the ANN model and actual experimental values have a significantly high correlation coefficient. The data points are aligned closely along the regression line depicting the degree of accuracy of the ANN model.

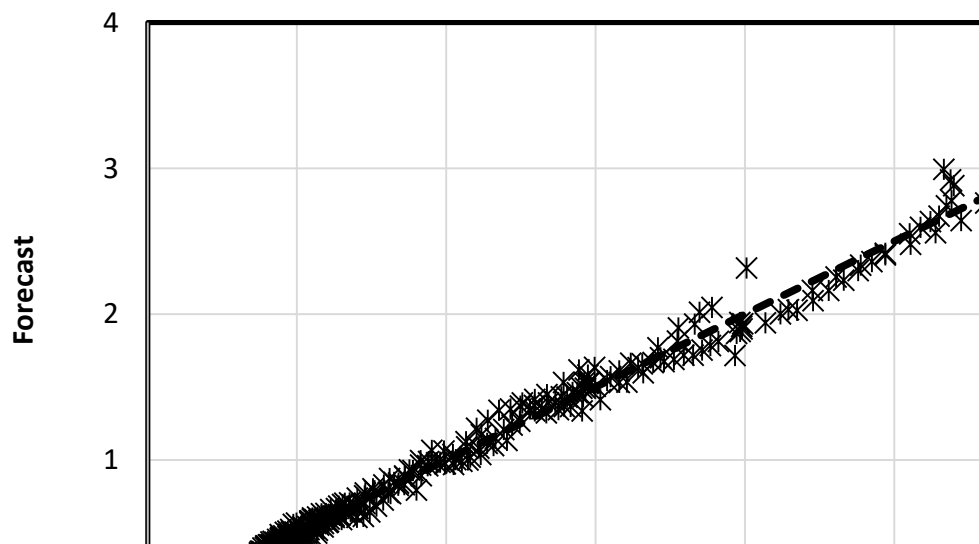


**Figure 4.13: Comparison between actual and forecasted values for the training session**

### **Input importance by percentage to the target**

By employing the commercial software Neuroph<sup>®</sup> and Microsoft Excel<sup>®</sup> embedded program ForecastXL<sup>®</sup>, the trained ANN model was able to establish the contribution of each input to the target output as shown in figure 4.14. In this figure, soil water content has been particularly identified as the most significant contributor to the factor of safety at 54.843% followed by slope angle at 27.979% and pore-water pressure which is a function of moisture content at 14.561%. Soil internal friction angle and cohesive stress (2.264 and 0.353%) are relatively less significant.

From the ANN model results, VWC was identified as the most significant factor influencing FS, in close agreement with other research studies. For instance, Fawaz et al. (2014) carried out numerical simulations and laboratory tests on different soil samples with varying hydrological conditions and concluded that changes in VWC is a proxy to deterioration of mechanical parameters of soil layers constituting the slope. This change in VWC has consequences including outward seepage, development of tension cracks, and eventual slope failure (Jia et al., 2009). Indeed, many other geotechnical investigations based on experimental field tests and numerical models had established the influence of water content variations on the soil shear strength and slope stability (Groh et al., 2020; Bogaard and Greco, 2018; Chueasamat et al., 2018; Brocca et al., 2017), but the percentage of influence was blatantly ignored. Clearly, the degree of significance in terms of a percentage is a vital idea geared towards identifying the triggering factors in terms of their impacts on a given slope, a key step in the development of an early warning system.

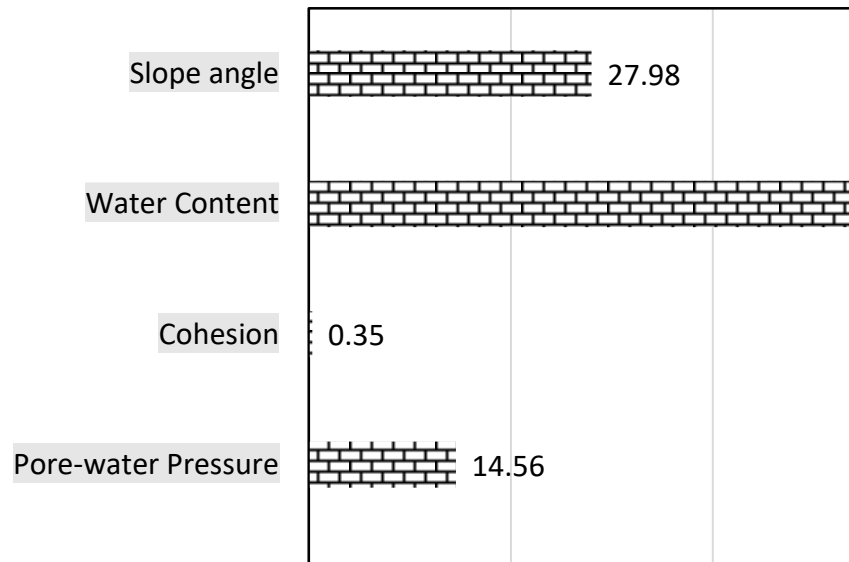


**Figure 4.14: Input importance by percentage to the target**

The second most important factor is PWP. As indicated in earlier sections, increase in pore-water pressure as a result of increased moisture content lowers the magnitude of the effective stress, consequently reducing the available shear strength within the soil mass thereby decreasing slope stability (Zhang et al., 2015). More precisely, for any soil volume that is continuously affected by hydrological conditions, PWP is either influencing or completely governing the actual soil properties (Johansson and Edeskär, 2014). Pore-water pressure variation depends on a number of factors such as the rate of rainfall, the nature of the ground surface, the catchment area, and the soil permeability (Guo, 2020; Wicki et al., 2020). Therefore, by identifying the degree of significance as a percentage to FS by PWP allows researchers and policy makers to ascertain the nature and mechanism of slope failure as well as mitigation measures related to slope instabilities.

The third significant factor is slope angle which obviously causes instability is the slope steepness. The gravitational component of downward force increases proportionately with increase in slope angle even when other factors are held constant

(Chatterjee and Krishna, 2019; Price, 2009), because of self-weight. Additionally, as confirmed by Daer (2001), the inclination angle determines the mode of slope failure, either downslope avalanche or retrogressive type. As such higher inclination angles pose a greater danger to the stability of a slope as witnessed in the reduction of the FS values (Russell et al., 2019; Savage and Hutter, 1991).

Finally, both internal friction angle and soil cohesion are less significant factors in terms of contribution to the FS. This is attributed to the fact that cohesive strength is only effective at low water contents but with higher VWC, PWP dominates. On the other hand, since internal friction angle is a function of the lithological structure of the soil in consideration, its effect will also be minimal and effective only at low VWC (Han et al., 2020; Alonso et al., 2010).

### **Model verification and validation**

Verification and validation are essential processes aimed at assuring that ANN models produced are accurate and produce reliable predictions. The verification stage is aimed at probing if the ANN model was built rightly i.e. if the model was built following the correct procedures, learned the correct data, the type of networks and learning algorithms were appropriate to meet the goals or requirements, etc. On the other hand, validation is concerned with proving if the ANN model built is the right one for the specific purpose i.e. if the ANN model converged to the global minimum or a local minimum, if the model can handle data outside of the training set, and if it can produce acceptable prediction regions (Liu and Yang, 2005; Papadopoulos et al., 2000).

In this study, the last step undertaken was verification and validation of the trained and tested ANN model with a set of geotechnical as well as geophysical input

parameters to evaluate its versatility to physical applications. This was done by using a set of 59 data points (not used both in training and testing) for cross validation with a set of known values of factor of safety. A coefficient of determination was computed and compared with conventionally accepted thresholds. This approach ensures that that results are free of any sample bias and checks for the robustness of the model (<https://medium.com/@salsabilabasalamah/cross-validation-of-an-artificial-neural-network-f72a879ea6d5>, accessed 11/05/2020).

Results of model predictions during validation were plotted against the actual vales of the target (FS) (figure 4.15), gave a positive correlation with the least error. More precisely, the coefficient of correlation obtained between the predicted and validation data set was 0.9933, implying that the ANN model successfully predicted the data.

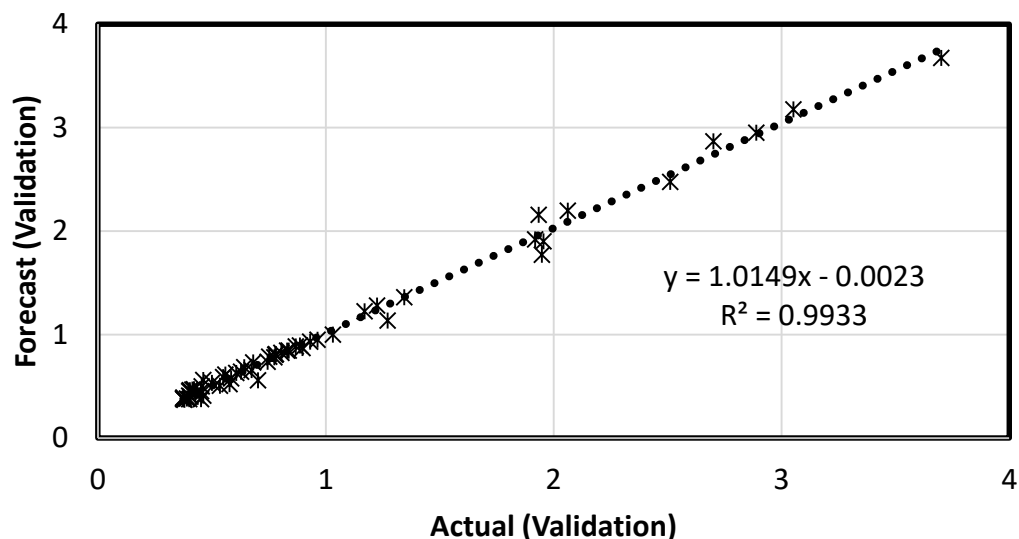


**Figure 4.15: Comparison of actual and predicted factor of safety for validation dataset**

#### 4.2.4.3 Summary, Conclusion and Recommendations

The major objective of study in this section was to develop an intelligent ANN to predict the likelihood of occurrence of slope failure given a set of input parameters.



From descriptive statistics outlined both in text and table 4.4 and figure 4.15, it's clear that the developed ANN was able to predict the state of a given slope by way of a numerical value of the safety factor. As mentioned earlier, a safety factor of greater than unity implies stability of the slope and vice versa. Secondly, from the results especially in figure 4.14, the most significant parameters that contribute to the variations of the safety factor are identified: water content, pore-water pressure, slope angle, internal friction angle and cohesion; arranged in order of decreasing significance.

## CHAPTER FIVE

### CONCLUSIONS AND RECOMMENDATIONS

#### 5.1 Introduction

In this chapter, a highlight of the conclusions drawn from the research outcomes, recommendations and avenues for further research are presented. The first segment provides an exposition of the key findings, conclusions inferred and by extension the contributions to the body of knowledge as well as recommendations. The second section outlines a highlight on the avenues for further research while a brief discussion of the limitations of the proposed scientific methodologies is outlined in the final part.

#### 5.2 Contributions of the study

This study was aimed at undertaking a computational and experimental characterization of convex configuration slopes under varying hydrological conditions. More precisely, it was targeted at deriving physically-based numerical models based on spherical-cap-shaped slope morphology, formulation of a hydromechanical landslide model, design of a versatile real-time monitoring system and development of an adaptive and intelligent ANN model to predict slope instability both in space and time.

As a consequence, a number of physically based numerical models were successfully derived considering spherical-cap shaped slip zones as well as a global hydromechanical landslide equation for analysing soil slopes. Computational results from the models were calibrated against experimental findings based on a Solar Powered Monitoring (SPM) system which comprised of a laboratory flume, sensor array and data broadcasting scheme. Finally, a BP-ANN model was developed and

trained from the experimental data that was utilized for prediction of slope stability status by way of numerical values of the factor of safety. In conclusion, all the proposed objectives of study were fulfilled.

As a result of the findings realized from the study, a number of concluding inferences were drawn which demonstrate originality and advancement of knowledge in soil mechanics as outlined below.

### **5.2.1 Objective 1: Formulation of physically-based numerical and constitutive models to simulate the characteristics of spherical-cap-shaped slip zones**

#### **(i) Slip zone**

The novel formulations presented in this study are based on the consideration of a finite spherical-cap shaped slip zone whose physical dimensions and parameters can be determined experimentally with minimal theoretical assumptions. These models offer a more realistic computational consideration as opposed to existing constitutive models which were based on the assumption that the land mass under failure takes the shape of an ideal cuboid, wedge (in the case of finite and infinite slope) or semi-circular configuration of unit width.

Specifically, it is concluded from the quantitative results that for convex slopes in which the failure surface is planar, the slip zone is approximately equivalent to a spherical cap whose base lies along the incline plane. While, for cohesive soils, the failure surface is curvilinear leading to the more apt and novel concept that the slip zone resembles two spherical caps sharing the base (double spherical caps). Therefore, the overriding conclusion is that the mode of failure and configuration of the slip zone is a function of the volumetric water content, location of the apparent

phreatic surface, magnitude of cohesive strength, orientation of weak planes and existence of discontinuities.

Undoubtedly, it is evident that most voids left after soil mass failures are dome-shaped resembling spherical caps. Therefore, it is recommended that computational constitutive models should incorporate this new consideration of spherical-cap-shaped slip zones as they represent a closer approximation of the natural scenarios as opposed to conventional methods.

### **(ii) Failure plane**

An emergent theme arising from analysis of soil slopes pinpointed the fact that the configuration of the potential failure plane (planar or curved) is dependent on the location of the phreatic surface and discontinuities especially at the interface of stratigraphic layers. Additionally, it can be concluded based on experimental results that for ‘young’ slope profiles arising from past landslide events or weathering processes, for which the interface between the weathered fragments and underlying bedrock do not have a very strong bond, the failure surface is located at the stratigraphic interface and is nearly a straight plane along the slope. While for highly cohesive soils, the failure surface is concave-shaped commencing from locations of discontinuities such as cracks and follows non-linear water flow paths or phreatic surfaces.

These findings are contrary to the conventional assumption that the failure plane always occurs at the soil-bedrock interface. It is recommended that during slope stability analysis, the location and anatomy of the perched or underground water table as well as the cohesive strength, presence of discontinuities and amount of VWC, should be considered before choosing the profile and location of the failure surface.

### **5.2.2 Objective 2: Hydromechanical Landslide Model**

Amongst the original contributions advanced in this study lies in the fact that geotechnical, geophysical and hydrological parameters are defined as empirical functions of the volumetric water content. The unique computational descriptions include expression of the cohesive stress, pore-water pressure and factor of safety as empirical functions of volumetric water content as well as representation of pulsed rainfall event as a Fourier transform.

A novel hydromechanical landslide model for the factor of safety of a soil mass on a slope was derived incorporating the volumetric water content as the most significant variable in its formulation. The more expedient hydromechanical model for the FS conceives a remedy to many geotechnical scientists because of its simplicity in terms of computation and application as it is dependent on only two variables i.e. volumetric water content and slope angle to establish the stability status of a given slope.

More pertinently the soil cohesive stress is defined as an empirical function of the volumetric water content, as such expensive and complex triaxial tests are excluded. In principle, the number of transducers and sensors are greatly reduced without compromising the integrity of computation and system instrumentation. Moreover, an improved effective wetness index has been derived taking into consideration the moist soil unit weight, as opposed to earlier models which were based on purely dry soil or saturated conditions.

Finally, since the threshold VWC for slope failure can be extracted directly from the equation of the FS, it is concluded that an early warning system can be developed based on this data for purposes of prediction and disaster preparedness. Essentially, it is noteworthy to conclude that since the FS in this model is principally a function of the VWC, it is recommended that an early warning system based purely on VWC

would be a remedy to many geophysical and geotechnical professionals in design and implementation.

Based on comparison between the experimental results and the computational data, it can be concluded that there was close concurrence between the models and experiments with  $r^2 > 0.9$  in all trials. It is therefore recommended that, since the models advanced in this study are physics-based, they can be applied on a variety of rainfall induced shallow landslides on relatively steep slopes. In other words, the field data can be readily incorporated into the hydromechanical slope stability model as well as the BP-ANN model to predict the stability status of a given slope.

### **5.2.3 Objective 3: SPM system architecture**

A hybrid SPM system comprising of both optical and electronic sensors for collection and transmission of data to a dedicated server for processing was developed and implemented. The SPM system architecture offers a significant advancement to the existing data acquisition designs because of minimal power consumption (and also powered by solar electric energy) and versatility, as well as relatively smaller number of transducers and sensors. Since this system can transmit processed data wirelessly, it can be integrated into an early warning system for disaster mitigation.

### **5.2.4 Objective 4: ANN model**

In this study, a unique BP-FF ANN model embedded in MS Excel™ was developed to predict numerical values of the factor of safety of a slope when fed with both geophysical and geotechnical as well as hydrological parameters. Statistical comparison of the ANN model results and experimental data indicated an overall relative error of less than 5%, leading to the conclusion that ANN models can provide

an effective solution to the evaluation of slope stability and by extension development of early warning systems.

Furthermore, the contribution to new knowledge that this study makes is the identification of the parametric input importance to the FS. For instance, results from ANN rubrics pinpointed VWC as the most significant factor modulating the FS followed by PWP, slope angle, internal friction angle and cohesion respectively. Since VWC is identified as the most significant proxy to deformation-softening process in slopes, and recognizing that most geophysical and geotechnical parameters are empirical functions of VWC, it is recommended that efficient drainage mechanisms and continuous monitoring of VWC in sloping regions will provide appropriate mitigation interventions to slope instability cases.

### **5.3 Recommendations for Further Research**

In this study, a number of numerical models were proposed and tested against experimental data using an SPM system based on a laboratory flume, yielding a number of research outputs. However, a number of recommendations for further research work are proposed, namely:

- i) Slope stability analysis using a combination of ANN and fuzzy logic models;
- ii) Explore other methodologies of analyzing complex configuration slip zones, and
- iii) Apply rheological and smoothed particle models to convex configuration slopes

### **5.4 Limitations of the study**

Characterization of soil slopes is a key initiative aimed at expanding the knowledge base with regard to disasters arising from mass wasting events. However, the experimental scope of study is too wide. For this reason, only representative samples

were considered and therefore the analysis could not be exclusively generalized without statistical assumptions. Additionally, because of the limitation to field-based equipment as a result of budgetary constraints, experimental trials were undertaken in a laboratory setting using a flume.

Furthermore, the physically based models derived in this study are a result of laboratory simulation processes which mimic *in situ* field conditions, although limitations cannot be ignored especially with regard to basal friction, soil-bedrock interface conditions and pore-water fluctuations at different locations. Moreover, the simulation efforts pursued in this study were able to yield the global factor of safety (i.e. for the whole soil mass in question), but local FS values could not be determined because of limitation in the number of transducers.

### **5.5 Concluding remarks**

The significance of the results of this study especially from the proposed numerical models and ANN formulation cannot be underestimated as they are of great utility to geophysical and geotechnical scientists, physical planners and the community at large. In essence, the models and experimental results as well as the deductions derived from this study will aid in providing baseline geophysical and geotechnical information as well as hydrological considerations to the public, government agencies and non-governmental organizations, on the stability of soil slopes. Secondly, the derived models based on spherical-cap shaped slip zones as well as the hydromechanical slope stability model will form the basis for more precise constitutive computations with regard to soil slopes. Lastly, prediction of slope stability status by way of a BP-FF ANN model will provide an excellent approach of



developing an early warning system for disaster preparedness. Therefore, all the four objectives of study were addressed.

## REFERENCES

- Abadie S., Morichon D., Grilli S. and Glockner S. (2010). Numerical simulation of waves generated by landslides using a multiple-fluid Navier-Stokes model. *Coastal Engineering*, **57**:779-794.
- Abraham M. T., Satyam N., Pradhan B. and Alamri A. M. (2020). Forecasting of Landslides Using Rainfall Severity and Soil Wetness: A Probabilistic Approach for Darjeeling Himalayas. *Water*, **12**:804.
- Abramson L., Lee T., Sharma S. and Boyce G. (2002). *Slope Stability and Stabilization Methods*, John Wiley & Sons, Inc., New York.
- Abu-Kiefa M. A. (1998). General regression neural networks for driven piles in cohesionless soils, *Journal of Geotechnical and Geoenvironmental Engineering*, ASCE, **124**(12):1177-1185.
- Adams M. J. and Perchard V. (1997). The cohesive forces between particles with interstitial fluid, *Physical Review E*, **56**(4):4467-4473.
- Aldefae A. H., Alkhafaji R. A., Shamkhi M. S. and Kumer H. Q. [Iervolino M. - Reviewing editor] (2019). Design and manufacturing of flume apparatus to investigate the failure mechanism of riverbanks, *Cogent Engineering*, **6**(1).
- Alonso E. E., Pereira J. M., Vaunat J. and Olivella S. (2010). A microstructurally based effective stress for unsaturated soils, *Geotechnique*, **60**:913–925.
- Adeli H. (2001). Neural networks in civil engineering: 1989-2000, *Computer-Aided Civil and Infrastructure Engineering*, **16**(2):126-142.
- Adeli H. and Wu M. (1998). Regularization neural network for construction cost estimation, *Journal of Construction Engineering and Management*, ASCE, **124**(1):18-24.

- Aharonov E. and Scholz C. H. (2018). A physics-based rock friction constitutive law: steady state friction, *Journal of Geophysical Research: Solid Earth*, **123**(2):1591-1614.
- Alaniz A., Barahona-Segovia R., Nuñez-Hidalgo I., González-Céspedes C., Osorio J., Hora B., Marchant C., Gutierrez-Gómez C., Arias R., Toro P., Escobar-Bahamondes P., Huerta J., Martinez C., Vicuña M., Guerrero N., Orellana V., Tapia J., Rodríguez M., Castillo P. and Fuentes G. (2019). *Chile: Environmental History, Perspectives and Challenges*, (1<sup>st</sup> Ed.), NOVA Science Publishers Inc.
- Alavi N., Tugrul A., Gokceoglu C. and Armaghani D. (2016). Characteristics of weathering zones of granitic rocks in *Malaysia for geotechnical engineering design*, *Engineering Geology*, **200**:94-103.
- Alemdağ S., Kaya A., Karadağ M., Gürocak Z. and Bulut F. (2015). Utilization of the limit equilibrium and finite element methods for the stability analysis of the slope debris: An example of the Kalebaşı District (NE Turkey); *Journal of African Earth Sciences*, **106**:134-146.
- Alvioli M., Marchesini I., Reichenbach P., Rossi M., Ardizzone F., Fiorucci F. and Guzzetti F. (2016). Automatic delineation of geomorphological slope units with r.slopeunits v1.0 and their optimization for landslide susceptibility modelling. *Geoscientific Model Development*, **9**:3975-3991.
- Anderson J. (1995). *An Introduction to Neural Networks*, A Bradford Book, MIT Press, Cambridge, MA.
- Anderson M. and Holcombe E. (2013). *Community-Based Landslide Risk Reduction: Managing Disasters in Small Steps*, World Bank Publications.

- Anglo Coal and Reutech Radar Systems (2005). *Brochure on Movement and Surveying Radar—An Overview*, www.rrs.co.za, accessed 10/01/2020.
- Arora K. (2008). *Soil mechanics and foundation engineering (geotechnical engineering)*, 8<sup>th</sup> ed., Lomus Ofset Press, Delhi, 953.
- ASCE Task Committee on Application of Artificial Neural Networks in Hydrology (2000a). Artificial neural networks in hydrology. I: pre-liminary concepts, *Journal of Hydrologic Engineering, ASCE*, **5**(2):115-123.
- ASCE Task Committee on Application of Artificial Neural Networks in Hydrology (2000b). Artificial neural networks in hydrology. II: hydrologic applications, *Journal of Hydrologic Engineering, ASCE, ASCE*, **5**(2):124–137.
- ASD-Network (2006). *Radar Satellite Service checks stability of Africa's largest artificial hole*. www.asd-network.com, accessed 10/01/2020.
- Askarinejad A., Bischof P., Beck A., Casini F. and Springman S. (2012). Rainfall induced instabilities: a field experiment on a silty sand slope in Northern Switzerland. *RIG, Italian Geotechnical Journal*, **3**:50-71.
- Assouline S. and Or D. (2014). The concept of field capacity revisited: Defining intrinsic static and dynamic criteria for soil internal drainage dynamics, *Water Resources Research*, **50**, 4787– 4802.
- Ataie-Ashtiani B. and Jilani A. (2007). A higher-order Boussinesq-type model with moving bottom boundary: applications to submarine landslide tsunami waves. *International Journal for Numerical Methods in Fluids*, **53**:1019-1048.
- Baartman J., Temme A. and Saco P. (2018). The effect of landform variation on vegetation patterning and related sediment dynamics, *Earth Surface Processes and Landforms*, **43**:2121-2135.

- Baba K., Bahi L, Ouadif L. and Akhhsas A. (2012). Slope stability evaluations by limit equilibrium and finite element methods applied to a railway in the Moroccan Rif. *Open Journal of Civil Engineering*, **2**:27-32.
- Bahareh K., Biswajeet P., Seyed A., Alireza M. and Shattri M. (2018). Assessment of the effects of training data selection on the landslide susceptibility mapping: a comparison between support vector machine (SVM), logistic regression (LR) and artificial neural networks (ANN), *Geomatics, Natural Hazards and Risk*, **9**(1):49-69.
- Baharuddin I., Omar R., Roslan R, Khalid N. and Hanifah M. (2016). Determination of Slope Instability Using Spatially Integrated Mapping Framework, *IOP Conference Series: Materials Science and Engineering*, **160**:012080.
- Basahel H. and Mitri H. (2017). Application of rock mass classification systems to rock slope stability assessment: a case study, *Journal of Rock Mechanics and Geotechnical Engineering*, **9**(6):993-1009.
- Begat P., Morton D. A., Staniforth J. N. and Price R. (2004). The Cohesive-Adhesive Balances in Dry Powder Inhaler Formulations I: Direct Quantification Force Microscopy. *Pharmaceutical Research*, **21**(9):1591-1597.
- Behrens T. Schmidt K., Ramirez-Lopez L., Gallant J., Zhu A-X. and Scholten T. (2014). Hyper-scale digital soil mapping and soil formation analysis, *Geoderma*, **213**:578-588.
- Bièvre G., Jongmans D., Winiarski T. and Zumbo V. (2012). Application of geophysical measurements for assessing the role of fissures in water infiltration within a clay landslide (Trièves area, French Alps). *Hydrological Processes*, **26**(14):2128-2142.

- Bishop A. (1955). The use of the slip circle in the stability analysis of earth slopes. *Geotechnique*, **5**(1):7-17.
- Bishop A. (1967). Progressive failure—with special reference to the mechanism causing it. *Proceedings of the Geotechnical Conference on Shear Strength Properties of Natural Soils and Rocks, Oslo* **2**:142-150.
- Bocco M., Willington E. and Arias M. (2010). Comparison of regression and neural networks models to estimate solar radiation. *Chilean Journal of Agricultural Research*, **70**(3):428-435.
- Bodner G., Scholl P., Loiskandl W. and Kaul H. (2013). Geoderma Environmental and management influences on temporal variability of near saturated soil hydraulic properties. *Geoderma*, **204–205**:120–129.
- Bogaard T. and Greco R. (2018). Invited perspectives: hydrological perspectives on precipitation intensity-duration thresholds for landslide initiation: proposing hydro-meteorological thresholds. *Natural Hazards and Earth System Sciences*, **18**:31–39.
- Bordoni M. Meisina C. Valentino R. Lu N. Bittelli M. and Chersich S. (2015). Hydrological factors affecting rainfall-induced shallow landslides: from the field monitoring to a simplified slope stability analysis, *Engineering Geology*, **193**:19-37.
- Bouissou S., Darnault R., Chemenda A. and Rolland Y. (2012). Evolution of gravity-driven rock slope failure and associated fracturing: geological analysis and numerical modelling, *Tectonophysics*, **526–529**:157–166.
- Brady B. and Brown E. (2004) *Rock mechanics for underground mining*. Kluwer, Dordrecht, 159.

- Brakorenko N., Leonova A. and Nikitenkov A. (2019). Effect of soil water saturation on slope stability: Tomsk case study, *E3S Web of Conferences* 98, 05005.
- Briggs L. J. (2016). *The Mechanics of Soil Moisture Paperback*, Wentworth Press, 38.
- Brocca L., Ciabatta L., Massari C., Camici S. and Tarpanelli A. (2017). Soil moisture for hydrological applications: Open questions and new opportunities. *Water*, **9**:140.
- Brown M. and Harris C. (1994). *Neurofuzzy adaptive modelling and control*, Prentice-Hall, Englewood Cliffs, New Jersey.
- Caner M., Gedik, E. and Kecebas A. (2011). Investigation on thermal performance calculation of two type solar air collectors using artificial neural network. *Expert Systems with Applications*, **38**:1668-1674.
- Carbune V., Gonnet P., Deselaers T., Rowley H. A., Daryin A., Calvo M., Wang L., Keysers D., Feuz S. and Gervais P. (2020). Fast multi-language LSTM-based online handwriting recognition, *International Journal on Document Analysis and Recognition*, **23**:89–102.
- Carey J. M., Massey C. I., Lyndsell B. and Petley D. N. (2019). Displacement mechanisms of slow-moving landslides in response to changes in porewater pressure and dynamic stress, *Earth Surface Dynamics*, **7**:707–722.
- Carro M., De Amicis M., Luzi L., and Marzorati S. (2003). The application of predictive modeling techniques to landslides induced by earthquakes: the case study of the 26 September 1997 Umbria-Marche earthquake (Italy). *Engineering Geology*, **69**(1-2):139-159.
- Casadei M., Dietrich W. and Miller N. (2003). Testing a model for predicting the timing and location of shallow landslide initiation in soil-mantled landscapes. *Earth Surface Processes and Landforms*, **28**:925-950.

- Cascini L., Cuomo S. and Pastor M. (2013). Geomechanical modelling of debris avalanches inception. *Landslides*, **10**(6):701–711.
- Cecioni C. and Bellotti G. (2010). Modelling tsunamis generated by submerged landslides using depth integrated equations. *Applied Ocean Research*, **32**(3):343-350.
- Chae B.-G., Lee J.-H., Park H.-J., and Choi J. (2015). A method for predicting the factor of safety of an infinite slope based on the depth ratio of the wetting front induced by rainfall infiltration, *Natural Hazards and Earth System Sciences*, **15**:1835–1849.
- Chakraborty A. and Goswami D. (2017). Slope Stability Prediction using Artificial Neural Network (ANN), *International Journal of Engineering and Computer Science*, **6**(6):21845-21848.
- Chambers J., Wilkinson P., Kuras O., Ford J., Gunn D., Meldrum P., Pennington C., Weller A., Hobbs P. and Ogilvy R. (2011). Three-dimensional geophysical anatomy of an active landslide in Lias group mudrocks, Cleveland Basin, UK. *Geomorphology*, **125**(4):472-484.
- Chao Z. and Ning L. (2019). Unitary Definition of Matric Suction, *Journal of Geotechnical and Geoenvironmental Engineering*, **145**(2):02818004.
- Charles J. A. and Soares M. M. (1984). The stability of slopes in soils with nonlinear failure envelopes. *Canadian Geotechnical Journal*, **21**(3):397–406.
- Chatterjee D. and Krishna M. A. (2019). Effect of Slope Angle on the Stability of a Slope Under Rainfall Infiltration, *Indian Geotechnical Journal*, **49**:708-717.
- Chekalin A., Khramchenkov M., Konyukhov V., Konyukhov I. and Garaeva A. (2017). Mathematical modelling of rainwater runoff over catchment surface



and mass transfer of contaminant incoming to water stream from soil. *Journal of Fundamental and Applied Sciences*, **9**(2S):880-889.

Chen F. (2000). *Soil Engineering: Testing, Design, and Remediation*. CRC Press: Boca Raton, FL.

Chen H. and Zhang L. (2014). A physically-based distributed cell model for predicting regional rainfall-induced slope failures. *Engineering Geology*, **176**:79-92.

Chen Y., Lin Y., Kung C., Chung M. and Yen I. (2019). Design and Implementation of Cloud Analytics-Assisted Smart Power Meters Considering Advanced Artificial Intelligence as Edge Analytics in Demand-Side Management for Smart Homes. *Sensors*, **19**(9):2047.

Chou T. K. (2016). A free GUI application for solving the van Genuchten parameters using non-linear least-squares minimization and curve-fitting, *www.cmcsjc.com*. January: 1-5.

Chueasamat A., Hori T., Saito H., Sato T. and Kohgo Y. (2018). Experimental tests of slope failure due to rainfalls using 1g physical slope models, *Soils and Foundations*, **58**:290-305.

Chugh A. (2002). A method for locating critical slip surfaces in slope stability analysis: Discussion. *Canadian Geotechnical Journal*, **39**(3):765-770.

Clare M., Chaytor J., Dabson O., Gamboa D., Georgiopoulou A., Eady H., Hunt J., Jackson C., Katz O., Krastel S., León R., Micallef A., Moernaut J., Moriconi R., Moscardelli L., Mueller C., Normandeau A., Patacci M., Steventon M., Urlaub M., Völker D., Wood L. and Jobe Z. (2018). A consistent global approach for the morphometric characterization of

- subaqueous landslides, *Geological Society, London, Special Publications*, **477**:455-477.
- Coduto D., Yeung M. and Kitch W. (2011). *Geotechnical Engineering Principles and Practices*. NJ: Pearson Higher Education, Inc.
- Conte E., Pugliese L., Troncone A. (2020) Run-Out of Landslides Caused by Excess Pore Water Pressure Along the Slip Surface, In: Calvetti F., Cotecchia F., Galli A., Jommi C. (eds) *Geotechnical Research for Land Protection and Development, CNRIG 2019. Lecture Notes in Civil Engineering*, **40**, Springer, Cham.
- Conte E., Donato A. and Troncone A. (2017). A simplified method for predicting rainfall-induced mobility of active landslides. *Landslides*, **14**:35-45.
- Crozier M. J. (1986). *Landslides - Causes, Consequences and Environment*. Croom Helm, London.
- Cruden D. and Varnes D. (1996). *Landslide Types and Processes*, Transportation Research Board, *U.S. National Academy of Sciences, Special Report*, **247**:36-75.
- Cybenko G. (1989). Approximations by superpositions of sigmoidal functions, *Mathematics of Control, Signals, and Systems*, **2**(4):303-314.
- Daer A. (2001). Dynamical equilibrium of avalanches on a rough plane, *Physics of Fluids*, **13**(7):2115–2124.
- Dai K, Li Z., Tomás R., Liu G., Yu B., Wang X., Cheng H., Chen J. and Stockamp, J. (2016). Monitoring activity at the Daguangbao mega-landslide (China) using Sentinel-1 TOPS time series interferometry. *Remote Sensing of Environment*, **186**:501-513.

- Damiano E. and Olivares L. (2010). The role of infiltration processes in steep slopes stability of pyroclastic granular soils: laboratory and numerical investigation, *Nat. Hazards*, **52**(2):329–350.
- Damiano E., Greco R., Guida A., Olivares L. and Picarelli L. (2017). Investigation on rainwater infiltration into layered shallow covers in pyroclastic soils and its effect on slope stability, *Engineering Geology*, **220**:208–218.
- Das B. (2011). *Principles of Foundation Engineering*. Stamford, CT: Cengage Learning.
- Davidová T., Dostál T., David V. and Strauss P. (2015). Determining the protective effect of agricultural crops on the soil erosion process using a field rainfall simulator. *Plant Soil Environment*, **1**:109-115.
- De Vleeschauwer C. and De Smedt F. (2002). Modeling slope stability using GIS on a regional scale. *Proceedings of the first Geological Belgica International Meeting*, Leuven, Aardkundige Mededelingen **12**:253-256.
- Deschamps R. and Leonards G. (1992). A study of slope stability analysis. *ASCE Specialty Conference on Stability and Performance of Slopes and Embankments II*, San Francisco, **1**:267-291.
- Díaz E., Robles P., and Tomás R. (2018). Multitechnical approach for damage assessment and reinforcement of buildings located on subsiding areas: Study case of a 7-story RC building in Murcia (SE Spain). *Engineering Structures*, **173**:744-757.
- Ding X., Montgomery S., Tsakiri M., Swindells C. and Jewell R. (1998). *Integrated monitoring systems for open pit wall deformation*, Meriwa Project No. M236, Meriwa Report No. 186.

- Duncan J. (1996) State of the Art: Limit Equilibrium and Finite-Element Analysis of Slopes. *Journal of Geotechnical Engineering*, **122**:577-596.
- Duncan J. M. and Wright S. G. (2005). *Soil strength and slope stability*. John Wiley & Sons, Inc., Upper Saddle River, N. J. New York.
- Dunnicliff J. (1993). *Geotechnical Instrumentation for Monitoring Field Performance*. New York: John Wiley and Sons.
- Dussauge-Peisser C., Helmstetter A. and Grasso J-R., Hantz D., Desvarreaux P., Jeannin M. and Giraud A. (2002). Probabilistic approach to rock fall hazard assessment: potential of historical data analysis. *Natural Hazards and Earth System Sciences*, **2**:15-26.
- EI-Ramly H., Morgenstern N. and Cruden D. (2002). Probabilistic slope stability analysis for practice. *Canadian Geotechnical Journal*, **39**(3):665-683.
- ELFEN (2001). *ELFEN 2D/3D Numerical Modelling Package*. Rockfield Software Ltd.: Swansea.
- Ellis G., Yao C., Zhao R. and Penumadu D. (1995). Stress-strain modeling of sands using artificial neural networks, *Journal of Geotechnical Engineering, ASCE*, **121**(5):429-435.
- Ercanoglu M. and Gokceoglu C. (2002). Assessment of landslide susceptibility for a landslide prone area (North of Ynice, NW Turkey) by fuzzy approach. *Environmental Geology*, **41**:720-730.
- Fang H., Cui P., Pei L. and Zhou X. (2012). Model testing on rainfall-induced landslide of loose soil in Wenchuan earthquake region. *Natural Hazard and Earth System Sciences*, 527-533.
- Fawaz A., Farah E. and Hagechegade F. (2014). Slope Stability Analysis Using Numerical Modelling, *American Journal of Civil Engineers*, **2**(3):60-67.

- Fayne J., Ahamed A., Roberts-Pierel J., Rumsey A. and Kirschbaum D. (2019). Automated Satellite-Based Landslide Identification Product for Nepal. *Earth Interactions*, **23**:1-21.
- Fellenius W. (1936). *Calculation of the Stability of Earth Dams*. Trans. 2<sup>nd</sup> Int. Cong. Large Dams, Washington, 445-459.
- Fredlund D. G. and Rahardjo H. (1993). *Soil mechanics for unsaturated soils*. New York, NY: John Wiley & Sons.
- Fredlund D. and Xing A. (1994). Equations for the soil–water characteristic curve, *Canadian Geotechnical Journal*, **31**(3):521-532.
- Fredlund D., Morgenstern N. and Widger A. (1978). Shear strength of unsaturated soils. *Canadian Geotechnical Journal*, **15**:313–321.
- Fredlund D., Rahardjo H. and Fredlund M. (2014). *Unsaturated Soil Mechanics in Engineering Practice*. Wiley-Interscience.
- Friele P., Millard T. H., Mitchell A., Allstadt K. E., Menounos B., Geertsema M. and Clague J. J. (2020). Observations on the May 2019 Joffre Peak landslides, British Columbia. *Landslides*, **17**:913–930.
- Froude M. and Petley D. (2018). Global fatal landslide occurrence from 2004 to 2016. *Natural Hazards and Earth System Sciences*, **8**:2161-2181.
- Fuhrman D. and P. Madsen (2009). Tsunami generation, propagation, and run-up with a high-order Boussinesq model. *Coastal Engineering*, **56**:747-758.
- Gabiri G., Burghof S., Diekkrüger B., Leemhuis C., Steinbach S. and Näschen K. (2018). Modeling spatial soil water dynamics in a tropical floodplain, East Africa. *Water*, **10**:191.
- Gachene C. and Kimaru G. (2003). *Soil Fertility and Land Productivity - A guide for extension workers in the eastern Africa region*. Technical Handbook No.30.

Regional Land Management Unit (RELMA)/ Swedish International Development Cooperation Agency (Sida).

- Galavi V. and Schweiger H. F. (2010). Nonlocal multilaminate model for strain softening analysis, *International Journal of Geomechanics*, **10**(1):30–44.
- Gandhi P., Werner L., Iams S., Gowda K. and Silber M. (2018). A topographic mechanism for arcing of dryland vegetation bands, *Journal of the Royal Society Interface*, **15**(147):20180508.
- Geist E. L., Lynett P. J. and Chaytor J. D. (2009). Hydrodynamic modeling of tsunamis from the Currituck landslide. *Marine Geology*, **264**:41-52.
- Geotechnics [www.halcrow.com/geotechnics](http://www.halcrow.com/geotechnics), accessed 15/12/2008)
- Göktürkler G., Balkaya Ç. and Erhan Z. (2008). Geophysical investigation of a landslide: The Altındağ landslide site, İzmir (western Turkey). *Journal of Applied Geophysics*, **65**(2):84-96.
- Golovin D., Solnik B., Moitra S., Kochanski G., Karro J. and Sculley D. (2017). Google vizier: A service for black-box optimization, Proceedings of the 23rd ACM SIGKDD International Conference on Knowledge Discovery and Data Mining, 1487–1495.
- Gray D. (2013). Influence of Slope Morphology on the Stability of Earthen Slopes. *Geotechnical Special Publication*. 1895-1904.
- Gribb M. M., Forkutsa I., Hansen A., David G. and Chandler J. P. M. (2009). The Effect of Various Soil Hydraulic Property Estimates on Soil Moisture Simulations, *Vadose Zone J.*, **8**:321–331.
- Griffiths D., Huang J. and Fenton G. (2009). Influence of spatial variability on slope reliability using 2-D random fields. *Journal of Geotechnical and Geoenvironmental Engineering*, **135**(10):1367-1378.

- Griffiths D. and Lane P. (1999). Slope stability analysis by finite elements  
*Géotechnique*, **49**(3):387-403.
- Griffiths D. and Fenton G. (2004). Probabilistic Slope Stability Analysis by Finite Elements, *Journal of Geotechnical and Geoenvironmental Engineering*, 130(5).
- Grilli S., Dias F., Guyenne P., Fochesato C. and Enet F. (2010). Progress in Fully Nonlinear Potential Flow Modelling of 3D Extreme Ocean Waves, in *Series in Advances in Coastal and Ocean Engineering*, World Scientific Publishing Co. Pte. Ltd., 75-128.
- Groh J., Vanderborght J., Pütz T., Vogel H.-J., Gründling R., Rupp H., Rahmati M., Sommer M., Vereecken, H. and Gerke H. H. (2020). Responses of soil water storage and crop water use efficiency to changing climatic conditions: a lysimeter-based space-for-time approach, *Hydrology and earth system sciences*, **24**:1211–1225.
- Groundprobe Brochure (2005). Slope Stability Radar, [www.groundprobe.com](http://www.groundprobe.com), accessed 10/01/2020.
- Guo Z. (2020). Estimating Method of Maximum Infiltration Depth and Soil Water Supply. *Scientific Reports*, **10**:9726.
- Gutiérrez-Martín A., Herrada M. Á., Yenes J. I., and Castedo R. (2019). Development and validation of the terrain stability model for assessing landslide instability during heavy rain infiltration, *Natural Hazards and Earth System Sciences*, **19**:721–736.
- Guzzetti F., Ardizzone F., Cardinali M., Rossi M. and Valigi D. (2009). Landslide volumes and landslide mobilization rates in Umbria, central Italy. *Earth and Planetary Science Letters*, **279**(3-4):222-229.

- Halty I. A. J. (2014). *Stability, Erosion, and Morphology Considerations for Sustainable Slope Design*, Ph.D. Thesis, University of Tennessee-Knoxville.
- Han Z., Li J., Gao P., Huang B., Ni J. and Wei C. (2020). Determining the Shear Strength and Permeability of Soils for Engineering of New Paddy Field Construction in a Hilly Mountainous Region of Southwestern China, *International Journal of Environmental Research and Public Health*, **17**(5), 1555.
- Hastie T., Tibshirani R. and Friedman J. (2001). *The Elements of Statistical Learning*, Springer-Verlag, New York.
- Hazari S., Roy S. and Ghosh S. (2019). *Analysis of Slope Considering Non-Linear Failure Surface*, Conference: ICERME-2019, At NIT Agartala.
- Hecht-Nielsen R. (1990) *Neurocomputing*, Addison-Wesley Publishing Company, Reading, Massachusetts.
- Herminghaus S. (2005). Dynamics of wet granular matter, *Advances in Physics*, **54**(3): 221-6.
- Highland L. and Bobrowsky P. (2008). *The landslide handbook: a guide to understanding landslides*, US Geol. Survey, Reston, 129.
- Hill D. J. and Minsker B. S. (2010). Anomaly detection in streaming environmental sensor data: a data-driven modelling approach, *Environmental Modelling and Software*, **25**:1014-1022.
- <http://pubs.usgs.gov/fs/2004/3072>, accessed 24/10/2019.
- <http://pubs.usgs.gov/fs/2004/3072/pdf/fs2004-3072.pdf>, accessed 21/03/2020.
- <http://www.soilmanagementindia.com/soil/slope-stability/stability-of-earth-slopes-soil-engineering/14489>, accessed 04/04/2020.



<http://environment.uwe.ac.uk/geocal/SoilMech/water/water.htm>, accessed 04/07/2020.

<https://www.aa.com.tr/en/environment/environmental-disasters-across-world-in-june-2020/1895500>, accessed 30/07/2020

<https://citizentv.co.ke/news/photos-west-pokot-landslide-the-aftermath-305535/>, accessed 14/01/2020.

[https://en.wikipedia.org/wiki/Mass\\_wasting](https://en.wikipedia.org/wiki/Mass_wasting), accessed 24/10/2019.

<https://medium.com/@salsabilabasalamah/cross-validation-of-an-artificial-neural-network-f72a879ea6d5>, accessed 11/05/2020.

<https://sciencing.com/topography-deserts-8178249.html>, accessed, 30/06/2020

<https://study.com/academy/lesson/scientific-models-definition-examples.html>, accessed 11/03/2020.

<https://theconstructor.org/geotechnical/slope-failures-types/28467/>, accessed 04/04/2020.

<https://www.nation.co.ke/counties/elgeyo-marakwet/Four-killed-in-Marakwet-landslide/3444818-5316280-15446p9z/index.html>, accessed 20/10/2019.

<https://www.nation.co.ke/news/1056-201434-1vds5gz/index.html>, accessed 15/04/2020.

Huang X., Shi Z. H., Zhu H. D., Zhang H. Y., Ai L. and Yin W. (2016). Soil moisture dynamics within soil profiles and associated environmental controls. *Catena*, **136**:189–196.

Huang Y. H. (2014). *Slope Stability Analysis by the Limit Equilibrium Method: Fundamentals and Methods*, ASCE Press.

Huddleston A. (1951). Geology of Kakamega area. *Geological survey of Kenya*. Report No.28.

- Humboldt County Operational Area Hazard Mitigation Plan (2019). Volume 1-Area-Wide Elements, Tetra Tech Project #103S5974.
- Hungr O., Leroueil S. and Picarelli L. (2014). The Varnes classification of landslide types, an update, *Landslides*, **11**:167-194.
- Hutchinson J. (1988). General report: Morphological and geo-technical parameters of landslides in relation to geology and hydrology, in Bonnard C. (Ed.), *Proceedings, Fifth International Symposium on Landslides*, A. A. Balkema, Rotterdam, **1**:3-36.
- Ishak M. and Zolkepli M. (2016). Exploration of Method for Slope Stabilization Influenced by Unsaturated Soil, *Electronic Journal of Geotechnical Engineering*, (21.17), 5627-5641.
- Iveson S. M., Litster J. D., Hapgood K. and Ennis B. J. (2001). Nucleation, growth and breakage phenomena in agitated wet granulation processes: a review, *Powder Technology*, **117**:3
- Jakob M. (2000). The impacts of logging on landslide activity at Clayoquot Sound, British Columbia. *Catena*, **38**:279-300.
- Janbu N. (1973), Hirschfeld R. C. and Poulos S. J. (eds.), Slope stability computations, *In Embankment-dam Engineering*, Jon Wiley and Sons Inc., NY: 40P.
- Jeffreys S. (2004). *The Role of GPS in an Open Pit Slope Stability Monitoring Programme*, Project report for Slope Stability Monitoring Certificate, University of the Witwatersrand, Johannesburg.
- Jenkins W. (1999). A neural network for structural re-analysis, *Computers and Structures*, **72**:687-98.

- Jia G., Zhan T., Chen Y. and Fredlund D. (2009). Performance of a largescale slope model subjected to rising and lowering water levels. *Engineering Geology*, **106**(1-2):92-103.
- Johansson J., and Edeskär T. (2014). Effects of external water-level fluctuations on slope stability, *Electronic Journal of Geotechnical Engineering*, **19**:2437-2463.
- Johnson R. B. and Degraff J. V. (1991). *Principles of Engineering Geology*, John Willy and Sons, New York.
- Kaab A. (2002). Monitoring high-mountain terrain deformation from repeated air- and spaceborne optical data: Examples using digital aerial imagery and ASTER data. *Journal of Photogrammetry and Remote Sensing*, **57**:39-52.
- Kievitsbosch R., Smit H., Magnanimo V., Luding S. and Taghizadeh K. (2017). Influence of dry cohesion on the micro- and macro-mechanical properties of dense polydisperse powders & grains, *EPJ Web of Conferences*, 140:08016.
- Kilburn C. and Petley D. (2003). Forecasting giant, catastrophic slope collapse: lessons from Vajont, Northern Italy. *Geomorphology*, **54**(1-2):21-32.
- Kimiaghalam N., Clark S. P. and Ahmari H. (2016). An experimental study on the effects of physical, mechanical, and electrochemical properties of natural cohesive soils on critical shear stress and erosion rate, *International Journal of Sediment Research*, **31**:1-15.
- Kirschbaum D., Stanley T. and Zhou Y. (2015). Spatial and temporal analysis of a global landslide catalog, *Geomorphology*, **249**:4-5.
- Kristo C., Rahardjo H. and Satyanaga A. (2017). Effect of variations in rainfall intensity on slope stability in Singapore. *International Soil and Water Conservation Research*, **5**:258–264.

- Kumar A., Sharma R. K. and Mehta B. S. (2020). Slope stability analysis and mitigation measures for selected landslide sites along NH-205 in Himachal Pradesh, India, *Journal of Earth System Science*, **129**(135).
- Lade P. V. (2010). The mechanics of surficial failure in soil slopes. *Engineering Geology*, **114**:57–64.
- Lambe T. W. and Whitman R. V. (1991). *Soil Mechanics*. John Wiley & Sons, 29.
- Landau L. D. and Lifshitz E.M. (1987). *Fluid Mechanics*, (2<sup>nd</sup> ed.) Butterworth-Heinemann, Oxford.
- Lanni C. (2012). *Hydrological controls on the triggering of shallow landslides: from local to landscape scale*, Doctoral thesis in Environmental Engineering, University of Trento.
- Le Roux O., Jongmans D., Kasperski J., Schwartz S., Potherat P., Lebrout V., Lagabrielle R. and Meric O. (2011). Deep geophysical investigation of the large Séchilienne landslide (western Alps, France) and calibration with geological data. *Engineering Geology*, **120**(1-4):18-31.
- Li L. and Chu X. (2019). Failure mechanism and factor of safety for spatially variable undrained soil slope, *Advances in Civil Engineering*, 8575439(17).
- Li S., Liang W., Zhang W. and Liu Q. (2016). Response of soil moisture to hydro-meteorological variables under different precipitation gradients in the Yellow River basin. *Water Resources Management*, **30**:1867–1884.
- Li X., Shao M., Zhao C. and Jia X. (2019). Spatial variability of soil water content and related factors across the Hexi Corridor of China. *Journal of Arid Land*, **11**:123–134.
- Liu F. and Yang M. (2005) *Verification and Validation of Artificial Neural Network Models*. In: Zhang S., Jarvis R. (eds.) *AI 2005: Advances in Artificial*

- Intelligence. AI 2005. Lecture Notes in Computer Science, vol 3809. *Springer*, Berlin, Heidelberg.
- Liu H., Li L., Li S., and Yang W. (2020). The Time-Dependent Failure Mechanism of Rocks and Associated Application in Slope Engineering: An Explanation Based on Numerical Investigation, *Mathematical Problems in Engineering*, <https://doi.org/10.1155/2020/1680265>.
- Logan D. (2011). *A first course in the finite element method*. Cengage Learning.
- Løvholt F., Pedersen G., Harbitz C. B., Glimsdal S. and Kim J. (2015). On the characteristics of landslide tsunamis, *Philosophical Transactions of the Royal Society of London A: Mathematical, Physical and Engineering Sciences*, **373**(2053), 20140376.
- Lowe J. and Karafiath L. (1960), Stability of earth dams upon drawdown, *In Proc. 1st. Pan American Conference on Soil Mechanics and Foundation Engineering, México*, **2**:537-552.
- Lu M., Zhang J., Zhang L. and Zhang L. (2020). Assessing the annual risk of vehicles being hit by a rainfall-induced landslide: a case study on Kennedy Road in Wan Chai, Hong Kong, *Natural Hazards and Earth System Sciences*, **20**:1833–1846.
- Lupiano V., Rago V., Terranova O. and Iovine G. (2019). Landslide inventory and main geomorphological features affecting slope stability in the Picentino river basin (Campania, southern Italy), *Journal of Maps*, **15**(2):131-141.
- Lu-sheng L., Xia-ting F. and Shi-wei B. (2002). Application of Artificial neural Network to Prediction of Sliding Slope, *J. Rock and Soil Mechanics*, **23**(4):508-510.

- Lu Y. (2015). Deformation and failure mechanism of slope in three dimensions, *Journal of Rock Mechanics and Geotechnical Engineering*, **7**(2):109-119.
- Lynett, P., and Liu P. (2002), A numerical study of submarine landslide generated waves and runup, *Proceedings of the Royal Society of London, Ser. A.*, **458**:2885-2910.
- Ma S., Xu C., Shao X., Zhang P., Liang X. and Tian Y. (2019). Geometric and kinematic features of a landslide in Mabian Sichuan, China, derived from UAV photography. *Landslides* **16**:373–381.
- Maier H. and Dandy G. (1997). Determining inputs for neural networks models of multivariate time series, *Computer Aided Civil and Infrastructure Engineering*, **12**(5):353-368.
- Masri S., Smyth A., Chassiakos A., Caughey T. and Hunter N. (2000). Application of neural networks for detection of changes in nonlinear systems, *Journal of Engineering Mechanics*, **126**(7):666-76.
- Masters T. (1993). *Practical Neural Network Recipes in C++*. Academic Press: San Diego.
- McColl S. T. (2015). Landslide Causes and Triggers, *Landslide Hazards, Risks, and Disasters*, 17-42.
- McCulloch W. and Pitts W. (1943). Logical calculus of the ideas immanent in nervous activity. *Bulletin of Mathematical Biophysics*, **5**:115-133.
- McIntosh K. and Krupnik A. (2002). Integration of Laser-derived DSMs and matched image edges for generating an accurate surface model, *Journal of Photogrammetry and Remote Sensing*, **56**:167-176.
- McKenna G. (2006). Rules of thumb for geotechnical instrumentation costs. *Geotechnical News*, **24**(2):46-47.

- Miles S. and Keefer D. (2001). Seismic landslide hazard for the city of Berkeley, California. U.S. Geological Survey Miscellaneous Field Studies Map MF-2378. <http://geopubs.wr.usgs.gov/map-mf/mf2378/>, accessed 16/01/2020.
- Ministry of State for Special Programmes, Office of the President (2009). *National Policy for Disaster Management in Kenya*. <http://www.sprogrammes.co.ke> accessed 15/12/2019.
- Mitchell J. K. and Soga K. (2005). *Fundamentals of soil behavior*, Third edition, John Wiley and Sons, Inc.
- Mollahasani A., Alavi A., Gandomi A. and Rashed A. (2011). Nonlinear Neural-Based Modeling of Soil Cohesion Intercept, *KSCE Journal of Civil Engineering*, **15**(5):831-840.
- Moore I. D. and Burch G. J. (1986). Modelling Erosion and Deposition. Topographic Effects. *Transactions of American Society of Agriculture Engineering*, **29**:1624-1630.
- Morgan G., Rawlings G. and Sobkowicz J. (1992). Evaluating total risk to communities from large debris flows. *Geotechnique and natural hazards: Canadian Geotechnical Society* (Bitech Publishers), 225-236.
- Morgenstern N. and Price V. (1965). The Analysis of the Stability of General Slip Surfaces. *Geotechnique*, **15**(1):77-93.
- Mostyn G. and Li K. (1993). Probabilistic slope stability – State of play. In *Probabilistic Method in Geotechnical Engineering: Proceedings of the conference*, Edited by Li, K.S. and Lo, S-C.R., Pub. A.A. Balkema, 89-110.
- Mukhlisin M. and Khiyon K. (2018). The Effects of Cracking on Slope Stability, *Journal of the Geological Society of India*, **91**:704-710.

- Muntohar A. and Liao H. (2009). Analysis of rainfall-induced infinite slope failure during typhoon using a hydrologicalgeotechnical model, *Environmental Geology*, **56**:1145-1159.
- Mussett A. and Khan M. (2000). *Looking into the earth: an introduction to geological geophysics*. Cambridge: Cambridge University Press.
- Mustafa M., Isa M. H., Rezaur R. B. and Rahardjo H. (2015). Data-driven modelling for pore water pressure variation responses to rainfall, in *WIT Transactions on The Built Environment*, WIT Press, **1**:447–455.
- Nahm F. (2016) Nonparametric statistical tests for the continuous data: The basic concept and the practical use. *Korean Journal of Anesthesiology*, **69**:8-14.
- Najjar Y., Ali H. and Basheer I. (1999). On the use of neurons for simulating the stress-strain behavior of soils. *Proc., 7th International Symposium on Numerical Models in Geomechanics*, G. N. Pande (ed.), Graz, Austria, NUMOG VII, 657-662.
- National Research Council (2004). *Partnerships for reducing landslide risk: Assessment of the national landslide hazards mitigation strategy*, the National Academies Press, Washington, DC.
- Ng C., Wang B. and Tung Y. (2001). Three-dimensional numerical investigations of groundwater responses in an unsaturated slope subjected to various rainfall patterns. *Canadian Geotechnical Journal*, **38**:1049-1062.
- Ngecu C., Nyamai M. and Erima G. (2004). The extent and significance of mass-movements in Eastern Africa: case studies of some major landslides in Uganda and Kenya. *Environmental geology*, 3-8.



- Ni S., Lu P. and Juang C. (1996). A Fuzzy Neural Network Approach to Evaluation of Slope Failure Potential, *Computer-Aided Civil and Infrastructure Engineering*, **11**(1):59-66.
- Ojha R., Morbidelli R., Saltalippi C., Flammini A. and Govindaraju R. S. (2014). Scaling of surface soil moisture over heterogeneous fields subjected to a single rainfall event. *Journal of Hydrology*, **516**:21–36.
- Olivares L. and Damiano E. (2007). Post-failure Mechanics of Landslides: Laboratory Investigation of Flow slides in Pyroclastic Soils, *Journal of Geotechnical and Geomechanical Engineering*, 51-62.
- Orense R. P., Shimoma S., Maeda K. and Towhata I. (2004). Instrumented Model Slope Failure due to Water Seepage. *Journal of Natural Disaster Science*, **26**(1):15-16.
- Pantelidis L. (2009). Rock slope stability assessment through rock mass classification systems. *International Journal of Rock Mechanics and Mining Sciences*, **46**(2):315–325.
- Papadopoulos G., Edwards P. J. and Murray A. F. (2000). Confidence Estimation Methods for Neural Networks: A Practical Comparison. In: *European Symposium on Artificial Neural Networks*, Bruges, Belgium, 75–80.
- Pardo J., Lozano A., Herrera G., Mulas J. and Rodríguez Á. (2013). Instrumental monitoring of the subsidence due to groundwater withdrawal in the city of Murcia (Spain). *Environmental Earth Sciences*, **70**(5):1957-1963.
- Parsons R. L. and Milburn J. P. (2018). Engineering behavior of stabilized soils, *Transportation Research Record: Journal of the Transportation Research Board*, **1837**:20–29.

- Patil V. and Gopale R. (2018). A geographical study of landslide: A case study of Malin village of Ambegaon Tahsil in Pune District, Maharashtra. *Peer Reviewed International Research Journal of Geography*, **35**:55–60.
- Perrone A., Lapenna V. and Piscitelli S. (2014). Electrical resistivity tomography technique for landslide investigation: A review. *Earth-Science Reviews*, **135**:65–82.
- Petley D. (2009). Mass Movement Hazards. In: K. Smith and D. Petley (Eds), *Environmental Hazards: Assessing risk and reducing disaster*. Routledge, London, 416.
- Petley D. (2012). Global patterns of loss of life from landslides, *Geology*, **40**:927–930.
- Pettinelli E., Cereti A., Galli A. and Bella F. (2002). Time domain reflectometry: Calibration techniques for accurate measurement of the dielectric properties of various materials. *Review of Scientific Instruments*, **73**:3553–3562.
- Piciullo L., Calvello M. and Cepeda J. M. (2018). Territorial early warning systems for rainfall-induced landslides. *Earth-Science Reviews*, **179**:228–247.
- Powrie W. (2004). *Soil Mechanics: Concepts and Applications* (2<sup>nd</sup> ed.), Spon Press, London.
- Pradhan A. M. S. (2019). *Rainfall-induced shallow landslide prediction and development of warning model in Korean Mountain*, Doctoral dissertation, Department of Ocean Engineering, Pukyong National University, Busan, 48513, South Korea.
- Price D. G. (2009). *Engineering Geology Principles and Practice*, Springer-Verlag, Berlin Heidelberg, p. 450.

- Qi S. C. and Vanapalli S. K. (2015). Hydro-mechanical coupling effect on surficial layer stability of unsaturated expansive soil slopes. *Computers and Geotechnics*, **70**:68–82.
- Qin L., Shuang F., and Zhu H. (2018). Research on the technological architectural design of geological hazard monitoring and rescue-after-disaster system based on cloud computing and Internet of things. *International Journal of System Assurance Engineering and Management*, **9**:684–695.
- Rafiq M., Bugmann G. and Easterbrook D. (2001). Neural network design for engineering applications. *Computers and Structures*, **79**(17):1541-1552.
- Raghuvanshi T. K. (2019). Plane failure in rock slopes – A review on stability analysis techniques, *Journal of King Saud University - Science*, **31**(1):101-109.
- Rahardjo H., Ong T., Rezaur R., and Leong, E. (2007). Factors controlling instability of homogeneous soil slopes under rainfall, *Journal of Geotechnical and Geoenvironmental Engineering*, **133**(12):1532–1543.
- Ray R., Jacobs J. and de Alba P. (2010). Impacts of Unsaturated Zone Soil Moisture and Groundwater Table on Slope Instability. *Journal of Geotechnical and Geoenvironmental Engineering*, **136**(10):1448–1458.
- Renalier F., Jongmans D., Campillo M. and Bard P. (2010). Shear wave velocity imaging of the Avignonet landslide (France) using ambient noise cross correlation. *Journal of Geophysical Research*, **115**, F03032.
- Republic of Kenya (2014). Soil suitability evaluation for maize production in Kenya. *A Report by National Accelerated Agricultural Inputs Access Programme (NAAIAP) in collaboration with Kenya Agricultural Research Institute (KARI), Department of Kenya Soil Survey.*

- Riquelme A., Tomás R. and Abellán A. (2016). Characterization of rock slopes through slope mass rating using 3D point clouds, *International Journal of Rock Mechanics and Mining Sciences*, **84**:165–176.
- Rueger J., Alanko, G. and Snow T. (1994). Monitoring of an open cut mine with a surveying robot, *The Australian Surveyor*, 252–266.
- Rumelhart D., Hinton G. and Williams R. (1986). Learning representations by back-propagating errors. *Nature*, **323**:533–536.
- Russell A., Johnson C., Edwards A., Viroulet S., Rocha F. and Gray J. (2019). Retrogressive failure of a static granular layer on an inclined plane, *Journal of Fluid Mechanics*, **869**:313-340.
- Rybar J., Stemberk J. and Wagner P. (2002). Landslides: *proceedings of the First European Conference on Landslides*, Czech Republic, Prague.
- Sakellariou M. and Ferentinou M. (2005). A study of slope stability prediction using neural networks, *Geotechnical and Geological Engineering*, **23**:419.
- Salunkhe D. P., Chvan G., Bartakke R. N. and Kothavale P. R. (2017). An overview on methods for slope stability analysis, *International Journal of Engineering Research & Technology*, **6**(3):528-535.
- Santi P., Hewitt K., Van Dine D. and Barillas C. (2011). Debris-flow impact, vulnerability, and response. *Natural Hazards*, **56**:371–402.
- Santos T., Lana M., Pereira T. and Canbulat I. (2019). Quantitative hazard assessment system (Has-Q) for open pit mine slopes, *International Journal of Mining Science and Technology*, **29**(3):419–427.
- Santos M. A. N., Panachuki E., Alves Sobrinho T., Oliveira P. T. S. and Rodrigues D. B. B. (2014) Water infiltration in na Ultisol after cultivation of common bean, *Revista Brasileira de Ciência do Solo*, **38**:1612-1620.

- Sastry R. and Mondal S. (2013). Geophysical Characterization of the Salna Sinking Zone, Garhwal Himalaya, India, *Surveys in Geophysics*, **34**:89–119.
- Savage S. B. and Hutter K. (1991). The dynamics of avalanches of granular materials from initiation to runout. Part I: Analysis, *Acta Mechanica*, **86**:201–223.
- Schrott L. and Sass O. (2008). Application of field geophysics in geomorphology: Advances and limitations exemplified by case studies. *Geomorphology*, **93**(1-2):55–73.
- Seemann R., Brinkmann M., Di Michiel M., Sheppard A. and Herminghaus S. (2008). Liquid distribution and cohesion in wet granular assemblies beyond the capillary bridge regime, *Journal of Physics: Condensed Matter*, **20**(49):494236.
- Sellers B. (2005). The truth about accuracy. *Geotechnical News*, **23**(2):30–32.
- Seneviratne S. I., Corti T., Davin E. L., Hirschi M., Jaeger E. B., Lehner I., Orlowsky B., and Teuling A. J. (2010). Investigating soil moisture– climate interactions in a changing climate: A review, *Earth-Science Reviews*, **99**:125-161.
- Sepúlveda S. and Petley D. (2015). Regional trends and controlling factors of fatal landslides in Latin America and the Caribbean, *Natural Hazards and Earth System Sciences*, **15**:1821–1833.
- Serdarevic A. and Babic F. (2019). Landslide Causes and Corrective Measures – Case Study of the Sarajevo Canton, *Journal of Civil Engineering Research*, **9**(2):51-57.
- Setan H. and Singh R. (2001). Deformation analysis of a geodetic monitoring network. *Geomatica*, **55**(3).
- Shahin M., Jaksa M. and Maier H. (2001). Artificial neural network applications in geotechnical engineering. *Australian Geomechanics*, **36**(1):49-62.

- Shahin M., Maier H. and Jaksa M. (2004). Data division for developing neural networks applied to geotechnical engineering. *Journal of Computing in Civil Engineering, ASCE*; **18**(2):105–14.
- Shahin M., Maier H. and Jaksa M. (2002). Predicting settlements of shallow foundation using artificial neural networks. *Journal Geotechnical and Geoenvironmental Engineering ASCE*, **128**(9):785–93.
- Sidle R. and Bogaard T. (2016). Dynamic earth system and ecological controls of rainfall-initiated landslides. *Earth - Science Reviews*, **159**:275–291.
- Sidle R., and Ochiai H. (2006). Landslides: Processes, prediction, and land use, *Water resources monograph*, 18, American Geophysical Union, Washington, D.C.
- Singh T., Singh R., Singh B., Sharma L., Singh R. and Ansari M. (2016). Investigations and stability analyses of Malin village landslide of Pune district, Maharashtra, India. *Journal of the International Society for the Prevention and Mitigation of Natural Hazards*, **81**(3):2019–2030.
- Sinha S., Singh V. and Jakhanwal M. (2015). Rainfall Runoff Modeling of Punpun River Basin Using ANN – A Case Study. *International Journal of Research in Engineering and Social Sciences*, **5**(5):32-49.
- Spencer E. (1967). A Method of analysis of the Stability of Embankments Assuming Parallel Inter-Slice Forces. *Géotechnique*, **17**:11–26.
- Springman S., Thielen A., Kienzler P. and Friedel S. (2013). A long-term field study for the investigation of rainfall-induced landslides. *Géotechnique*, **63**(14):1177– 1193.
- Stein R., (1993). Selecting data for neural networks. *AI Expert*, **2**:42–47.
- Stone M. (1974). Cross-validatory choice and assessment of statistical predictions. *Journal of Royal Statistical Society*, **B36**:111–147.

- Sturzenegger M. and Stead D. (2009). Close-range terrestrial digital photogrammetry and terrestrial laser scanning for discontinuity characterization on rock cuts. *Engineering Geology*, **106**(3-4):163–182.
- Suh J., Choi Y., Roh T., Lee H. and Park H. (2011). National-scale assessment of landslide susceptibility to rank the vulnerability to failure of rock-cut slopes along expressways in Korea, *Environmental Earth Sciences*, **63**(3):619–632.
- Tai Y.-C., Ko C.-J., Li K.-D., Wu Y.-C., Kuo C.-Y., Chen R.-F. and Lin C.-W. (2020). An Idealized Landslide Failure Surface and Its Impacts on the Traveling Paths. *Frontiers in Earth Science*, **8**:313.
- Takahashi T., Takeuchi T. and Sassa K. (2006). ISRM suggested methods for borehole geophysics in rock engineering. *International Journal of Rock Mechanics and Mining Sciences*, **43**(3):337–368.
- Tappin D., Watts P. and Grilli S. (2008). The Papua New Guinea tsunami of 17 July 1998: Anatomy of a catastrophic event, *Natural Hazards and Earth System Sciences*, **8**(2):243–266.
- Terzaghi K. (1960). Mechanism of landslides, *Geological Society of America, Engineering Geology Volume*, 84-123.
- Thennavan E. and Pattukandan G. (2020). Evaluation of landslide hazard and its impacts on hilly environment of the Nilgiris District - a geospatial approach. *Geoenvironmental Disasters*, **7**(3).
- Thielen A., Friedel S., Plötze M. and Springman S. (2005). Combined approach for site investigation in terms of the analysis of rainfall induced landslides. *Proceedings of the 16th international conference on soil mechanics and geotechnical engineering*, Millpress, Rotterdam, the Netherlands, 2591–2594.

- Tonon F., and Kottenstette J. (eds) (2007). *Laser and Photogrammetric Methods for Rock Face Characterization. Report on a workshop held June 17–18, 2006 in Golden, CO, in Conjunction with Golden Rocks, 41st U.S. Rock Mechanics Symposium*, Colorado School of Mines.
- Trani D., Hellmuth J. and Thompson J. (2020). Modelled versus observed open cut performance in weak transition rock: the Dubbo Quarry case study, in Dight P. M. (ed.), *Proceedings of the 2020 International Symposium on Slope Stability in Open Pit Mining and Civil Engineering*, Australian Centre for Geomechanics, Perth, 863-872.
- Tsangaratos P. (2012). *Research on the engineering geological behaviour of the geological formations by the use of information systems*, PhD Thesis, School of Mining Engineering Ge-ology, Department of Geological Section, NTUA, Athens, 363.
- Turcotte D. and Schubert G. (2002). *Geodynamics*, Cambridge University Press, New York.
- UNDRR-ISC (United Nations Office for Disaster Risk Reduction- international Science Council) (2020). *UNDRR-ISC Technical Report on Sendai Hazards Definitions and Classifications*, Geneva, Switzerland ([www.undrr.org](http://www.undrr.org)).
- Van Genuchten M. (1980). A closed-form equation for predicting the hydraulic conductivity of unsaturated soils. *Soil Science Society of America Journal*, **44**(5):892–898.
- Vanapalli S. and Fredlund D. (2000). *Comparison of empirical procedures to predict the shear strength of unsaturated soils using the soil-water characteristic curve*, In C.D. Shackelford, S.L. Houston and N.Y. Chang (Eds.). *Advances in*



- Unsaturated Geotechnics. *Geotechnical Special Publication No. 99*, ASCE, Reston, VA, 195–209.
- Varnes D. (1984). *Landslide hazard zonation: a review of principles and practice*. UNESCO, Paris, 1-55.
- Varnes D. (1978). Slope movement: types and processes. *Landslides, Analysis and control*, Transportation Research Board Report, **176**:11–33.
- Vondráčková T., Kmec J., Čejka J., Bartuška L. and Stopka O. (2016). Evaluation of the Parameters Affecting the Cohesion of Fine-Grained Soil, *IOP Conference Series Earth and Environmental Science*, **44**:022019.
- Voyat I., Roncella R., Forlani G. and Ferrero A. (2006). Advanced techniques for geo structural surveys in modelling fractured rock masses – Application to two Alpine sites, *Proceeding: The 41st U.S. Symposium on Rock Mechanics (USRMS): “50 Years of Rock Mechanics - Landmarks and Future Challenges”*, Colorado.
- Wagner J. -F. (2013). Mechanical Properties of Clays and Clay Minerals, *Developments in Clay Science*, **5**:347-381.
- Wanatowski D. and Chu J. (2012). Factors affecting pre-failure instability of sand under plane-strain conditions. *Geotechnique*, **62**(2):121-135.
- Wang B., Vardon P. J. and Hicks M. A. (2016). Investigation of retrogressive and progressive slope failure mechanisms using the material point method. *Computers and Geotechnics*, **78**:88-98.
- Wang R. H., Zhou H. Q. and Liu Q. Y. (2018). Failure modes of key blocks in high slope with steep downward soil, *Journal of Water Resources and Architectural Engineering*, **16**(03):165–169.

- Warneke J., Dwyer J. and Orr T. (2007). Use of a 3-D scanning laser to quantify drift geometry and overbreak due to blast damage in underground manned entries. In *Rock Mechanics: Meeting Society's Challenges and Demands*, Vol. 1. Edited by E. Eberhardt, D. Stead, and T. Morrison. London: Taylor and Francis, 93–100.
- Watts P., Grilli S., Kirby J., Fryer G. and Tappin D. (2003). Landslide tsunami case studies using a Boussinesq model and a fully nonlinear tsunami generation model, *Natural Hazards Earth Systems Sciences*, **3**:391-402.
- Weiss R., Fritz H. and Wünnemann K. (2009). Hybrid modelling of the mega tsunami runup in Lituya Bay after half a century, *Geophysical Research Letters*, **36**: L09602.
- Welsch W., Heunecke O. and Kuhlmann H. (2000). Auswertung geodätischer Überwachungsmessungen. In Möser et al. (eds.): *Handbuch Ingenieurgeodäsie*. Wichmann Verlag, Heidelberg.
- Whiteley J., Chambers J., Uhlemann S., Wilkinson, P. and Kendall, J. (2019). Geophysical monitoring of moisture-induced landslides: A review. *Reviews of Geophysics*, **57**:106–145.
- Wicki A., Lehmann P., Hauck C., Seneviratne S., Waldner P. and Stähli M. (2020). Assessing the potential of soil moisture measurements for regional landslide early warning. *Landslides*, Springer Nature Switzerland AG.
- Wines, D. R. (2020). Understanding the sensitivity of numerical slope stability analyses to geotechnical and other input parameters, in Dight P. M. (ed.), *Proceedings of the 2020 International Symposium on Slope Stability in Open Pit Mining and Civil Engineering*, Australian Centre for Geomechanics, Perth, 983-1002.

- Wolff T. (1996). Probabilistic slope stability in theory and practice. *In Uncertainty in the geologic environment: From theory to practice*, Edited by Shackelford, C.D. et al., ASCE, GSP, **58**:419-433.
- World Conference on Disaster Reduction (WCDR) (2005). *Conference Report*. Kobe, Hyogo, Japan.
- Wu X., Chen X., Benjamin Zhan F. and Hong S. (2015). Global research trends in landslides during 1991–2014: a bibliometric analysis, *Landslides*, **12**:1215–1226.
- Wunderlich T. (2004). Considerations Concerning Geodetical Long-Term Monitoring Tasks. In: Malzahn, D., Plapp, T. (Eds.): *Proceedings of Disasters and Society – From Hazard Assessment to Risk Reduction*, Karlsruhe.
- Yang P. (2019). Analysis of the Influence of Initial Gravity Field on the Stability Analysis of Soil Slope, *IOP Conference Series: Earth and Environmental Science*, **218**(1), 012026, 10.1088/1755-1315/218/1/012026.
- Yang R., Xiao P. and Qi S. (2019). Analysis of Slope Stability in Unsaturated Expansive Soil: A Case Study. *Frontiers in Earth Sciences*, **7**:292.
- Yang Y., and Rosenbaum, M. (2002). The artificial neural network as a tool for assessing geotechnical properties, *Geotechnical Engineering Journal*, **20**(2):149-168.
- Zaman, M. (2000). Dynamics of rigid pavements including vehicle- pavement interaction effects. *Modelling in Geomechanics*, M. Zaman, G. Gioda and J. Booker (eds.), Wiley, New York, 467-491.
- Zhang C., Shao W., Yue F., Saffari P. and Nie W. (2019). Physical Tank Experiment Investigation on Rainfall Producing Groundwater Level in Homogeneous

Material Slopes, *Geofluids / Published Special Issues / Special Issue*,  
<https://doi.org/10.1155/2019/5368765>.

- Zhang J., Li J. and Lin H. (2018). Models and influencing factors of the delay phenomenon for rainfall on slope stability. *European Journal of Environmental and Civil Engineering*, **22**:122–136.
- Zhang J., Sun D., Zhou A. and Jiang T. (2015). Hydro-mechanical behaviour of expansive soils with different suctions and suction histories. *Canadian Geotechnical Journal*, **53**(1):1-13.
- Zhang Y., Hanaor D. and Gan Y. (2015). Rate effects in inter-granular capillary bridges, *Unsaturated Soil Mechanics-from Theory to Practice: Proceedings of the 6th Asia Pacific Conference on Unsaturated Soils*, CRC Press, 463–466.
- Zhao B., Dai Q., Han D., Dai H., Mao J. and Zhuo L. (2019). Probabilistic thresholds for landslides warning by integrating soil moisture conditions with rainfall thresholds. *Journal of Hydrology*, **574**:276–287.
- Zhao H. and Zhang L. (2014) Instability of saturated and unsaturated coarse granular soils. *Journal of Geotechnical and Geoenvironmental Engineering*, **140**(1):25–35.
- Zheng H. and Tham L. G. (2009). Improved Bell's method for the stability analysis of slopes, *International Journal for Numerical and Analytical Methods in Geomechanics*, **33**(14):1673–1689.
- Zheng S., Zhang G., Yuan X., Ye F. and Fu W. (2020). Failure characteristics of shallow soil slope considering surface runoff and interstitial flow, *Geomatics, Natural Hazards and Risk*, **11**(1):845-868.
- Zhu F., Zhang W. and Su M. (2017). A new calculation method for the soil slope safety factor, *Mathematical problems in engineering*, vol. 2017, 3569826.

- Zhu H., Griffiths D. V., Fenton G. A., and Zhang L. M. (2015). Undrained failure mechanisms of slopes in random soil, *Engineering Geology*, **191**:31–35.
- Zhu H. D., Shi Z. H., Fang N. F., Wu G. L., Guo Z. L., Zhang Y. (2014). Soil moisture response to environmental factors following precipitation events in a small catchment. *Catena*, **120**:73–80.
- Zhu W. (2019). The effect of dry-wet cycle on crack propagation and shear strength index of Yunnan laterite in China, *Applied Ecology and Environmental Research*, **17**(4):7881-7889.
- Zou F., Zhan Q. and Zhang W. (2018). Quantifying the impact of human activities on geological hazards in mountainous areas: evidence from Shennongjia, China, *Natural Hazards*, **90**:137–155.

## APPENDICES

**Appendix I: Table showing a section of the normalized data in the range -1 to +1 to be fed in the ANN for analysis (Pre-processing of data)**

Input					Target
slope angle	Water content	Cohesion	Pore pressure	int friction angle	FS 30
[n]	[n]	[n]	[n]	[n]	[n]
min: 30	min: 0.001315	min: 3066	min: -26730	min: 9.463	min: 0.374
max: 60	max: 0.497	max: 22180	max: -0.691	max: 59.107	max: 3.815
-0.4	-0.398447401	-0.10601653	-0.4	0.4	0.388375472
-0.4	0.396772144	-0.16628649	0.12855837	-0.374184191	-0.24934612
0.13333333	-0.366615895	-0.04742074	-0.21982325	0.390427846	-0.02429526
-0.13333333	0.212784329	-0.35333264	0.312625979	-0.397341068	-0.37070619
-0.4	0.316075734	-0.39673538	0.382437885	-0.39476271	-0.35977913
-0.4	0.240221108	0.11497332	-0.06628393	-0.307469181	-0.08962511
0.4	-0.232659855	0.37153919	-0.11177706	0.100604303	-0.18541122
-0.13333333	0.246676821	-0.02816784	0.024702337	-0.350930626	-0.25632084
-0.4	0.38224679	-0.24606048	0.18889663	-0.379937153	-0.2867771
0.13333333	0.169208267	-0.31076698	0.133915785	-0.384497623	-0.37396106
0.13333333	-0.198767362	0.35354191	-0.18929496	0.131560712	-0.07707062
-0.13333333	0.245062893	-0.39882808	0.279823036	-0.392796713	-0.38302819
0.13333333	0.125632206	-0.38920163	0.214636166	-0.395600677	-0.39302528
-0.13333333	-0.229431998	0.23509469	-0.29135522	0.251905568	0.106364429
-0.13333333	0.204714688	-0.32164905	0.31062069	-0.398179035	-0.36140657
-0.4	0.333828944	-0.39677723	0.350427181	-0.392281041	-0.35861668
-0.13333333	-0.398871864	-0.10601653	-0.31320389	0.4	0.133100843
0.4	-0.019621332	-0.21144711	0.119699181	-0.399887197	-0.37349608
-0.4	0.341898585	-0.38878309	0.333397186	-0.391056321	-0.35466434
-0.13333333	0.035252227	0.31796589	-0.16026316	-0.183401821	-0.08776518
-0.13333333	0.291866811	-0.24606048	0.147503866	-0.379937153	-0.33281023
-0.13333333	0.264430031	-0.36789788	0.237292943	-0.388929176	-0.37233362
0.13333333	-0.061583465	0.35312337	-0.12823839	-0.142776569	-0.16704446
0.13333333	0.164366483	-0.07504447	0.035177729	-0.360986222	-0.31793083
0.13333333	-0.127754522	0.4	-0.16205894	-0.018177423	-0.11984888
0.4	-0.156805229	0.38032855	-0.08663612	-0.09678511	-0.22911944
0.4	-0.04867204	0.16268704	-0.03336127	-0.287051809	-0.29793665
-0.13333333	0.153068985	0.13883018	-0.06478744	-0.297687535	-0.18564371
-0.4	0.4	-0.14422936	0.112875211	-0.372379341	-0.23865155
0.4	-0.277849844	0.27067071	-0.12255175	0.223027959	-0.16495205
0.13333333	-0.350476613	-0.01142618	-0.21892536	0.379904923	-0.02406277
-0.4	0.30155038	0.01954588	-0.0007379	-0.339021835	-0.14867771
-0.4	0.370949292	-0.29590876	0.230858059	-0.383369591	-0.31025865

## Appendix II: A section of the Input, Target, Forecast, Relative Error and Performance

Estimate data table during training of the ANN

Input					Target	Output			
slope angle	wc	C	Pu	int ang	FS	Forecast	Abs. Error	Rel. Error	Estimate
30	0	10090	-26730	59.107	3.765	3.850365945	0.085365945	2.27%	Good
30	99	8650	-9070	11.065	1.022	1.03631573	0.01431573	1.40%	Good
50	4	11490	-20710	58.513	1.99	1.917670324	-0.07232968	3.63%	Good
40	76	4181	-2920	9.628	0.5	0.492296128	-0.00770387	1.54%	Good
30	89	3144	-587.47	9.788	0.547	0.571297218	0.024297218	4.44%	Good
30	80	15370	-15580	15.205	1.709	1.770131473	0.061131473	3.58%	Good
60	21	21500	-17100	40.528	1.297	1.337146823	0.040146823	3.10%	Good
40	80	11950	-12540	12.508	0.992	1.06181084	0.06981084	7.04%	Good
30	97	6744	-7054	10.708	0.861	0.890811254	0.029811254	3.46%	Good
50	71	5198	-8891	10.425	0.486	0.463576257	-0.02242374	4.61%	Good
50	25	21070	-19690	42.449	1.763	1.691352009	-0.07164799	4.06%	Good
40	80	3094	-4016	9.91	0.447	0.472963346	0.025963346	5.81%	Good
50	65	3324	-6194	9.736	0.404	0.417721236	0.013721236	3.40%	Good
40	21	18240	-23100	49.917	2.552	2.552395464	0.000395464	0.02%	Good
40	75	4938	-2987	9.576	0.54	0.521856348	-0.01814365	3.36%	Good
30	91	3143	-1657	9.942	0.552	0.592208453	0.040208453	7.28%	Good
40	0	10090	-23830	59.107	2.667	2.993867808	0.326867808	12.26%	Bad
60	47	7571	-9366	9.47	0.488	0.557357104	0.069357104	14.21%	Bad
30	92	3334	-2226	10.018	0.569	0.609301639	0.040301639	7.08%	Good
40	54	20220	-18720	22.904	1.717	1.701672141	-0.01532786	0.89%	Good
40	86	6744	-8437	10.708	0.663	0.654394978	-0.00860502	1.30%	Good
40	83	3833	-5437	10.15	0.493	0.504290458	0.011290458	2.29%	Good
50	42	21060	-17650	25.425	1.376	1.346064695	-0.0299353	2.18%	Good
50	70	10830	-12190	11.884	0.727	0.752759234	0.025759234	3.54%	Good
50	34	22180	-18780	33.157	1.579	1.611198	0.032198	2.04%	Good
60	30	21710	-16260	28.279	1.109	1.082346566	-0.02665343	2.40%	Good
60	44	16510	-14480	16.472	0.813	0.768631759	-0.04436824	5.46%	Good
40	69	15940	-15530	15.812	1.296	1.414544533	0.118544533	9.15%	Good
30	99	9177	-9594	11.177	1.068	1.090508378	0.022508378	2.11%	Good
60	15	19090	-17460	48.125	1.385	1.43221226	0.04721226	3.41%	Good
50	6	12350	-20680	57.86	1.991	1.898148321	-0.09285168	4.66%	Good
30	87	13090	-13390	13.247	1.455	1.336973454	-0.11802655	8.11%	Good
30	96	5553	-5652	10.495	0.76	0.788816658	0.028816658	3.79%	Good
40	77	3599	-3012	9.689	0.47	0.474445893	0.004445893	0.95%	Good
60	51	3450	-9005	9.712	0.382	0.373524609	-0.00847539	2.22%	Good
50	45	20220	-17140	22.904	1.295	1.374563738	0.079563738	6.14%	Good
50	67	3066	-6548	9.846	0.396	0.39947255	0.00347255	0.88%	Good
60	11	16340	-17650	53.188	1.439	1.461054296	0.022054296	1.53%	Good
60	49	4668	-8950	9.593	0.413	0.436924708	0.023924708	5.79%	Good
30	87	3221	-437.195	9.761	0.552	0.602246298	0.050246298	9.10%	Good
40	81	3143	-4215	9.942	0.451	0.467625091	0.016625091	3.69%	Good
60	28	22100	-16530	31.454	1.165	1.148158259	-0.01684174	1.45%	Good
40	78	3324	-3161	9.736	0.456	0.463410316	0.007410316	1.63%	Good
40	78	3221	-3262	9.761	0.451	0.467520896	0.016520896	3.66%	Good
30	90	3067	-1167	9.877	0.544	0.582352958	0.038352958	7.05%	Good
40	73	6518	-3447	9.509	0.625	0.606169524	-0.01883048	3.01%	Good
60	51	3221	-9084	9.761	0.377	0.372955758	-0.00404424	1.07%	Good
40	78	3450	-3078	9.712	0.462	0.460487319	-0.00151268	0.33%	Good
30	41	22050	-23890	36.749	3.13	3.130103569	0.000103569	0.00%	Good
40	58	19250	-17960	20.707	1.605	1.533726763	-0.07127324	4.44%	Good
50	62	14230	-14000	14.14	0.9	0.793185438	-0.10681456	11.87%	Bad
50	49	19250	-16610	20.707	1.215	1.348938355	0.133938355	11.02%	Good

**Appendix III: Budget Estimates**

		<b>Year1</b>	<b>Year 2</b>
	<b>Equipment</b>	<b>COST (KSHS)</b>	<b>COST (KSHS)</b>
1	Type K thermocouples	3,000	
2	TC-08 thermocouple data logger	1,500	
3	PCI-3140R Time-domain reflectometer (TDR)	12,000	
4	5" GPS NAV+Bluetooth+FM Transmitter+GPRS+4G Card 09 map	82,000	
5	Geophone	68,000	
6	Druck PDCR-81 miniature pore pressure transducers	8,000	
7	Digital camera	15,000	
8	Micro-computer	15,000	
9	Branded computers (server)	50,000	
10	Analogue-to-digital (ADC) converter	6,000	
11	Data logger	3,000	
12	10x10 cm solar cell module	2,000	
13	Soldering gun	2,000	
14	Rain gauge	1,000	
15	Laptop	50,000	
16	ESRI ArcView v. 3.1, ArcScene v. 8.1, ArcGIS		24,000
17	Ilwis 3.0		22,000
18	Matlab v.8.0		18,000
19	GeoModelling software		20,000
<b>Sub-total</b>		<b>318,500</b>	<b>84,000</b>

	<b>Expendable supplies</b>	<b>COST (KSHS)</b>	<b>COST (KSHS)</b>
1	Soldering wires	200	200
2	PCB boards	1,000	1,000
3	Connecting wires	500	500
<b>Sub-total</b>		<b>1,700</b>	<b>1,700</b>

	<b>Literature, documentation, information</b>	<b>COST (KSHS)</b>	<b>COST (KSHS)</b>
1	Printing	6,000	10,000
2	Publication	2,000	4,000



3	Internet services	10,000	15,000
4	Photocopying	4,000	4,000
5	Progress reports and thesis and drafts binding		8,000
<b>Sub-total</b>		<b>22,000</b>	<b>35,000</b>

<b>10</b>	<b>Local travel</b>	<b>COST (KSHS)</b>	<b>COST (KSHS)</b>
1	Subsistence	50,000	100,000
2	Transport (student and supervisors)		120,000
3	Support staff (wages) in the field		50,000
<b>Sub-total</b>		<b>50,000</b>	<b>270,000</b>

<b>11</b>	<b>Other costs</b>	<b>COST (KSHS)</b>	<b>COST (KSHS)</b>
1	Ruled paper (1 ream)	300	300
2	Pens (1pack of 20 pens)	200	200
3	Flash disk (4GB)	2,500	
4	Compact disks (1 pack of 10 CDs)	150	150
<b>Sub-total</b>		<b>3,150</b>	<b>650</b>

<b>GRAND TOTALS (Kshs.)</b>	<b>396,350</b>	<b>397,350</b>
-----------------------------	----------------	----------------

<b>OVERAL TOTAL FOR TWO YEARS (Kshs.)</b>	<b>793,700</b>
---	----------------



**Appendix V: Similarity Report**